Università degli Studi di Napoli "Federico II"

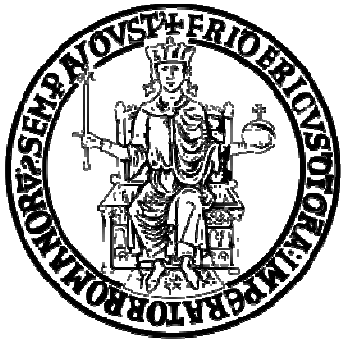

Dottorato di Ricerca in

Ingegneria Aerospaziale, Navale e della Qualità

XXVI Ciclo

Aerothermodynamic and mission analyses of deployable aerobraking Earth re-entry systems

Coordinatore:

Ch.mo Prof. L. De Luca

Tutor:

Ch.mo Prof. R. Savino

Candidato:

Ing. Valerio Carandente

Acknowledgements

At the end of a three years formative experience like a Ph.D., I think it is worth acknowledging all the people contributing to my scientific and personal growth.
First of all, I would like to thank my tutor, Prof. Raffaele Savino, for his constant guidance throughout the Ph.D. course and for having transmitted me his passion and dedication for Research.
Then I thank Prof. Rodolfo Monti, Prof. Gennaro Zuppardi, Dr. Gennaro Russo, Dr. Raimondo Fortezza and Dr. Antonio Esposito for the fruitful collaboration.
Finally I am grateful to all the members of the Hyper Landers team for the great work done together and to all the students (and friends) I had the honour to supervise during their training at University. Many thanks to: Abdoulaye, Alessandro, Davide, Domenico, Gianpaolo, Giovanni, Ignazio, Jessica, Massimo, Maurizio, Michele and Riccardo.

Abstract

Deployable aerobrakes for Earth re-entry capsules may offer many advantages in the near future, including the opportunity to recover on Earth payloads and samples from Space with reduced risks and costs with respect to conventional systems. Such capsules can be accommodated in the selected launcher in folded configuration (optimizing the available volume) and, when foreseen by the mission profile, the aerobrake can be deployed in order to increase the surface exposed to the hypersonic flow and therefore to reduce the ballistic parameter.

The ballistic parameter reduction offers as main advantage the opportunity to perform an aerodynamic de-orbit of the system without the need of a dedicated propulsive subsystem and an atmospheric re-entry with reduced aerothermal and mechanical loads. It makes also possible the use of relatively lightweight and cheap thermal protection materials (like the ceramic fabrics successfully tested in hypersonic plasma wind tunnels). Furthermore, the deployable surface can be modulated for the aerodynamic control of the de-orbit trajectory in order to correctly target the capsule towards the selected landing site. The aerodynamic de-orbit capability can be also exploited to implement alternative methods for the Space debris attenuation, which is becoming more and more important due to the growing number of micro, nano and pico-satellites launched every year in Low Earth Orbit.

The main objective of the present thesis is to perform aerothermodynamic and mission analyses of re-entry systems characterized by deployable heat shields. In particular, the study has been focused on the assessment of the wide range of scientific applications offered by this technology and on the development of technological demonstrators for the experimental verification of its effectiveness and functionality along different flight profiles.

The main outcomes of the study include the preliminary definition of the analyzed missions and of the corresponding deployment mechanism, the aerodynamic and aerothermodynamic study of the system in different flight regimes, from rarefied to continuum.

Table of contents

List of Figures

List of Tables

1 Introduction

In the present Section a brief introduction on deployable aerobrakes is presented. The state-of-the-art technologies, including inflatable systems will be shown and their advantages for Earth re-entry operations underlined. Then some candidate materials for the realization of the aerobrake and potential mission scenarios are discussed. Finally, the opportunities offered by suborbital technology demonstrators are also presented.

1.1 The advantages of deployable aerobrakes for re-entry capsules

In recent years there has been an increasing interest for small Space platforms (micro and nano-satellites), in particular for Earth's environmental protection, prevention of natural disasters and homeland security. Other applications include scientific experiments or technology, Space exploration, observation of the Universe, astrophysics, biology or physical sciences in microgravity.

Reducing size, mass and power implies a significant reduction of costs and of development time, increasing accessibility to Space and sustaining frequent launches. Unfortunately, as a consequence of the miniaturization, these systems require more sophisticated solutions to achieve ambitious scientific and technological goals and to offer the possibility to safely recover on Earth the payload and potential data. These are the main reasons why novel concepts of deployable and inflatable aerodynamic decelerators for de-orbit and re-entry purposes have been proposed in the aerospace community.

These capsules can be in fact more easily accommodated in launch vehicles in folded configuration and, when foreseen by the mission scenario, their aerobrakes can be deployed (or inflated) in order to reduce the capsule ballistic coefficients, defined in Equation 1.1 as the ratio between the capsule mass m and its reference surface S, times the drag coefficient C_D.

$$B = \frac{m}{C_D \cdot S} \tag{1.1}$$

This innovative approach decouples the ballistic coefficient from the launch vehicle mass and volumetric constraints characterizing the conventional, fixed-geometry capsules. In this way the ballistic coefficient can be considered a design parameter, able to provide the opportunity to optimize the entry path.

Figure 1.1 shows the deployable aerobraking capsules within the international re-entry scenario. It is evident that these innovative capsules are intended to perform an almost ballistic re-entry (due to the almost null aerodynamic efficiency) with an extremely low ballistic parameter.

The main reasons of this choice are shown in Figure 1.2. Lower ballistic coefficients, in fact, imply larger decelerations in the upper part of the atmosphere, offering as main advantage the reduction of the aero-thermal peak loads and, consequently, a higher reliability of the re-entry phase.

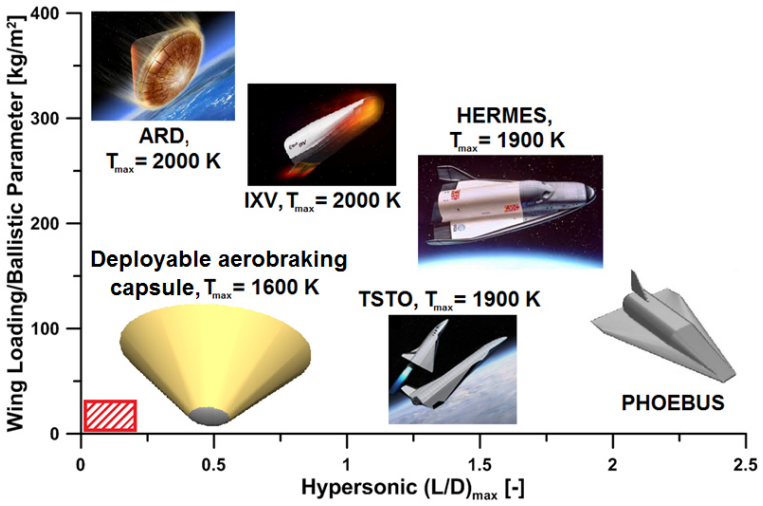

Figure 1.1: Deployable aerobraking capsules within the international scenario in terms of ballistic parameter and aerodynamic efficiency

From Figure 1.2a, in fact, it is evident that a more significant Mach number reduction at higher altitudes can be obtained as the ballistic coefficient decreases. This implies, for lower ballistic coefficient capsules, a more rapid descent at high altitudes and a slower re-entry as the altitude decreases, as depicted in Figure 1.2b. Figure 1.2c and Figure 1.2d finally show the implications of the different dynamic behaviours in terms of mechanical and aerothermal loads, respectively. Roughly, reducing the ballistic coefficient from 100 to 10 kg/m^2, the peak stagnation-point pressure p_0 is reduced by a factor 10, while the peak stagnation-point heat flux $\dot{q}_0$ by a factor 3.

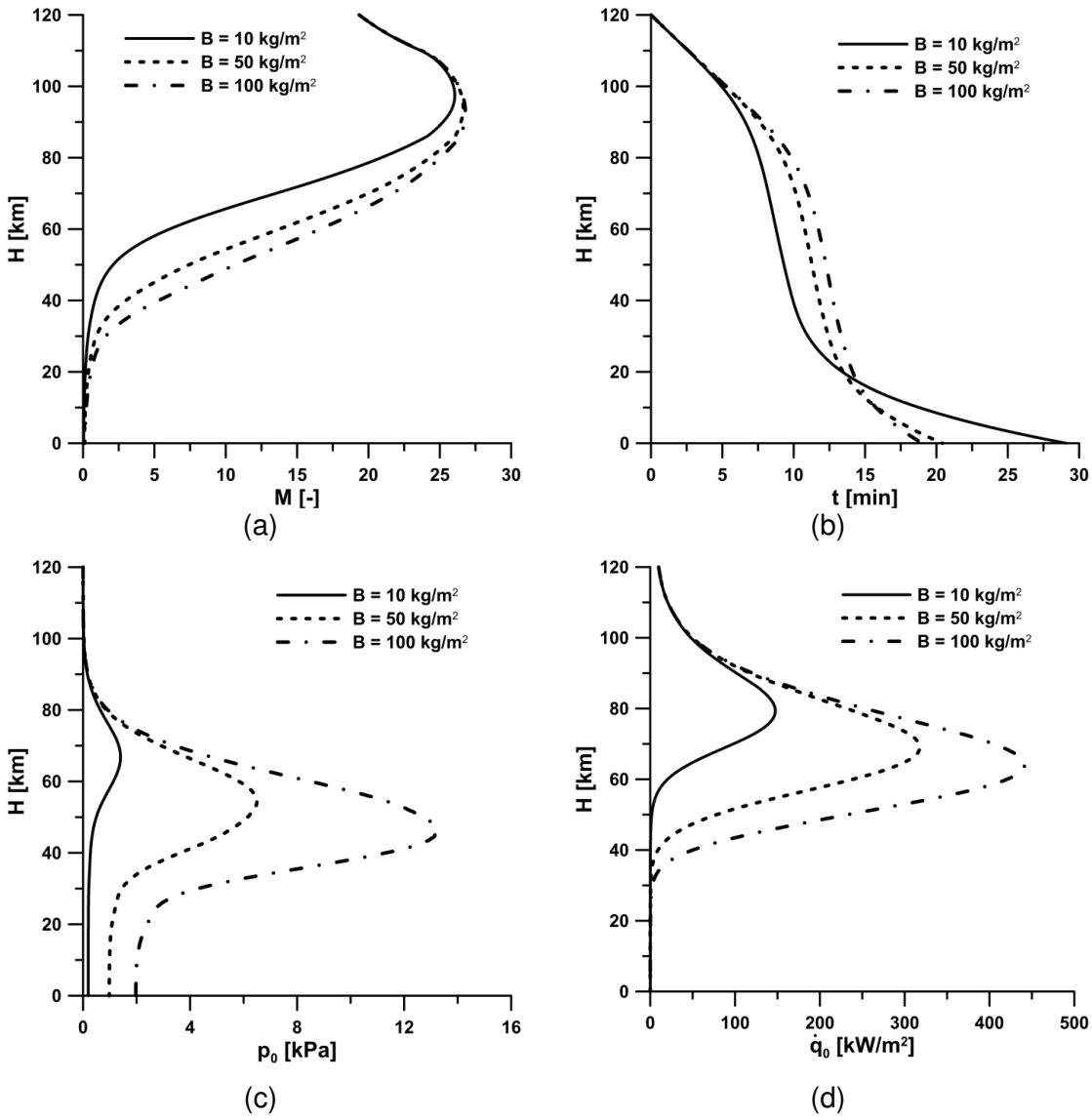

Figure 1.2: Comparison among re-entry trajectories in terms of Mach number (a), flight duration (b), stagnation-point pressure (c) and stagnation-point heat flux (d) for capsules characterized by different ballistic parameters

In addition, deployable aerobrakes may be also useful for aerodynamic de-obits not requiring a dedicated propulsive system. This aspect is fundamental, not only for re-entry capsules, but also for the satellites de-orbit from Low Earth Orbit (LEO) at the end of their lifetime. Due to the increasing problem of the Space debris, in fact, the ability to autonomously remove an object from LEO after the natural duration of its mission appears to be a fundamental advantage, as it will be clarified in the following.

Figure 1.3 shows that, assuming the same initial conditions, an aerodynamic de-orbit performed by means of a deployable decelerator can be almost equivalent, except for the de-orbit duration, to a propulsive de-orbit requiring a velocity change of 150 m/s.

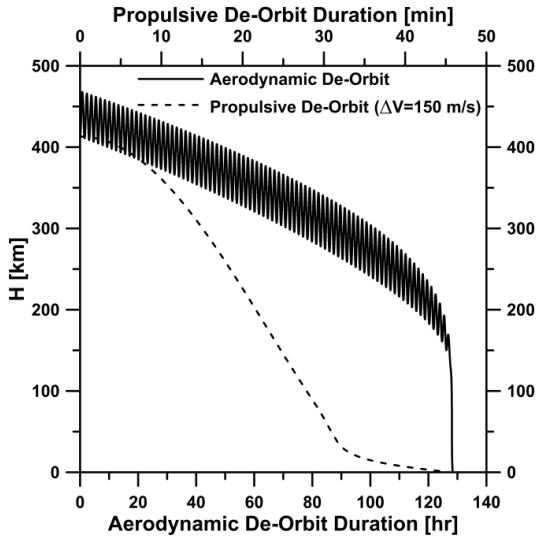

Figure 1.3: Comparison between aerodynamic and propulsive de-orbit phases

Finally, deployable aerobrake can offer the advantage to potentially modulate the reference surface area in order to aerodynamically control the de-orbit phase and correctly target the capsule towards the desired landing site.

1.2 State-of-the-art inflatable and deployable aerobrakes

Examples of inflatable systems proposed and already tested are the Inflatable Re-entry and Descent Technology (IRDT) (1) and the Inflatable Re-entry Vehicle Experiment (IRVE) (2). More recently, Andrews Space has designed and patented an inflatable Nanosat De-orbit and Recovery System for CubeSat payloads (3), (4).
In particular, the IRDT technology shown in Figure 1.4 has been successfully tested in 2000, re-entering the atmosphere after a 6-orbit flight into Space (1).

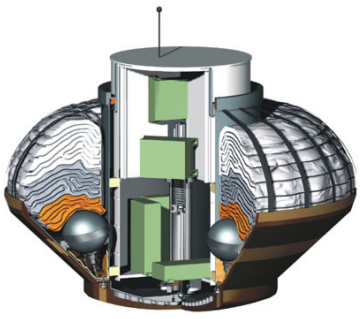

(a)

(b)

Figure 1.4: The IRDT concept in folded configuration (a) and an artistic view of the capsule from Space (b)

A further demonstrating mission in 2002 has not been successful due to a failure in the launcher/payload interface of the Volna rocket, while in 2005 the capsule was not recovered for an unexpected trajectory overshoot.

Figure 1.5(a) shows the assembly of the IRVE-3 re-entry demonstrator successfully tested in 2003. During the flight test the on-board systems inflated some inner tubes, creating the aeroshell depicted in Figure 1.5(b). In that case the heat shield protected a payload consisting in the inflation system, a steering mechanisms, a telemetry equipment and a camera gear.

(a) (b)

Figure 1.5: The IRVE-3 demonstrator assembly (a) and an artistic view of the capsule from Space (b)

Beside those, different concepts for re-entry systems based on mechanically deployable heat-shields exist. In 1990 a deployable capsule was developed using an umbrella-like heat-shield, made of silicon fabrics and called parashield (5). A similar satellite called Bremsat and depicted in Figure 1.6 was studied in 1996 at the University of Bremen (6).

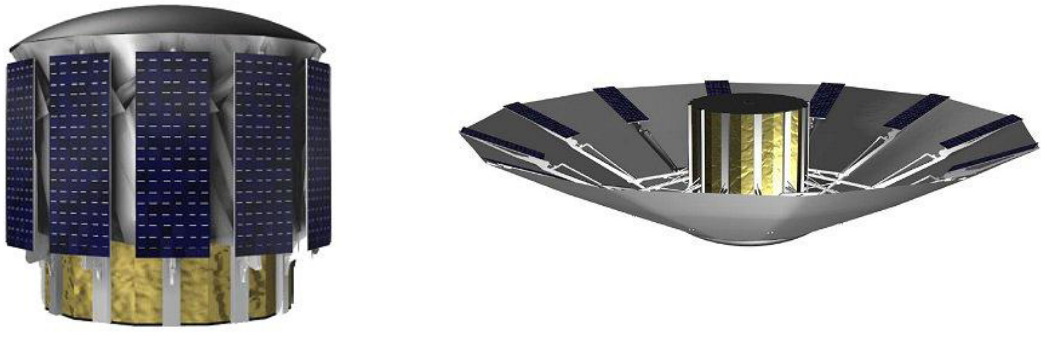

(a) (b)

Figure 1.6: Bremsat re-entry capsule in folded (a) and deployed (b) configurations

1.3 Candidate materials for the Thermal Protection System (TPS)

One of the most important topics regarding the design of this innovative kind of re-entry systems, is the identification and testing of potential materials to be employed for the Thermal Protection System (TPS). In particular, TPS materials have to satisfy a number of requirements, including the ability to withstand high temperatures in a chemically reacting environment, the workability, the low cost and the availability. In addition, the conical part of the heat shield has to be made of a flexible, high temperature resistant material, so that it can be folded and deployed for the different phases of the mission.

For the hemispherical rigid nose cone a number of RESCOR ceramic foams has been considered. Their main thermo mechanical properties are reported in Table 1.1.

Property	RESCOR 310M (99% pure Silica) SiO_2	RESCOR 311 (Alumina Silica) Al_2O_3-SiO_2	RESCOR 750 (Fused Silica) SiO_2
Max. Operating Temp. (°C)	1650	1430	1480
Density (g/cm^3)	0.80	0.80	1.76
Thermal Expansion (10^{-6}/°C)	0.54	5.22	0.54
Elastic Modulus (GPa)	73	---	73
Compressive Strength (kg/cm^2)	84	35	420
Flexural Strenght (kg/cm^2)	36.4	17.5	76.4
Thermal Conductivity (BTU in/Hr/°F/Ft^2)	1.3	2.4	4
Porosity (%)	63	52	19

Table 1.1: Main thermo mechanical properties of RESCOR ceramic foams (7)

Comparing the characteristics reported in Table 1.1, RESCOR 310M resulted particularly suitable for the scope under consideration. In fact, it is characterized by a maximum operative temperature of 1650°C, a low thermal expansion, a high resistance to thermal shocks, a low thermal conductivity. It is also particularly resistant to oxidation. Additional advantages include the possibility to glue the material by means of special adhesives, like RESCOR 901 and to treat it with liquid hardeners, like the RESCOR 901A.

On the other hand, for the flexible part of the TPS, the NEXTEL woven ceramic fabric has been selected. Its main characteristics include the good chemical resistance, the low thermal conductivity, the high resistance to thermal shocks and the low porosity.

Different kind of ceramic fibres can be woven for this kind of fabric, but the most suitable for the aerospace field are the NEXTEL 312 and 440, whose main thermo mechanical properties are reported in Table 1.2.
In particular, NEXTEL 312 has been selected for the lower density and thermal expansion coefficient.

Property	NEXTEL 312	NEXTEL 440
Chemical composition (wt. %)	62.5 Al_2O_3 24.5 SiO_2 13 B_2O_3	70 Al_2O_3 28 SiO_2 2 B_2O_3
Melting point (°C)	1800	1800
Filament diameter (µm)	10-12	10-12
Density (g/cm^3)	2.7	3.5
Thermal Expansion (10^{-6}/°C)	3	5.3
Specific Heat @ 500 °C (cal/g/°C)	0.25	0.27

Table 1.2: Main thermo mechanical properties of NEXTEL ceramic fibres (8)

In the last years the above mentioned materials have been employed to realize technology demonstrators of the concept under investigation to be tested in Plasma Wind Tunnel (PWT) facilities. In particular, the most significant experience in this sense has been realized testing the test article shown in Figure 1.7 through Figure 1.9 in the Scirocco PWT available at the Italian Aerospace Research Centre (CIRA). In particular, in Figure 1.8 and Figure 1.9 the ceramic fabric employed for the flexible part of the demonstrator and its nose cone, respectively, are shown in more details.
The test conditions are reported in Table 1.3, being P_{arc} the arc heater power, H_0 the total enthalpy in the arc heater, $p_{0,arc}$ the total pressure in the arc heater and $\dot{m}$ the air mass flow rate. These parameters led to a stagnation-point pressure and temperature around 7 mbar and 350 kW/m^2, respectively. The stagnation-point heat flux is in particular very close to characteristic re-entry conditions from LEO.

P_{arc} [MW]	H_0 [MJ/kg]	$p_{0,arc}$ [bar]	$\dot{m}$ [kg/s]
10.7	11.5	2.5	0.5

Table 1.3: Test conditions in Scirocco PWT

Figure 1.7: Technology demonstrator for the experimental testing of the concept under investigation in the Scirocco PWT

Figure 1.8: NEXTEL 310 ceramic fabric employed for the flexible part of the demonstrator

Figure 1.9: The nose cone of the demonstrator, made of RESCOR 310

On the basis of this experimental testing (9), it was evidenced that the selected materials are able to withstand maximum temperatures in the order of 1600°C at the stagnation-point (i.e. on the hemispherical nose come made of RESCOR) and of 1400°C on the conical part of the heat shield (i.e. on the NEXTEL fabric).

1.4 Potential orbital mission scenarios

1.4.1 Space mailing to/from the ISS

Space mailing missions to/from the International Space Station (ISS) could be of utmost importance in the present time, due to the urgent need of carrier vehicles for scientific experiments, in particular after the termination of the Space Shuttle programme. In fact, the payload capability of the Russian Soyuz is very limited, while the European ATV, the Russian Progress and the Japanese HTV cargo carriers are only able to deliver experiment to the Station, but not to return them back to Earth.
In Figure 1.10 just one of the feasible scenarios for this kind of mission is depicted. In this case the deployable re-entry capsule contains a scientific experiment and is assumed itself as a piggy back payload of the European Automated Transfer Vehicle (ATV), launched by the Ariane 5. After rendez-vous and docking operations with the ISS, the experimental payload is implemented in the Station to perform its scientific mission. Once the scientific mission is completed, the experiment can be included again in the capsule and safely enter the Earth atmosphere (exploiting the deployable heat shield) for recovery and post-flight inspections and analyses.

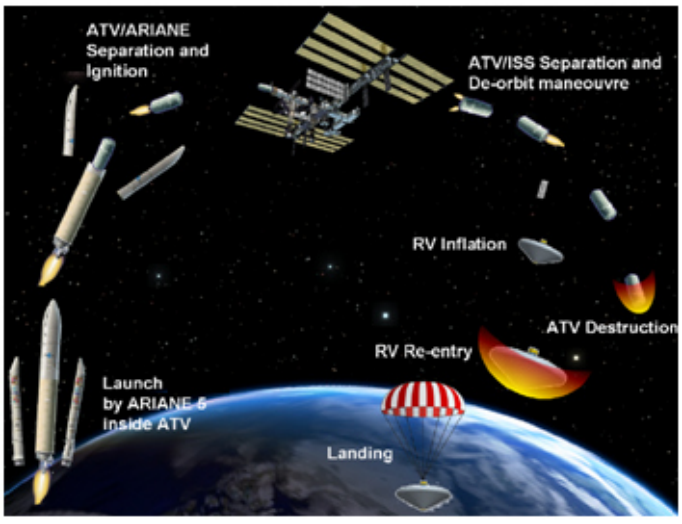

Figure 1.10: Potential scenario for a Space mailing mission to/from the ISS (10)

1.4.2 Orbital scientific mission to/from LEO

The deployable re-entry capsule can be launched as a piggy back payload of a certain launcher directly into LEO for independent orbital missions, whose objective may include:

- microgravity experiments, mainly in the fields of biology and biotechnology;
- exoatmospheric research, including exobiology, Space materials science;
- Space engineering and technology.

Figure 1.11 reports a potential scenario for this kind of mission, taking advantage from the European launcher Vega.

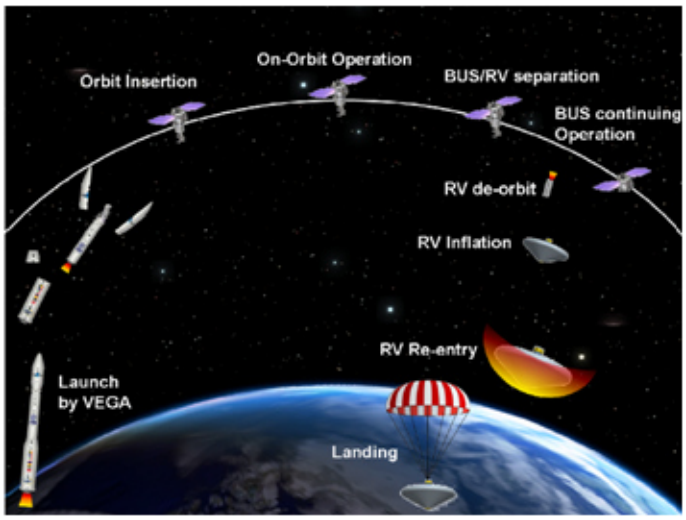

Figure 1.11: Potential scenario for orbital Space mission to/from LEO (10)

1.4.3 Earth observation mission

Further applications for the analyzed system may include Earth observation mission for Earth's environmental protection, prevention of natural disasters and homeland security. In some cases these mission scenarios require very responsive actions, not always feasible for conventional Earth observation satellites, which could require expensive and irreversible orbit changes.

That is the reason why a system able to quickly access to Space into a specific orbit for a dedicated observation mission, to retrieve a large amount of data at high spatial resolution and to safely return on ground can be extremely attractive for the above mentioned applications.

A properly designed deployable re-entry capsule could be very useful for these scopes, in particular using air-launch for orbit injection. In fact, the capsule can be included in folded configuration inside the payload bay of an air-launched rocket and injected into a

certain orbit, easily selectable taking advantage of the flexibility offered by air-launch. In fact (11), (12):

- the airplane may be seen as a Flying Launch Pad able to serve any location on Earth;
- any orbit inclination and launch azimuth can be achieved without expensive out-of-plane orbital manoeuvres;
- the payload can take full advantage of the mother airplane speed, orientation and altitude at the time of the release;
- gravitational and aerodynamic losses are reduced;
- air launch vehicles can operate free of national range scheduling constraints, have minimum launch site requirements and offer the potential for aircraft-like operations, providing responsive launch on demand or launch on schedule.

The orbital injection can be performed at very low altitude (e.g. 150-200 km) to reduce size, mass and cost of optical equipment, optimize the spatial resolution on the ground. In this way the gap between platforms operating up to 50 km (e.g. stratospheric balloons and Unmanned Aerial Vehicles) and traditional satellites for Earth observation, generally operating above 400 km (13) can be bridged. In addition, many kind of orbits can be selected for efficient observations, depending on the specific mission requirement, due to the above mentioned flexibility offered by air launch (14).
Once the mission is completed, after a maximum duration in the order of a few days, the aero-braking system performs an aerodynamic de-orbit manoeuvre, a controlled re-entry into the atmosphere and a soft landing (or splash down) to allow users to retrieve and post-process the data recorded on board (13).

1.4.4 Orbital decay system for Space debris mitigation

The increasing diffusion of standardized nano and pico-satellites, like CubeSat (15) and PocketQube (16), characterized by limited volume and mass and by the use of Commercial Off-The-Shelf (COTS) electronic components, led in the last years to a large decrease of the satellite price tag, producing as a consequence a wider Space accessibility. This enabled regular launch opportunities for several systems in the last decade and many attractive projects are planned for the near future.
On the other hand, as the number of missions increases, the risk produced by the orbital debris, intended as a combination between hazard and vulnerability, dangerously rises. Each year 30-40 launches inject 60-70 new objects into orbit, so that a report of the National Research Council of USA stated in 2010 that the orbital environment has already reached the “Tipping Point”, the threshold of the so called

“Kessler Syndrome”. According to this study, there is enough debris and junk to start a cascade of collisions that will make LEO unusable in decades from now (17).

The dangerous proliferation of Space debris, now amounting to approximately 700000 items circling the Earth, of which only about 21000 larger than 10 centimetres in diameter are tracked, enforces to find out complex solutions for their removal. Some examples in this directions are the Active Debris Removal (ADR) and the On-orbit Satellite Servicing (OSS) (18). ADR is mainly intended to remove objects in LEO (including spent rocket stages), while OSS is typically aimed at refuelling operations and safe lifting to “graveyard” orbits of inoperative GEO-based satellites (18). However, these proposals have to face with a multitude of difficulties due to technical complexity and funding issues. The last problem, in particular, is due to the difficulty of making such proposals commercially attractive, in order to raise funds for their achievement. In addition, legal and political consideration issues concerning the definition of Space debris, jurisdiction, legislation, control and liability related to those ADR and OSS solutions are even more troubling than technical hurdles. Other patented designs for Space debris removal are based on systems intended to create an artificial atmosphere at high altitudes in order to induce satellites decay (19), (20), (21).

It is evident that it is smarter and more affordable not creating remnants rather than clean them up. In this regard, it is of utmost importance to develop safe and low cost de-orbit systems capable to fulfil the growing necessity to avoid on-orbit collisions and reduce Space debris.

In this field RICE project (22) has the objective to develop a low-cost, low-mass flight system able to expose CubeSats to the LEO environment for scientific experiments and to safely recover them for post-flight analyses. RICE system is intended to be launched as a secondary payload and injected into LEO. After 1 to 4 weeks on-orbit, the vehicle is designed to perform a propulsive de-orbit manoeuvre and an atmospheric re-entry with the service module separation from the entry vehicle. Nonetheless, a number of disadvantages characterize this solution, including the need to use a dedicated propulsive subsystem for de-orbit operations and the impossibility to launch the system by means of a standard CubeSat Picosatellite Orbital Deployer (POD).

In the present work the deployable decelerators concept is applied to nano-satellites, in particular to standard CubeSats, in order to exploit the aerodynamic drag to induce the rapid satellite decay after the end of its mission and therefore to contrast the problem of Space debris.

1.5 Design and development of suborbital technology demonstrators

Several research studies and activities on deployable re-entry capsule have been carried out since 2010 at the University of Naples "Federico II" for different mission scenarios (17), (23), (24), (25), (26). However, many of them are recently focused on the development of technology demonstrators for European suborbital sounding rockets. The rational of the this choice is to obtain meaningful experimental verifications of several phenomena connected with the atmospheric re-entry of deployable capsules in mission scenarios characterized by relatively low complexity and then to exploit results for the study and development of analogous systems re-entering from LEO.

Sounding rockets have been used by the European Space Agency (ESA), since the ’80s, as research platforms for scientific experiments performed in microgravity. The microgravity conditions are realized for periods of different duration: the larger the maximum achievable altitude of the suborbital parabolic trajectory, the larger the duration. A schematic view on the different class of European sounding rockets can be found in Figure 1.12.

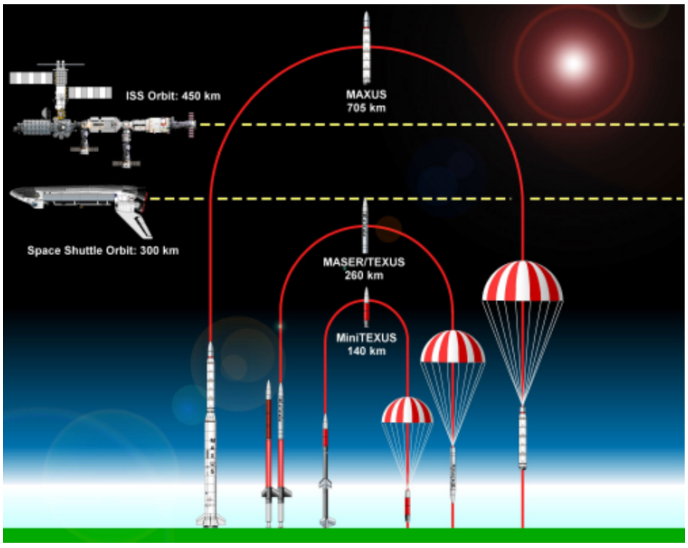

Figure 1.12: ESA sounding rockets (27)

1.5.1 Mission scenario onboard MAXUS

MAXUS is the largest sounding rocket of the ESA. Its main characteristics are summarized in Table 1.4 and in Figure 1.13(b).

In addition to scientific experiments in microgravity, the recent MAXUS-8 mission in 2010 also included a secondary payload, the capsule SHARK (Sounding Hypersonic

Atmospheric Re-entering Kapsule), designed by the Italian Aerospace Research Centre (CIRA) with the support of the European Space Agency (ESA) to test a sharp nose cone made of Ultra High Temperature Ceramic (UHTC) material in hypersonic conditions (28).

During the ascent parabola of the sounding rocket, the capsule was ejected at an altitude of about 150 km, performing a 15 minutes flight in the atmosphere, concluded with the atmospheric re-entry and the final landing. The project proved for the first time the possibility to execute a re-entry test flight by dropping a capsule from the MAXUS sounding rocket.

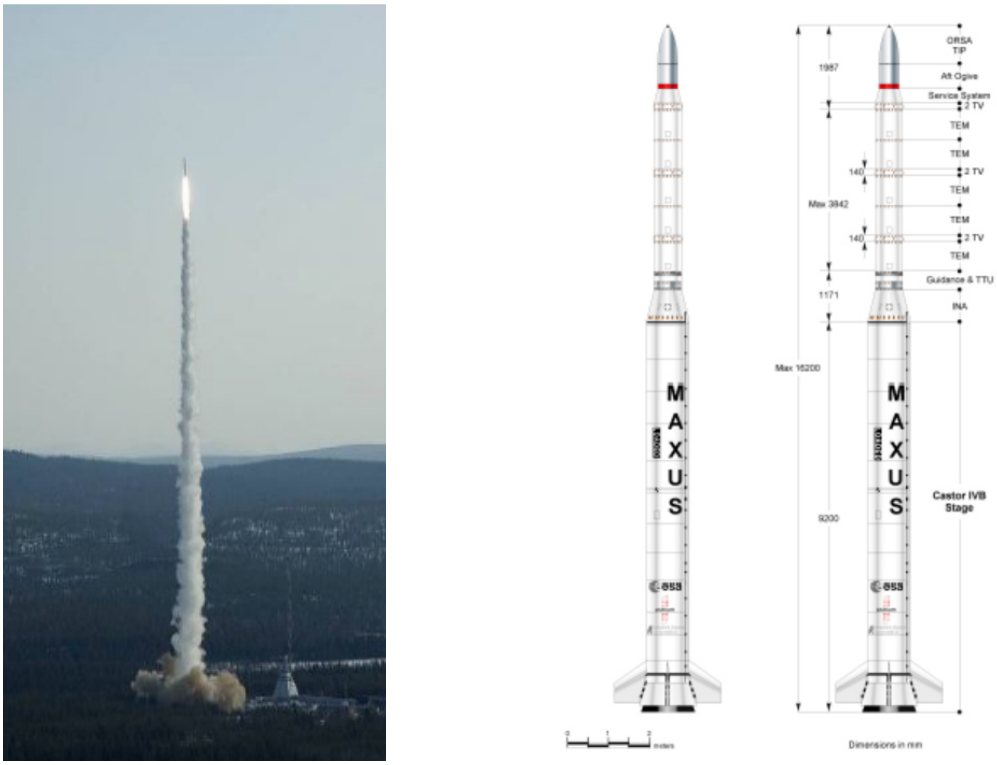

(a) (b)

Figure 1.13: The launch of MAXUS-7 in May 2006 (a) and a schematic drawing of the MAXUS rocket (b) (27)

Microgravity duration [min]	Number of modules	Payload Diameter [cm]	Payload Length [m]	Payload Mass [kg]
12.5	5	64	3.8	480

Table 1.4: Main features of the MAXUS sounding rocket (27)

In the first suborbital scenario analyzed in this work, a technology demonstrator of deployable re-entry capsule is supposed to be ejected from the MAXUS rocket interstage similarly to the SHARK capsule. In particular, the capsule ejection can occur during the ascent phase of the MAXUS sounding rocket, after the payload bay

separation from the booster, also in this case around 150 km altitude. Then the capsule is intended to follow a parabolic trajectory, having an apogee around 720 km, and finally to enter the atmosphere. Despite the lower total energy, in this work it will be shown that the entry path is such that aerothermal and mechanical loads experienced in the descending leg of the trajectory are comparable and even larger than the ones characterizing an orbital re-entry, respectively.

1.5.2 Mission scenario onboard REXUS

The Rocket-borne EXperiments for University Students (REXUS) programme allows students from Universities across Europe to carry out scientific and technological experiments on small sounding rockets. The REXUS program (29) is realised under a bilateral Agency Agreement between the German Aerospace Centre (DLR) and the Swedish National Space Board (SNSB). Every year two rockets are launched from the Esrange Space Centre in northern Sweden. The student experiments are launched on unguided spin-stabilized solid propellant single stage rockets, like the one shown in Figure 1.14 (29). A typical REXUS rocket is composed of an improved Orion motor with exhaust nozzle extension, a tailcan, three stabilizing fins and a motor adapter with an integrated separation system. The standard payload bay include a recovery module, a service module and two experiment modules. One of the two available REXUS rockets has also an ejectable nosecone. In this case there is the opportunity to perform an ejectable experiment, in addition to the standard experiment modules generally employed for microgravity, scientific and technology research.
The total available mass for the student experiments is about 30 kg. REXUS standard configuration mass is reported in Table 1.5.

Vehicle component	Mass [kg]
Improved Orion Motor	125
Propellant	290
Payload (without Experiment Modules)	60
Experiment Modules	40 (max)
Total	515

Table 1.5: REXUS Standard mass budget

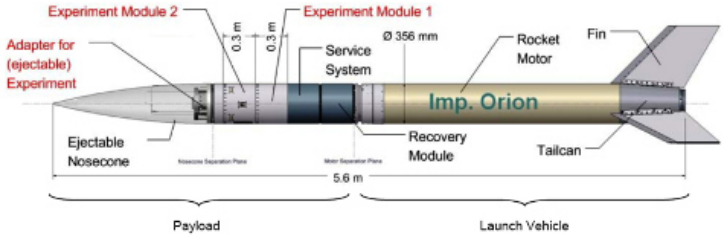

Figure 1.14: REXUS sounding rocket (29)

When performing its mission (29), the rocket accelerates the payload for 26 s with a peak of acceleration of about 20 g during the boost phase. In the initial part of the flight, the rocket has a spin rate of approximately 4 Hz, in order to take advantage from gyroscopic stabilization (in the following part of the mission users can ask for yo-yo de-spinning, if required by their experiment). The motor burnout is usually at an altitude of 23 km. The time of the motor separation depends on the experiment requirements but will not be performed before the nosecone ejection, that can take place at altitudes larger than 55 km. The apogee is between 90 and 100 km, depending on the payload mass. During the descent phase in the lower atmosphere, at an altitude of about 26 km, the payload is decelerated with a maximum acceleration of about 6 g.

The recovery sequence of the payload remaining onboard the rocket is initiated after about 7 min, at an altitude of about 5 km. A parachute system decelerates the payload up to a terminal velocity of about 10 m/s before landing. The main typical events of the flight sequence are reported in Table 1.6, on the basis of the REXUS-3 mission.

Flight event	Flight time [s]	Altitude [km]	Range [km]
Lift-off	T_0	0.0	0.0
Motor burn-out	T_0+26	22.4	3.9
Nosecone ejection	T_0+60	57.4	13.2
Payload/motor separation	T_0+66	62.3	15.5
Apogee	T_0+150	95.8	35.5
Maximum payload deceleration	T_0+270	26.0	-
Stabilizer chute release	T_0+420	5.0	70.0
Main chute release	T_0+447		
Payload landing	T_0+640	0.0	70.0

Table 1.6: Typical Flight Sequence based on the REXUS-3 mission (29)

In this case a flight demonstrator can be ejected from the rocket fairing after the nosecone fairing ejection and before the rocket de-spinning. The experiment has to be

mounted below the ejectable nosecone on an adapter structure (see Fig. 2.13) and, once separated, will perform its entry mission.

Figure 1.15: Example of experiment situated in the nosecone (29)

It is clear that, due to the very low energy level of the rocket suborbital parabola (also when compared to the MAXUS mission scenario described in Section 1.5.1), the demonstrative mission would not be beneficial to test the aerothermodynamic behaviour of the capsule, but could give meaningful results in particular on the aerodynamic stabilization of the system and on the flight testing of the aerobrake deployment mechanism.

2 Numerical models

In this Section the main numerical models implemented for the subsequent analyses will be described. First, the dynamic models employed to obtain re-entry and de-orbit trajectories, landing dispersion and aerodynamic control of the entry path will be shown. Finally, fluid dynamic and Computational Fluid Dynamic (CFD) models used for aerodynamic and aerothermodynamic studies will be presented.

2.1 Dynamic models

2.1.1 Dynamic equations of motion

In order to compute entry trajectories, the set of first order nonlinear ordinary differential Equations 2.1 (30) has been numerically integrated at discrete time-steps and taking advantage of the Euler's method. They represent the dynamic equations of motion for a point mass characterized by three degrees of freedom.

$$\begin{cases} \dfrac{dV}{dt} = -\dfrac{\rho V^2}{2B} - g\sin\gamma + \omega_E^2 r\cos\lambda(\sin\gamma\cos\lambda - \cos\gamma\sin\psi\sin\lambda) \\ V\dfrac{d\gamma}{dt} = \left(\dfrac{V^2}{r} - g\right)\cos\gamma + 2\omega_E\cos\lambda\cos\psi + \omega_E^2 r\cos\lambda(\cos\gamma\cos\lambda - \sin\gamma\sin\psi\sin\lambda) \\ V\dfrac{d\psi}{dt} = -\dfrac{V^2}{r}\cos\gamma\cos\psi\tan\lambda - 2\omega_E(\sin\lambda - \tan\gamma\sin\psi\cos\lambda) - \omega_E^2 r\dfrac{\cos\psi\sin\lambda\cos\lambda}{\cos\gamma} \\ \dfrac{dH}{dt} = V\sin\gamma \\ \dfrac{d\lambda}{dt} = \dfrac{V}{r}\cos\gamma\sin\psi \\ \dfrac{d\Lambda}{dt} = \dfrac{V}{r}\cdot\dfrac{\cos\gamma\cos\psi}{\cos\lambda} \end{cases} \quad 2.1$$

In Equation 2.1 *t* is the time, *V* the velocity, *H* the altitude, γ the flight path angle, *B* the ballistic parameter, *g* the gravity acceleration, *r* the radius of curvature of the trajectory, ψ the azimuth angle, λ the latitude, Λ the longitude and ω_E the Earth's angular velocity. The gravitational acceleration has been assumed to vary according to Equation 2.2, where g_0 is the gravity acceleration at sea level and $R_\oplus$ is the Earth radius.

$$g = g_0\left(\frac{R_\oplus}{R_\oplus + H}\right)^2 \quad 2.2$$

For re-entry trajectories air density, pressure and temperature have been assumed to vary according to the 1976 U.S. Standard Atmosphere Model.
Some engineering calculations can been also performed on the basis of the computed trajectories to estimate some important parameter variation along the entry path. In particular, the stagnation-point heat flux $\dot{q}_0$ can been estimated taking advantages of Equation 2.3, also known as Tauber's engineering formula (31), being ρ the atmospheric density, V the flight velocity and R_c the nose curvature radius.

$$\dot{q}_0 = 1.83 \cdot 10^{-4} \sqrt{\frac{\rho}{R_c}} \cdot V^3 \qquad 2.3$$

The radiative equilibrium temperature profile corresponding to the convective heat flux computed at the stagnation-point can be calculated solving with respect to the wall temperature T_w the quartic Equation 2.4. The equation has been solved by means of the Newton's method, being c_p the specific heat, σ the Stefan-Boltzmann constant and ε the surface emissivity.

$$\dot{q}_0 \cdot \left(1 - \frac{c_p \cdot T_w}{V^2/2}\right) - \sigma \cdot \varepsilon \cdot T_w^4 = 0 \qquad 2.4$$

Furthermore, the stagnation pressure p_0 on the nose has been evaluated according to Equation 2.5 (being ρ the atmospheric density and V the flight velocity), since the pressure coefficient can be considered equal to 2 in hypersonic regime, according to Newton's theory (30).

$$p_0 = \rho \cdot V^2 \qquad 2.5$$

2.1.2 Period reduction model for orbital decay

The orbital decay phase has been studied implementing both the dynamic equations described in Section 2.1.1 and a model based on the orbital period reduction due to the atmospheric drag (32).
The period reduction model, reported in Equation 2.6, foresees that the orbiting object under consideration flies around the Earth along circular orbits, whose radius (and therefore whose orbital period) is step-by-step reduced by the influence of the aerodynamic drag. The latter factor depends, on the one hand, on the object ballistic

parameter *B* and, on the other hand, by the atmospheric density, assumed to vary, for altitudes larger than 175 km, according to the exponential law reported in Equation 2.7. In Equation 2.6 *P* is the orbital period, *r* is the orbital radius and $\mu_{\oplus}$ the Earth's standard gravitational parameter.

$$\begin{cases} \frac{dP}{dt} = -3\pi\frac{\rho r}{B} \\ r = \sqrt[3]{\frac{P^2\mu_{\oplus}}{4\pi^2}} \end{cases} \quad 2.6$$

$$\rho = \rho_0 e^{-\frac{H-175}{SH}} \quad 2.7$$

In Equation 2.7 ρ_0 is the reference density at 175 km altitude and *SH* is a scale height, strongly influenced by the atmospheric temperature, and therefore by the solar activity. In fact, the solar X-rays impinging on the Earth are absorbed at the base of the thermosphere (around 120 km) and this effect produces the atmospheric heating, which propagates upward from this level. The solar 10.7 cm radio flux is generally employed to directly correlate the total solar X-ray flux producing this effect with the scale height. This flux can vary from 65 to over 300 Solar Flux Units (SFU) within a 11-years cycle (1 SFU = 10^{-22} W/m^2/Hz).

This model has been verified cross-checking its results with the analogous ones obtained thanks to the numerical integration of the dynamic equations of motion, for a capsule characterized by the ballistic parameter reported in Table 2.1. The range of altitudes considered varies from 270 and 100 km, while the drag coefficient has been preliminarily assumed constant and equal to 2, due to the high rarefaction level (26).

m [kg]	S [m^2]	C_D [-]	B [kg/m^2]
20	1.0	2.0	10

Table 2.1: Capsule ballistic parameter

Figure 2.1 shows the comparison of the results obtained by the two different approaches, in both cases assuming an Average Solar Activity (ASA). Despite the larger level of approximation for the period reduction method, the results agreement appears very satisfactory.

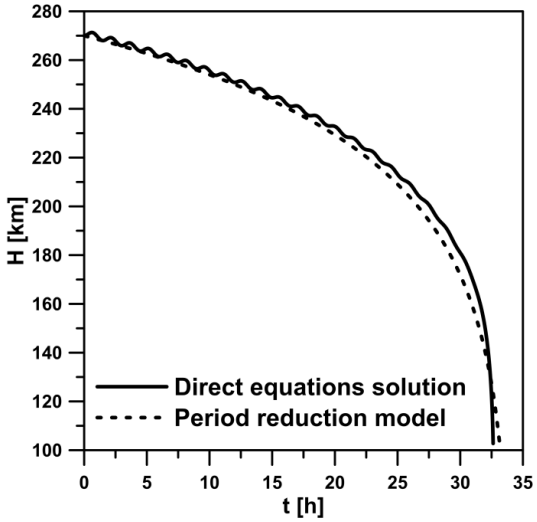

Figure 2.1: Comparison between the period reduction model and the numerical integration of the dynamic equations of motion for a capsule having a ballistic parameter of 10 kg/m^2

Finally, a similar validation between the two methods has been applied to the orbital decay from 300 to 180 km altitude, but considering a ballistic parameter in the order of 160 kg/m^2. Calculation results reported in Table 2.2 assume three different values for the solar activity: Minimum Solar Activity (MiSA), Average Solar Activity (ASA) and Maximum Solar Activity (MaSA).

	Satellite lifetime [days]		
	MiSA	ASA	MaSA
Direct equation solution	74.8	40.8	27.5
Period reduction model	77.8	39.3	26.8

Table 2.2: Satellite lifetime comparison for different solar activities

Also in this case Table 2.2 shows that results obtained using the “Period reduction model” do not differ more than 5% from the “Direct equation solution”. It has to be specified that the validation test cases reported in this Section can be highly representative of the orbital decay for a variable geometry aerobraking capsule. The fist example considers the aerobrake in deployed configuration, whilst the second one assumes the folded aerobrake.

2.1.3 Monte Carlo analysis for landing dispersion

During a re-entry flight a huge number of uncertainties can be able to vary the nominal vehicle entry path. This can affect the re-entry phase and, in particular, the precise determination of the landing site. Most of these uncertainties are linked to the vehicle itself (e.g. uncertainties on the aerodynamic coefficients, mass distribution, reference

surface, parachute activation and so on). Some other disturbances, on the other hand, are due to the external environment (e.g. connected with the atmospheric density, the presence of wind).

In order to reduce risks derived from the capsule landing and to assess the probability to correctly recover the system in a determinate geographical area, it can be therefore very important to perform re-entry calculations taking into account these uncertainties from a statistical point of view. The typical approach consists in Monte Carlo analyses for the evaluation of the landing dispersion and of the aerothermal and mechanical loads variation on the basis of random input parameters (33), (34), (35).

First, a number of potential uncertainties have been identified for the missions under investigation, namely, the capsule mass, its reference surface, the vehicle drag and lift coefficients, the initial altitude, velocity and flight path angle, the density profile during re-entry, the influence of the wind on the aerodynamic forces. It is worth underlining that many other factors should be taken into account for a more detailed analysis, but the objective of the Monte Carlo analysis reported in this work is mainly to provide an order of magnitude for landing dispersion and for loads variances in a preliminary phase of the study.

As second step, random Gaussian distributions are independently generated for all the input parameters, on the basis of their average values and 3-σ standard deviations. In this work each distribution consists in 1000 off-nominal cases, representative of 1000 pseudo-experiments (i.e. statistical tests).

Then, for each i^{th} statistical test case, a re-entry trajectory is evaluated assuming the simultaneous effect of all the random parameters calculated at the i^{th} step. Finally, collecting the results deriving from every randomly initialized trajectory, some significant output parameters (e.g. downrange, maximum aerothermal and mechanical loads) have been obtained and plotted. As the number of test cases increases, also the output parameters tend to assume normal distributions and the analysis reliability increases.

2.1.4 Aerodynamic control of de-orbit trajectories

The uncertainties discussed in Section 2.1.3, in particular the ones connected with the atmosphere properties, can affect not only the re-entry phase, but also the de-orbit path, as it will be clarified in this Section. As also mentioned in Section 1.1, one of the advantages of a deployable re-entry capsule consists in the possibility to modulate the reference surface area during the atmospheric re-entry to control the trajectory and target the payload into a desired un-populated area for safe landing and recovery. In

particular, the control can be performed in such a way to cope with the differences between the trajectory detected by on board instrumentation and the nominal one.
In order to show the importance of such a kind of control, in particular for the de-obit phase, the shift for the entry interface point (conventionally at 120 km altitude) has been calculated and depicted in Figure 2.2 for an equatorial re-entry trajectory from LEO (assuming the ballistic parameter reported in Table 2.1). Figure 2.2 shows the entry point shift as a function of the solar radio flux discrepancy from the nominal conditions. It is evident that even small uncertainties in the above mentioned parameter can produces a huge error in the entry interface point and, as a consequence, a huge uncertainty on the landing site location.

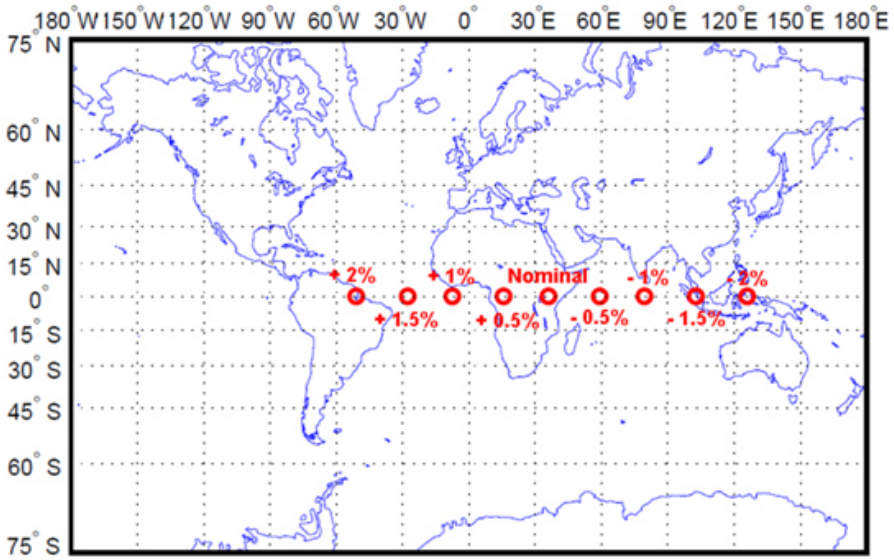

Figure 2.2: Entry interface point shift for different values of the solar radio flux error (with respect to the average conditions)

In the de-orbit phase, an aerodynamically-based control has been therefore considered in the present work. At each time step, in particular, a surface increment or decrement ΔS has been applied to the reference surface, according to Equation 2.8 (being H and H_{nom} the actual and the nominal altitude and Λ and Λ_{nom} the actual and the nominal longitude, respectively).

$$\Delta S = k_1 \cdot (H - H_{nom}) + k_2 \cdot (\Lambda - \Lambda_{nom}) \qquad 2.8$$

In the previous equation the surface area correction has been assumed to be proportional to the altitude and longitude discrepancy between the nominal trajectory and the one detected by on-board instrumentation. The constant gains have been assumed equal to 0.1.

2.2 Fluid dynamic and Computational Fluid Dynamic (CFD) models

2.2.1 Fluid dynamic models for hypersonic flows

During hypersonic flights, due to the high total enthalpy and to the presence of strong shock waves, the huge energy conversion in sensible enthalpy can cause dissociation and, in more extreme conditions (which will not be considered in the present work) even ionization phenomena. In any case the perfect gas model is no longer applicable and the air has to be modelled as a mixture of reacting gases in chemical non-equilibrium.
In this case the fluid dynamic governing equations are the following (36):

- Continuity

$$\frac{\partial \rho}{\partial t} + \underline{\nabla} \cdot \left(\rho \underline{V}\right) = 0 \qquad 2.9$$

where ρ is the mixture density and V the mass velocity of the fluid mixture.

- Species

$$\frac{\partial \rho_i}{\partial t} + \underline{\nabla} \cdot \left(\rho_i \underline{V}\right) + \underline{\nabla} \cdot \left(\rho D_i \underline{\nabla} \alpha_i\right) = \omega_i \qquad 2.10$$

where ρ_i, D_i, α_i and ω_i are the density, the mass diffusivity, the mass fraction and the mass production of the i^{th} species of the mixture, respectively.

- Momentum

$$\frac{\partial \left(\rho \underline{V}\right)}{\partial t} + \underline{\nabla} \cdot \left(\rho \underline{V}\,\underline{V}\right) + \underline{\nabla} p = 2\underline{\nabla} \cdot \left[\mu \cdot \left(\underline{\nabla V}\right)_0^s\right] \qquad 2.11$$

where p is the mixture density and pressure and μ the dynamic viscosity. For each species the perfect gas model is applicable, while the mixture pressure p can be calculated by means of the Dalton's law reported in Equation 2.12 as a function of the partial pressures p_i of the N species considered.

$$p = \sum_{i=1}^{N} p_i \qquad 2.12$$

- Energy

$$\frac{\partial(\rho E)}{\partial t}+\underline{\nabla}\cdot\left[(\rho E+p)\underline{V}\right]=\underline{\nabla}\cdot\left[\lambda\underline{\nabla}T+2\mu\cdot\left(\underline{\underline{\nabla V}}\right)_0^s\cdot\underline{V}+\sum_{i=1}^{N}h_i\cdot\left(\rho D_i\underline{\nabla}\alpha_i\right)\right] \qquad 2.13$$

where E, λ and T are the total energy, the thermal conductivity coefficient and the temperature of the mixture, while h_i the sensible enthalpy per unit mass of the i^{th} species of the mixture.

The source term for the i^{th} chemical species in Equation 2.10 is the sum of the molar rate of creation/destruction of the i^{th} species over the R reactions that the species participate in, as shown in Equation 2.14, being $\mathcal{M}_i$ the molecular weight of the i^{th} species.

$$\omega_i=\mathcal{M}_i\sum_{r=1}^{R}\widehat{\omega}_{i,r} \qquad 2.14$$

The creation/destruction rate of each species can be obtained by means of the Equation 2.15.

$$\widehat{\omega}_{i,r}=\Gamma\cdot\left(\nu''_{\mathrm{i,r}}-\nu'_{\mathrm{i,r}}\right)\cdot\left(\mathrm{k_{f,r}}\prod_{\mathrm{j=1}}^{\mathrm{N_r}}\left[\mathrm{C_{j,r}}\right]^{\eta'_{\mathrm{j,r}}}-\mathrm{k_{b,r}}\prod_{\mathrm{j=1}}^{\mathrm{N_r}}\left[\mathrm{C_{j,r}}\right]^{\eta''_{\mathrm{j,r}}}\right) \qquad 2.15$$

In Equation 2.15 N_r is the number of chemical species in the r^{th} reaction, $C_{j,r}$ the molar concentration of each reactant and product in the r^{th} reaction, $\nu'_{i,r}$ and $\nu''_{i,r}$ are the stoichiometric coefficients for reactant and product species i in the r^{th} reaction, $k_{f,r}$ and $k_{b,r}$ the forward and the backward rate constant for reaction r, $\eta'_{j,r}$ and $\eta''_{j,r}$ the forward and backward rate exponent for each j^{th} reactant and product in reaction r and Γ takes into account the third body efficiency on the reaction rate.

Finally, the forward rate constant for the generic r^{th} reaction can be found by means the Arrhenius equation labelled as Equation 2.16.

$$k_{f,r}=A_r\cdot\mathrm{T}^{\beta_\mathrm{r}}\cdot\mathrm{e}^{-\mathrm{E_r}/\mathcal{R}\mathrm{T}} \qquad 2.16$$

In Equation 2.16 A_r is called pre-exponential factor, β_r temperature exponent, E_r is the activation energy for the r^{th} reaction and $\mathcal{R}$ the universal gas constant (from a dimensional point of view the ratio $E_r/\mathcal{R}$ is a temperature and can be also referred as

activation temperature for the r^{th} reaction). If the reaction is reversible, the backward rate constant for the r^{th} reaction is computed from the forward rate constant using the equilibrium constant for the reaction.

2.2.2 CFD models

The governing equations presented in Section 2.2.1 can be also written in a generic vector form as shown in Equation 2.17.

$$\frac{\partial \underline{U}}{\partial t} + \nabla \cdot \left(\underline{F} - \underline{G}\right) = \underline{S} \tag{2.17}$$

In Equation 2.17 $\underline{U}$ is the unknown vector:

$$\underline{U} = \begin{bmatrix} \rho_1 \\ \rho_2 \\ \vdots \\ \rho_i \\ \rho\underline{V} \\ \rho E \end{bmatrix} \tag{2.18}$$

$\underline{F}$ is the non dissipative part of the flux vector, that is:

$$\underline{F} = \begin{bmatrix} \rho_1\underline{V} \\ \rho_2\underline{V} \\ \vdots \\ \rho_i\underline{V} \\ \rho\underline{V}\underline{V} + p\underline{\underline{U}} \\ \rho E\underline{V} + p\underline{V} \end{bmatrix} \tag{2.19}$$

where $\underline{\underline{U}}$ denotes the singular tensor. $\underline{G}$ represent the dissipative part of the flux vector:

$$\underline{G} = \begin{bmatrix} J_1 \\ J_2 \\ \vdots \\ J_i \\ \underline{\underline{\tau_d}} \\ \lambda\nabla T + \tau_d \cdot \underline{V} - \sum_i h_i J_i \end{bmatrix} \tag{2.20}$$

being J_i the mass diffusivity of the i^{th} species and τ_d the dissipative part of the stress tensor.

Finally, $\underline{S}$ is the production term:

$$\underline{S} = \begin{bmatrix} \omega_1 \\ \omega_2 \\ \vdots \\ \omega_i \\ 0 \\ 0 \end{bmatrix} \qquad 2.21$$

This system of equation with suitable boundary conditions has been numerically solved for aerodynamic and aerothermodynamic analyses taking advantage of the software FLUENT (37). The program is based on the solution of the discretized Equation 2.17 by means of a finite volume technique. In each control volume, Equation 2.17 can be written as reported in Equation 2.22, being V_C the control volume considered and A_i one of its faces (see Figure 2.3).

$$\frac{\partial \underline{\tilde{U}}}{\partial t} + \frac{1}{V_C} \sum_i \left(\underline{\hat{F}} - \underline{\hat{G}} \right)_i \cdot \underline{A}_i = \underline{\tilde{S}} \qquad 2.22$$

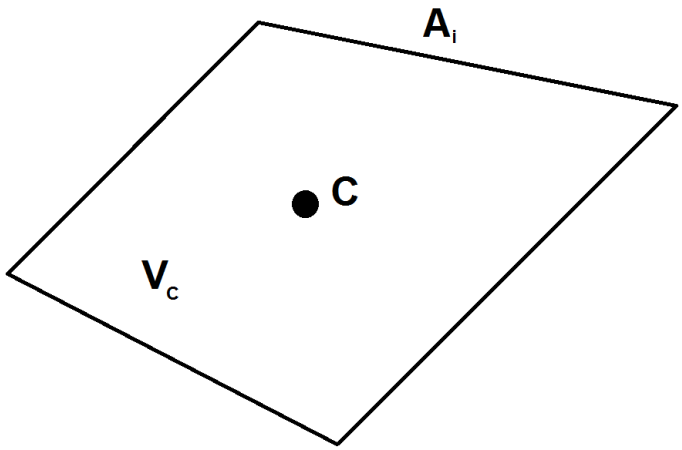

Figure 2.3: Example of control volume

Finally, in Equation 2.22:

$$\underline{\tilde{U}} = \frac{1}{V_C} \int_{V_C} \underline{U} dV_C \ , \ \underline{\hat{F}}_i = \int_{A_i} \underline{F} dA_i$$
$$\underline{\hat{G}}_i = \int_{A_i} \underline{G} dA_i \ , \ \underline{\tilde{S}} = \frac{1}{V_C} \int_{V_C} \underline{S} dV_C \qquad 2.23$$

In the present work, a density-based, time implicit, numerical resolution scheme, adopting the Advanced Upstream Splitting Method (AUSM+) scheme for convective numerical fluxes, has been used.

The density-based approach consists in the simultaneous solution of the continuity, momentum and energy equations, while the pressure field is determined from the equation of state. Since the governing equations are non-linear (and coupled), a number of iterations of the solution loop must be performed before a converged solution is obtained. The non-linear governing equations are linearized to produce a system of equations for the dependent variables in every computational cell. The resultant linear system is then solved to furnish an updated flowfield solution at each iteration.

The governing equations have been linearized by means of an implicit formulation. An implicit scheme foresees that, for a given variable, the unknown value in each cell is computed by means of a relation including both existing and unknown values from neighbouring cells. Each unknown will therefore appear in more than one equation in the system and these equations must be solved simultaneously to give the unknown quantities.

For the mission scenarios characterized by relatively high energies (i.e. for LEO re-entry missions), air has been modelled as a 5 species reacting mixture (O_2, O, N_2, N, NO) and constants in Equation 2.16 have been set according to the 5-reactions Park's model (38), (39), as reported in Table 2.3. In Table 2.3 *M* represents a generic third body not directly participating in the reaction.

Reaction	$A_{f,r}$ [m^3/(kmol·s)]	$\beta_{f,r}$	E_r [J/kmol]	3rd body efficiency
$O_2 + M \leftrightarrow 2O + M$	$2.0 \cdot 10^{18}$	-1.5	$4.94 \cdot 10^8$	O_2=1, O=5, N_2=1 N=5, NO=1
$N_2 + M \leftrightarrow 2N + M$	$7.0 \cdot 10^{18}$	-1.6	$9.40 \cdot 10^8$	O_2=1, O=4.28, N_2=1 N=4.28, NO=1
$NO + M \leftrightarrow N + O + M$	$5.0 \cdot 10^{12}$	0	$6.28 \cdot 10^8$	O_2=1, O=22, N_2=1 N=22, NO=22
$NO + O + M \leftrightarrow O_2 + N + M$	$2.4 \cdot 10^6$	1	$1.61 \cdot 10^8$	-
$N_2 + O + M \leftrightarrow NO + N + M$	$1.8 \cdot 10^{11}$	0	$3.19 \cdot 10^8$	-

Table 2.3: Reaction rate parameters based on the Park's model (39)

On the other hand, for entry missions along suborbital trajectories, air has been assumed as an ideal gas, considering that the total flow enthalpy in that cases is not able to trigger significant dissociation phenomena.

In addition, a laminar viscous model has been assumed. In any case the transport properties (i.e. the dynamic viscosity, the thermal conductivity and the mass diffusivity) have been evaluated according to the kinetic theory of gases (40).

Different kind of boundary conditions have been used:

- pressure far-field in order to model a free stream condition dictated by re-entry trajectories;
- pressure outlet for the downstream surfaces;
- wall conditions for the surface of the capsule;
- axis/symmetry conditions to model 2D axisymmetric and 3D symmetric problems, respectively.

In particular, on walls non-slip conditions and constant temperatures of 300 K were set. The latter setting has been assumed to have a conservative estimation for the convective heat fluxes.

Also, for relatively high energy scenarios, CFD analyses have been performed setting either a Non-Catalytic (NC, see Equation 2.24) and a Fully-Catalytic (FC, Equation 2.25) condition on the walls. In Equation 2.24 α_i represents the concentration of the i^{th} species and n the direction normal to the wall while, in the first relation in Equation 2.25, α_{prod} stands for the concentration of the species generated by the oxygen and nitrogen dissociation reactions.

Non-Catalytic condition (NC)

$$\left(\frac{\partial \alpha_i}{\partial n}\right)_w = 0 \qquad 2.24$$

Fully-Catalytic condition (FC)

$$\begin{cases} \left(\alpha_{prod}\right)_w = 0 \\ \left(\alpha_{O_2}\right)_w = 0.22 \\ \left(\alpha_{N_2}\right)_w = 0.78 \end{cases} \qquad 2.25$$

In Fully-Catalytic conditions the energy stored in the chemical degrees of freedom is completely released at the wall, causing additional heating. For a Non-Catalytic surface, this additional heating does not occur at all. The above two conditions represent the best and the worst possible case from the thermal heating point of view, but they are not necessarily encountered in practice. Generally, real materials have an intermediate catalycity.

3 Re-entry mission from LEO

In this Section some possible re-entry missions for deployable aerobraking systems from Low Earth Orbit (LEO) will be presented. In particular, the attention will be focused on deployable aerobrakes applied to CubeSat satellites for de-orbit and re-entry purposes and on air-launched systems for Earth observation missions.

3.1 System configurations

3.1.1 General configuration

The typical capsule configuration under consideration may consist of a cylindrical structure containing all the subsystems necessary for the on-orbit mission and for the re-entry phase, umbrella-like frameworks, off-the-shelf ceramic fabrics (e.g. NEXTEL) for the conical deployable heat shield and available ceramic materials (e.g. RESCOR, silica, alumina or zirconia) for the rigid hemispherical nose.
The necessary subsystems include parachute, beacon, OBDH, AOCS, IMU, GPS receiver, batteries and sensors. The system launch mass is intended to be only few tens of kilograms so that the entire platform can be launched as a secondary payload of a launch vehicle or with a smaller air-launched rocket. After completing the on-orbit mission, the system performs an aerodynamic de-orbit manoeuvre taking advantage of the deployable structure.
After aerocapture the separation of a satellite bus can be also foreseen, so that the capsule can safely re-enter through the atmosphere and, after landing, its payload can be recovered and/or delivered for post flight inspection and experimentation. The small mass/surface area ratio results in terminal velocities of the order of 10 m/s, requiring only terminal decelerators (e.g. small parachutes) or shock absorbers to mitigate the landing impact.
Figure 3.1 shows possible vehicle configurations in the different phases of the mission.

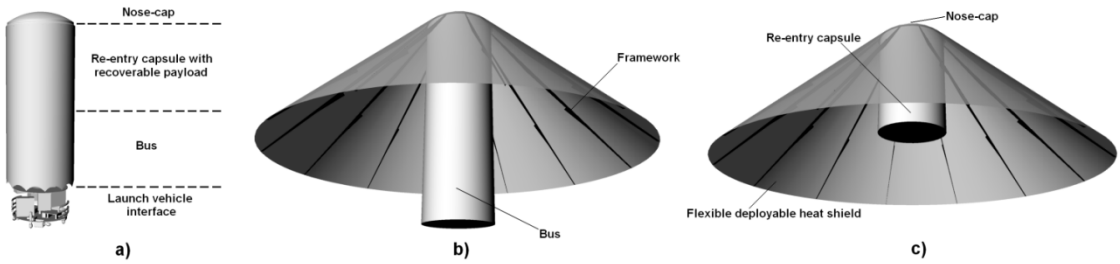

Figure 3.1: Capsule concept in launch (a), de-orbit (b) and re-entry (c) configuration

3.1.2 Aerobrake and re-entry modules on CubeSats

In the present Section novel concepts of deployable aerodynamic decelerators for standard CubeSats are shown. In particular, two different configurations are proposed.
As also discussed in Section 1.4.4, the first class of deployable aerobrakes is intended to increase the satellite cross sectional surface, in order to strongly reduce its de-orbit lifetime and therefore to contrast the problem of Space debris connected with the increasing number of micro, nano and pico-satellites into LEO. In the following, this configuration will be labelled as CubeSat End-of-Life System (CELS).
The second concept, defined CubeSat De-orbit and Recovery System (CDRS), is based on a deployable heat shield also able to provide a safe recovery of payloads and potential data from LEO at low cost. It is clear that in principle these concepts can be applied, in general, to micro and nano-satellites.
Since the objective for CELS configuration is to de-orbit the satellite without recovery, the umbrella-shaped aerobrake is not designed to withstand the aerothermal and mechanical loads acting during the atmospheric entry. In this regard the material requirements are not constraining and therefore simple and lightweight structures can be realized. As depicted in Figure 3.2, the CELS unit fulfils the maximum requirement of 11.3 centimetres in height, prescribed for Standard CubeSats (15) and, by means of deployable ribs, a reference diameter around 55 centimetres is reached. In this case the attached 2U standard CubeSat units represent the satellite payload.

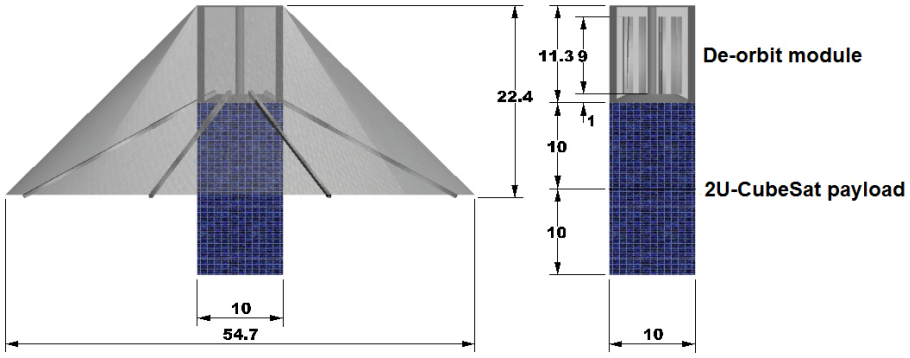

Figure 3.2: Preliminary concept for the CubeSat End-of-Life System (CELS) unit

On the other hand, the proposed CubeSat De-orbit and Recovery System (CDRS) concept enables to safely protect the CubeSat modules during atmospheric re-entry allowing it to be recovered. In addition, it can be considered as a highly innovative system that shows, together with analogous inflatable solutions (3), (4), undoubted advantages if compared with solutions like the ones offered by RICE project (22).

In fact, unlike the RICE, the design solution proposed in the present thesis would allow users to launch the system by means of a standard CubeSat Picosatellite Orbital Deployer (POD) and to avoid propulsive devices for de-orbit operations.

For CDRS the aerobrake structure, strengthened by the presence of an high temperature heat shield, is intended to protect the payload from the re-entry environment for its final recovery. As in the CELS case, after completing the on-orbit mission, the nano-satellite performs an aerodynamic de-orbit manoeuvre using the deployable structure. In addition, unlike the concept proposed by Andrews Space (3), (4), once the umbrella-like framework is opened, the reference surface can be modulated, changing the half-cone angle, to control the trajectory and target the payload into an un-populated area for landing and recovery, as widely discussed in Section 2.1.4. Thus the capsule safely re-enters through the atmosphere and, after landing, the payload is delivered for post flight inspections and experimentations. Furthermore, due to the small mass-over-surface ratio, it can be thought to use an integrated crushable structure, positioned between the heat shield and the payload, to increase the recovery reliability. The folded Thermal Protection System (TPS) is 1U sized, while the second unit is dedicated to a service module. In this case, realistically, only one unit can be dedicated to the payload to execute on-orbit operations (e.g. earth observation, microgravity, technology, life science, etc.). In particular the service module is intended to support orbital activities, to activate the heat shield deployment and to manage the aerodynamic control along the entire trajectory.

As shown in Figure 3.3, the CDRS requires a spherical nose in ceramic materials (like C-SiC with special ceramic oxide coatings) in order to withstand thermal and mechanical loads acting around the stagnation-point and a flexible high temperature material for the conical part of the heat shield.

The class of materials which can be used for the latter component strongly depends on the mission profile (i.e. on the temperature distributions encountered along the re-entry path). For maximum temperatures on the conical part of the heat shield lower than 1200°C, multi-layer stitched blanket insulations, like the one described in (41), can be employed. The aerobrake described in (41) includes a first layer of cloth material that is resistant to temperatures up to 1400°C. It is followed by a sheet of non-porous metal foil and by a layer of flexible insulating felt material. A second sheet of non-porous foil optionally comes next, followed by a second layer of cloth material. The second cloth layer may be the same as the front one or may be less heat resistant to about 1000°C (41). A thread material that is adapted to withstand elevated temperatures is used to sew or stitch the two layers of cloth material, the layer of insulating material and the non-porous foil together (41).

Considering that in the present work, like it will be shown in the following Sections, maximum temperatures on the conical part of the heat shield can be larger than 1200°C, flexible ablators for hypersonic decelerators, like the ones in course of development at NASA Ames Research Center (42), able to withstand heat fluxes in the order of MW/m^2, can be used. They mainly consist of PICA and SIRCA cousins with flexible matrixes made of silica and carbon-based felts or cloths, polymer-based felts and organic/inorganic blended materials.

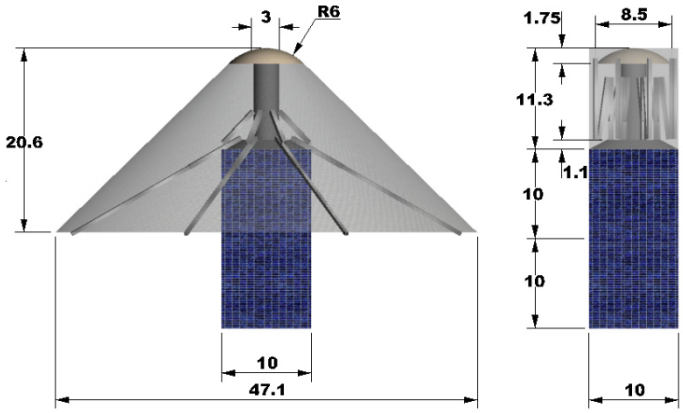

Figure 3.3: Preliminary concept for the CubeSat De-orbit and Recovery System (CDRS) unit

3.1.3 Avio-launched system for Earth observation missions

In this Section a possible configuration for an air-launchable micro-platform, able to autonomously de-orbit and re-enter from LEO at the end of its mission, is presented. As shown in Figure 3.4, the main components of the capsule are a deployable structure for efficient aerodynamic de-orbit and re-entry operations and a payload compartment able to accommodate instruments for a large variety of missions, including Earth observation. Typical dimensions are reported in Figure 3.5.

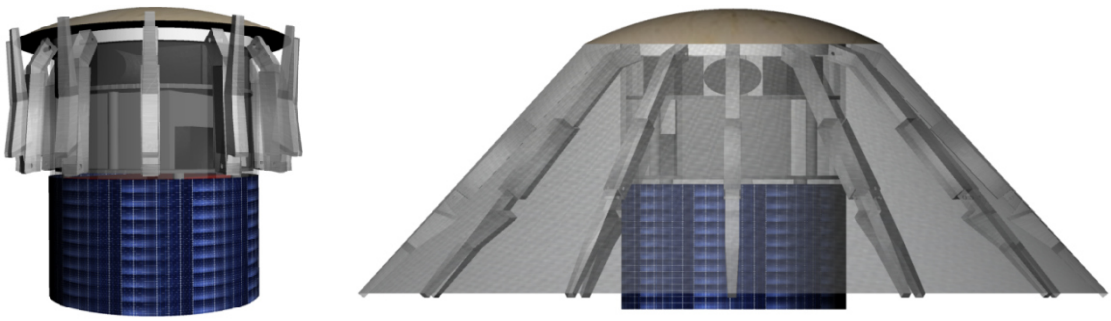

(a) (b)

Figure 3.4: Possible avio-launchable system in folded (a) and deployed (b) configurations

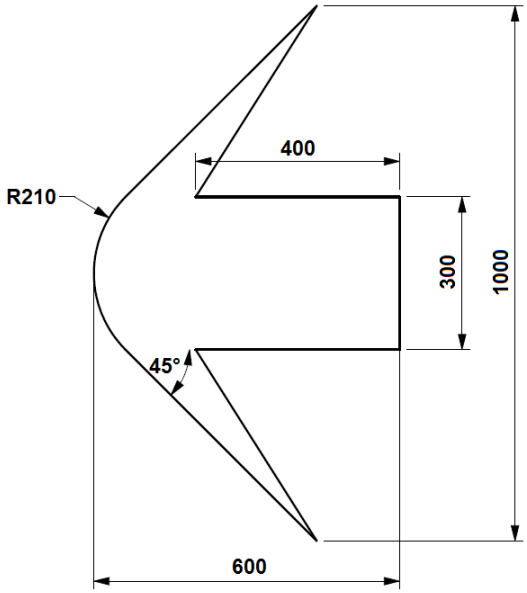

Figure 3.5: Typical dimensions (in mm) of the analyzed configuration

During the orbital phase, the deployable structure can be used to control the satellite along its orbit and during the orbital decay phase, by means of a proper modulation of the aerobrake reference surface. In this way the right approach to the defined entry interface can be achieved. Thus, the deployable aerobrake can allow the capsule to perform efficient manoeuvres in a relatively short time, with low risks and avoiding any propulsive boost.

Together with the deployable heat shield, one of the most critical aspects of the project is the air launch system. The main advantages an capability of this innovative launch procedure are reported in (12) and (14), but a detailed analysis of this phase of the mission is not included among the objectives of the present work.

3.2 De-orbit and re-entry trajectories

3.2.1 CubeSats

3.2.1.1 De-orbit trajectories

As already discussed in Section 3.1.2, after having completed the on-orbit operations, both the proposed CubeSat configurations have to perform an aerodynamic de-orbit manoeuvre taking advantage from the deployable structure. Increasing the cross section, the ballistic coefficient of the satellite decreases, so that the de-orbit time to the atmospheric entry interface is strongly reduced. Table 3.1 summarizes the parameters

characterizing the de-orbit phase of a standard CubeSat and of the CELS/CDRS configurations.

	m [kg]	S [m^2]	C_D	B [kg/m^2]
Standard CubeSat	3.6	0.01	2	180
CELS configuration	3.6	0.236	2	7.63
CDRS configuration	3.6	0.174	2	10.3

Table 3.1: De-orbit parameters for the lifetime evaluation

The drag coefficient has been assumed equal to 2 in the de-orbit trajectory leg because of the high rarefaction level, according to results obtained from a Direct Monte Carlo aerodynamic simulation (26).

In order to easily represent and understand the results, the comparison between the standard CubeSat and the CELS configuration is shown below. This can be justified noting that, according to Table 3.1, due to comparable values of the ballistic coefficients, the de-orbit results for the CELS and CDRS configurations would be very similar.

In this regard, Figure 3.6 reports the satellite lifetime as a function of the initial altitude for a standard CubeSat (a) and then for CELS in deployed configuration (b). In particular, the de-orbit lifetime has been evaluated according to the period reduction model discussed in Section 2.1.2 and considering the Minimum Solar Activity (MiSA), the Average Solar Activity (ASA) and the Maximum Solar Activity (MaSA).

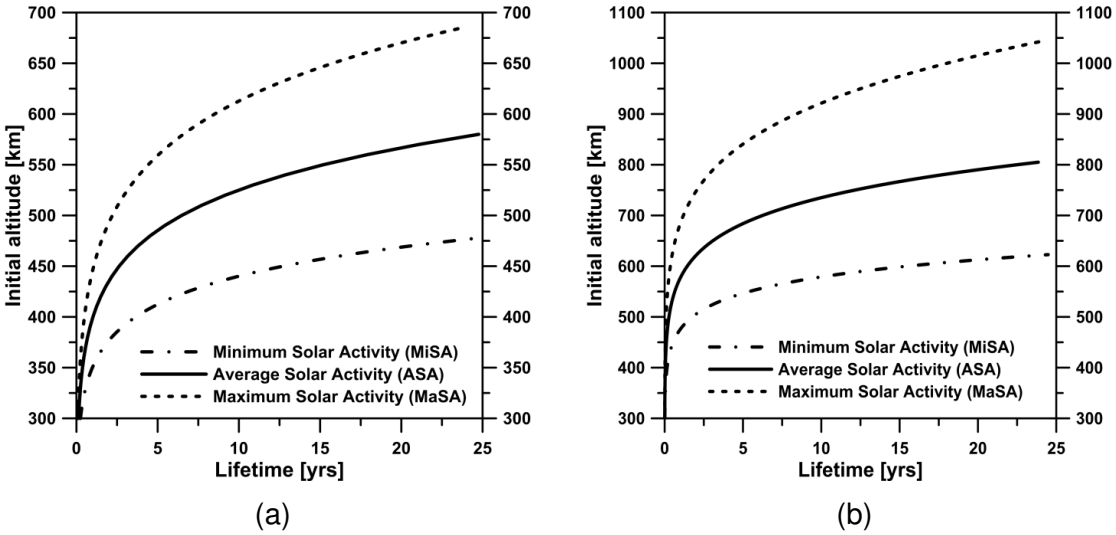

Figure 3.6: Satellite lifetime as a function of the initial altitude
for a standard CubeSat (a) and for the CELS deployed configuration (b)

The results are also summarized in Table 3.2 to better understand the achievable improvement enabled by a deployable structure in terms of lifetime requirements.

Taking into consideration the maximum lifetime requirement of 25 years, it has to be noted that, in ASA conditions, the possible initial altitude shifts from about 550 kilometres for a standard CubeSat to over 800 kilometres for CELS.

	De-Orbit Lifetime [years]					
	Standard CubeSat			Deployed CELS		
H [km]	MiSA	ASA	MaSA	MiSA	ASA	MaSA
300	0.245	0.128	0.0889	0.0107	0.00561	0.00397
400	3.65	1.02	0.489	0.155	0.0433	0.0210
500	> 25	6.47	2.21	1.76	0.275	0.0940
600	> 25	> 25	8.51	15.47	1.44	0.361
700	> 25	> 25	> 25	> 25	6.25	1.19
800	> 25	> 25	> 25	> 25	22.5	3.40

Table 3.2: De-orbit time as function of initial altitude expressed in years

Thus, the curves related to the ASA conditions in the range of altitude between 300 and 600 kilometres have been superimposed in Figure 3.7, leading to meaningful results in terms of lifetime reduction. It can be noticed that, at an altitude of 600 km the lifetime ensured by the CELS configuration in ASA condition is almost reduced by a factor of 25, permitting the rapid satellite aero-capture and destruction in atmosphere.

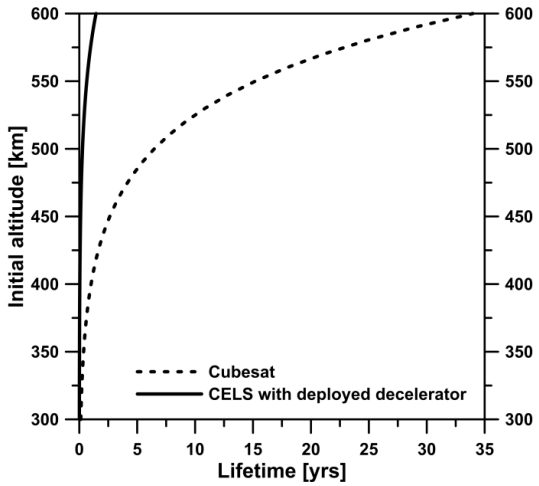

Figure 3.7: Comparison between the satellite lifetime as a function of the initial altitude for a standard CubeSat and for a CELS with the deployed decelerator; ASA conditions

3.2.1.2 Re-entry trajectories

Unlike the CELS, the CDRS has to be designed to withstand mechanical and thermal loads acting during the entire re-entry trajectory. In this regard, Table 3.3 reports the re-entry distinctive features of the CDRS.

Configuration	m [kg]	S [m^2]	C_D	B [kg/m^2]	R_c [m]
1 Re-entry module (1.3 kg) + 1 Service module (1.3 kg) + 1U-CubeSat Payload (1 kg)	3.6	0.174	1.0	20.7	0.06

Table 3.3: CDRS re-entry parameters

Assuming that the re-entry phase begins at an altitude of 120 kilometres, Figure 3.8 shows the final trajectory leg of the CDRS configuration, obtained integrating the dynamic equations of motion reported in Section 2.1.1.

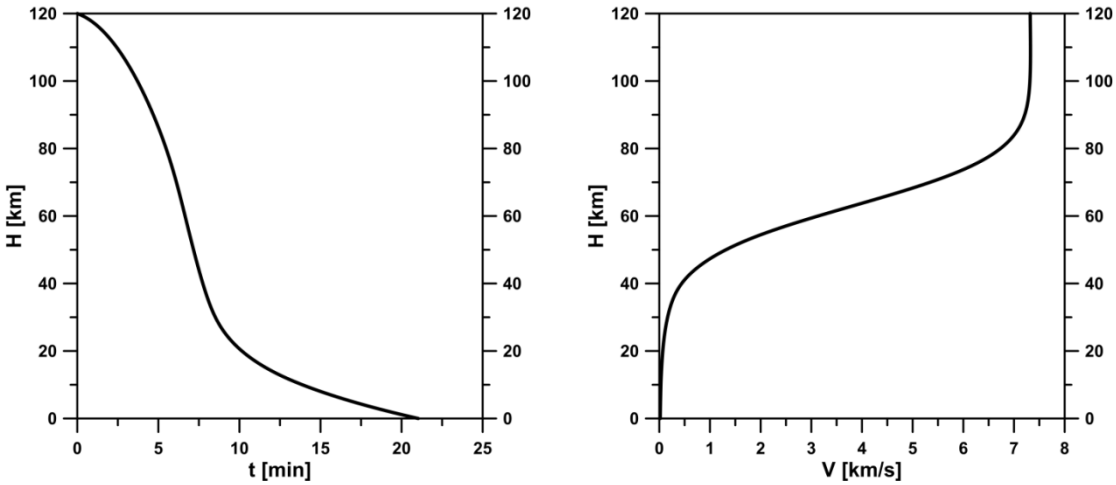

Figure 3.8: Altitude Vs time (a) and velocity (b) along the re-entry trajectory for the CDRS

In this case, an Average Solar Activity and an orbital inclination of 51.6° (i.e. the one of the International Space Station) have been considered. Furthermore, the drag coefficient in the hypersonic continuum regime has been assumed equal to 1, according to CFD simulation analyses reported in Section 3.3.1.

The discussion continues considering the aerothermal and mechanical loads experienced by the CDRS along its re-entry trajectory, in accordance with the engineering methods discussed in Section 2.1.1. Results are represented in Figure 3.9 assuming a radius of curvature of 6 centimetres and a material emissivity of 0.8.

Figure 3.9(b) shows in particular that the maximum radiation equilibrium temperature estimated for the stagnation-point region is in this case around 2000 K (i.e. around 1700°C).

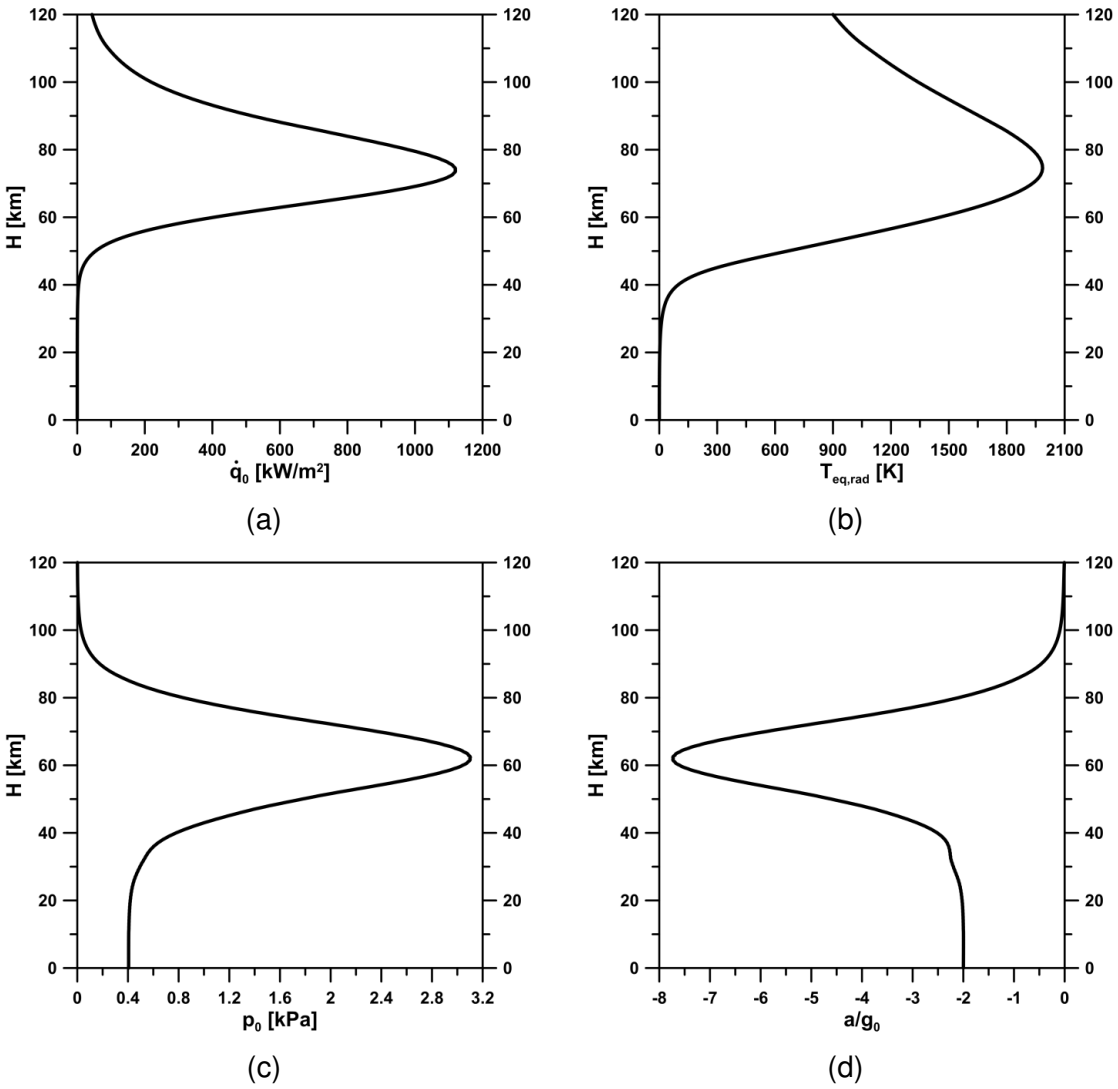

Figure 3.9: Stagnation-point heat flux (a), radiative equilibrium temperature (b), stagnation-point pressure (c) and deceleration (d) along the entire re-entry trajectory for the CDRS

3.2.1.3 Control of the target re-entry point

As mentioned in Section 3.1.2, once the umbrella-like framework is deployed, the reference surface area of the CDRS can be adjusted to control the trajectory and target the payload into a desired un-populated area for landing and recovery. In particular, the control is performed in such a way to cope with the differences between the de-orbit trajectory detected by on board instrumentation and the nominal one. Thus the capsule safely re-enters through the atmosphere and, after landing, the payload is delivered for post flight inspections and experimentations.

A simple algorithm for the CDRS control in the de-orbit phase has been therefore considered. At each time step, in particular, a surface increment or decrement has been applied to the reference surface, according to Equation 2.8.

Figure 3.10(a) shows the surface control correction necessary to cope with the nominal trajectory in presence of a solar radio flux 5% higher than the average one and for different errors in the reference density ρ_0 evaluated at 175 km of altitude. It is indeed evident that, as expressed in Equation 2.7, the above mentioned parameters strongly influence the re-entry, resulting in great dispersions of the re-entry interface point. In particular a solar radio flux 5% larger than the average leads to a ground distance error of about 3.5%.

Finally, from Figure 3.10 (b) it is possible to understand the effectiveness of the control algorithm. In a conservative approach, a solar radio flux 5% larger than the average one and a reference density 5% smaller than the nominal have been chosen. The comparison between a controlled and an uncontrolled trajectory with respect to the nominal one shows that the controlled is very close to the nominal, leading to great advantages in terms of mission reliability.

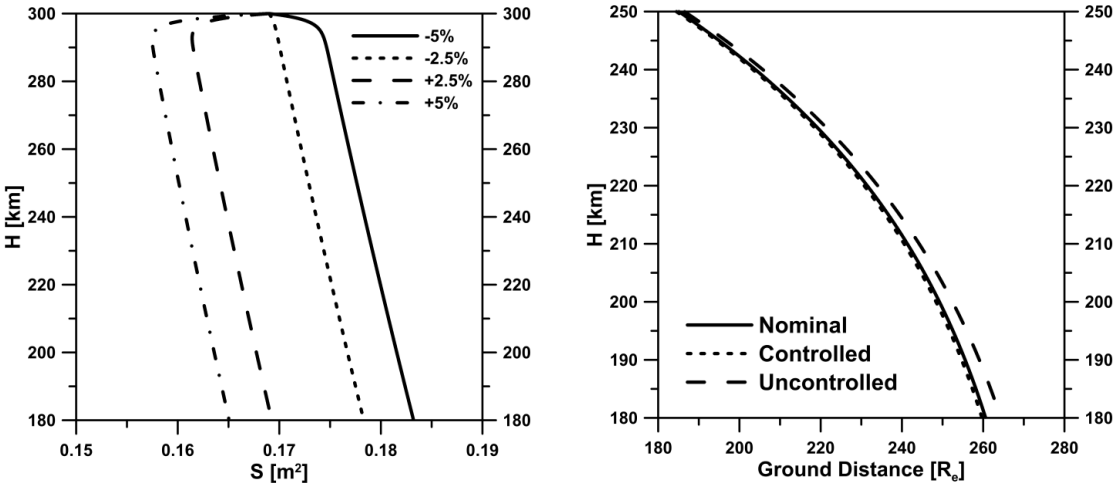

Figure 3.10: Surface control to contrast a solar radio flux 5% larger than the nominal and different values of the reference density (a); Comparison between controlled and uncontrolled trajectory, assuming a solar radio flux 5% larger than the nominal and a reference density 5% smaller than the nominal one (b)

3.2.2 Avio-launched system

3.2.2.1 De-orbit and re-entry trajectories

In this Section possible de-orbit and re-entry trajectories of an avio-launched system for Earth observation will be analyzed. In particular, the attention will be focused on a capsule characterized by the entry parameters and initial conditions reported in Table 3.4. In Table 3.4 the initial velocity has been assumed equal to the relative orbital

velocity at the initial altitude of 300 km (i.e. taking into account Earth's rotation). An orbit inclination of 45° has also been assumed.

m [kg]	S [m^2]	R_c [m]	H [km]	V [km/s]	γ [°]
15.0	0.785	0.210	300	7.44	0

Table 3.4: Entry parameters and initial conditions for the avio-launched system

In this case a variable drag coefficient has been assumed along the trajectory, so to take into account also the effect of air rarefaction on that aerodynamic coefficient. A bridging relation between the continuum (c) and the free molecular flow (f) regimes for the drag coefficient has been assumed and reported in Equation 3.1 (43). This relation is a function of the Knudsen number *Kn*, defined as the ratio between the mean free path and a characteristic dimension of the capsule (in this case the reference diameter). The mean free path is assumed to vary with respect to the altitude according to the standard atmosphere model.

$$C_D = C_{D,c} + \left(C_{D,f} - C_{D,c}\right)\frac{Kn}{Kn + 0.1} \qquad 3.1$$

Also in this case the drag coefficient in free molecular and continuum regimes have been assumed equal to 2 and 1, respectively.

With these assumptions the nominal re-entry trajectory has been calculated numerically integrating the dynamic equations of motions shown in Section 2.1.1.

Figure 3.11 reports the orbital decay of the capsule with the deployed heat shield for ASA conditions above 120 km altitude. It is worth noticing that this phase is performed in less than 3 days, while according to Table 2.2 typical lifetimes for a capsule with a folded heat shield and a similar mass are in the order of a few months.

On the one hand this can be useful to have a sufficient time to perform the orbital mission before deploying the aerobrake and, on the other hand, when the orbital phase of the mission is concluded, a relatively rapid decay can be obtained.

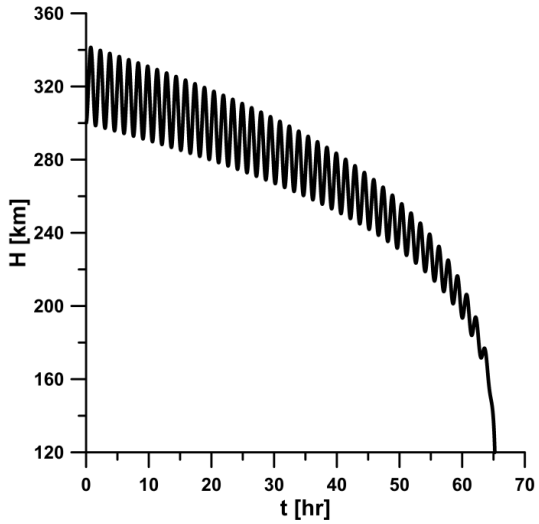

Figure 3.11: Orbital decay from 300 km altitude

Finally, Figure 3.12 reports the most significant re-entry parameters below 120 km altitude. In this case a maximum stagnation point heat flux around 500 kW/m^2 is experienced around 75 km altitude. This leads to a maximum radiation equilibrium temperature on the nosecone of about 1500°C assuming a surface emissivity of 0.8.

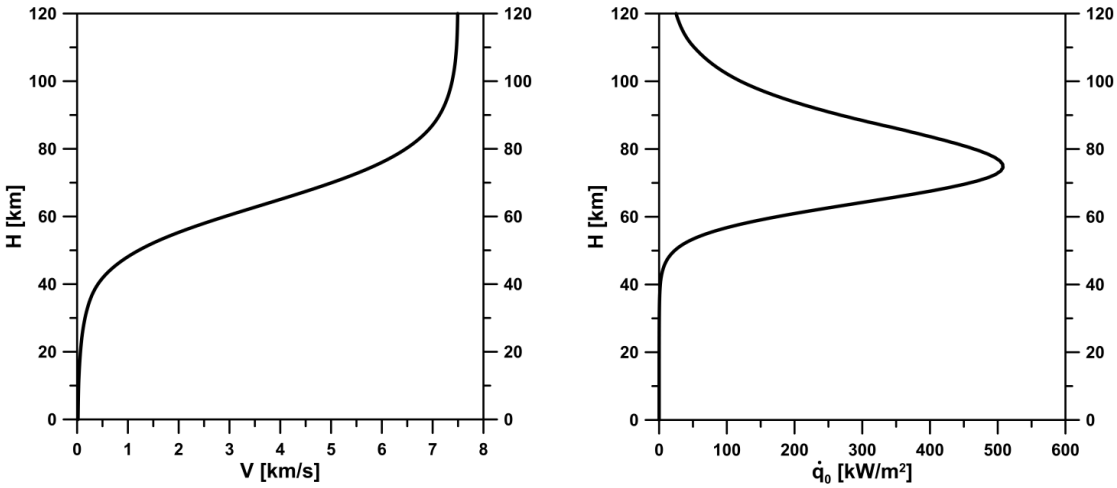

(a) (b)

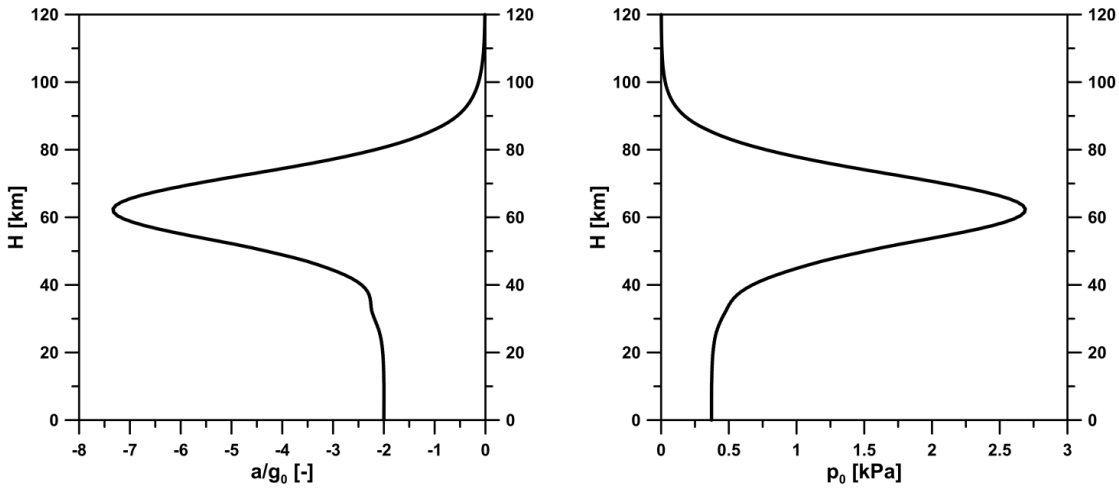

Figure 3.12: Velocity (a), stagnation-point heat flux (b), acceleration (c) and stagnation-point pressure (d) variation along the re-entry trajectory below 120 km for the avio-launched capsule

3.2.2.2 Landing dispersion analysis

In this Section a statistical analysis based on the Monte Carlo method will be carried out in order to assess the dispersion of the nominal trajectory reported in Section 3.2.2.1. As also discussed in Section 2.1.3, the first step of the analysis foresees the identification of a number of uncertainties for some flight variables, which have been reported in Table 3.7, Table 3.5 and Table 3.6, divided in three categories. As far as the atmospheric conditions are concerned, the average density at each altitude has been assumed to be equal to the density prescribed by the standard atmosphere and a 3-σ variance equal to the 10% of the average value has been assumed.

Variable	Average Value	3-σ Variance
Initial altitude [km]	120	0.500
Initial velocity [m/s]	7492	10.00
Initial flight path angle [°]	-0.2477	0.01

Table 3.5: Mission uncertainties connected with the entry interface

Variable	Average Value	3-σ Variance
Capsule mass [kg]	15	0.10
Drag coefficient [-]	Equation 3.1	0.10
Lift coefficient [-]	0	0.010
Reference Surface [m^2]	0.79	0.010

Table 3.6: Mission uncertainties connected with the capsule configuration

Variable	Average Value	3-σ Variance
Air density [kg/m^3]	Standard atmosphere	10%
Wind velocity [m/s]	0	10

Table 3.7: Mission uncertainties connected with the atmospheric conditions

Then, random Gaussian distributions are independently generated for all the input parameters reported in Table 3.7, Table 3.5 and Table 3.6, on the basis of the assigned average values and 3-σ standard deviations. All the distributions consist in 1000 pseudo-experiments and some of them are reported in Figure 3.13 through Figure 3.15. In particular, in Figure 3.15 the random atmospheric density and wind velocity have been plotted at 20 km altitude for example.

Finally, 1000 re-entry trajectories (one for each i^{th} pseudo-experiment) have been integrated assuming the simultaneous effect of all the random parameters at the i^{th} step.

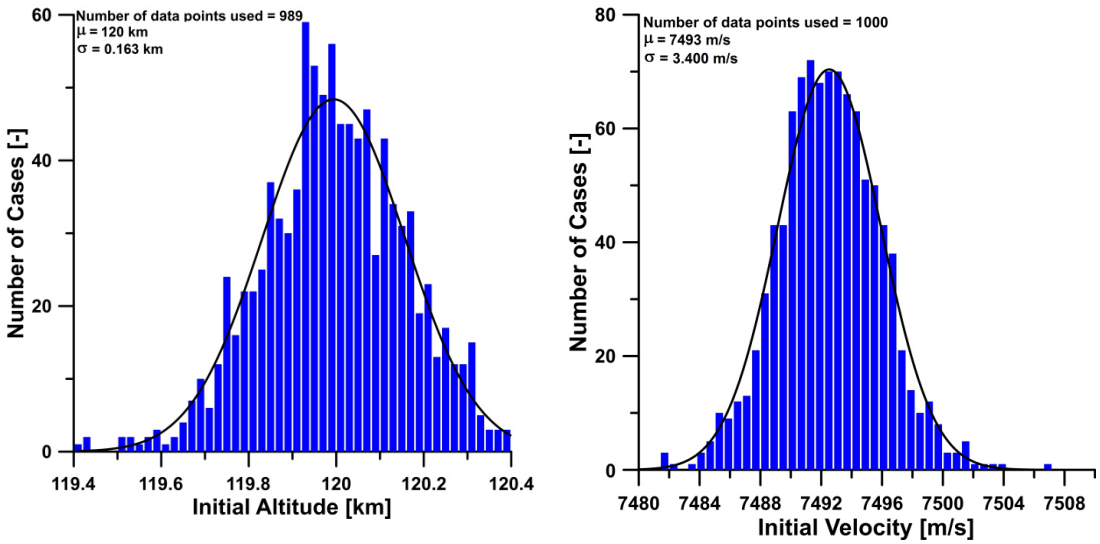

(a) (b)

Figure 3.13: Random Gaussian distributions for the mission uncertainties connected with the entry interface

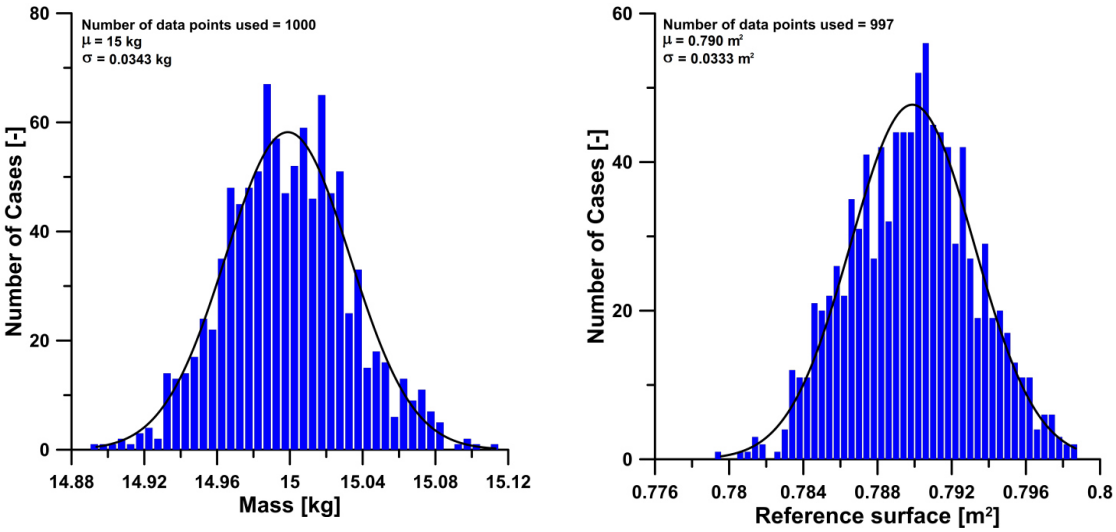

(a) (b)

Figure 3.14: Random Gaussian distributions for the mission uncertainties connected with the capsule configuration

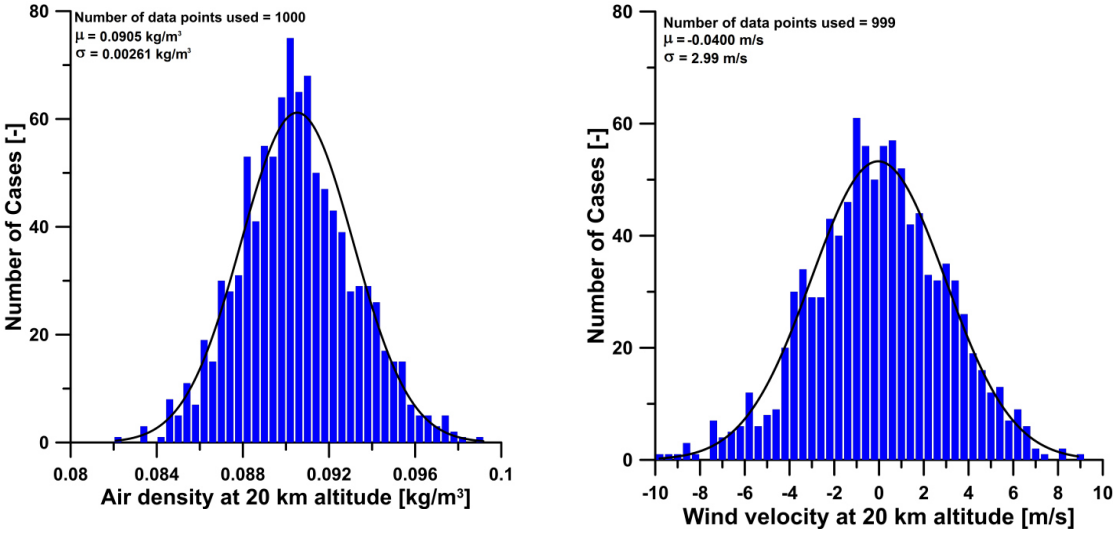

(a) (b)

Figure 3.15: Random Gaussian distributions for the mission uncertainties connected with the atmospheric conditions

The occurrences of some significant parameters characterizing the 1000 integrated re-entry trajectories (i.e. the maximum deceleration, the impact velocity, the stagnation-point pressure and heat flux) have been plotted in Figure 3.16. It is evident that also these distributions tend to Gaussian curves (increasing the number of pseudo-experiments, in particular, the Gaussian trend would be more and more evident) and that the average values are very close to the corresponding nominal values along the nominal trajectory.

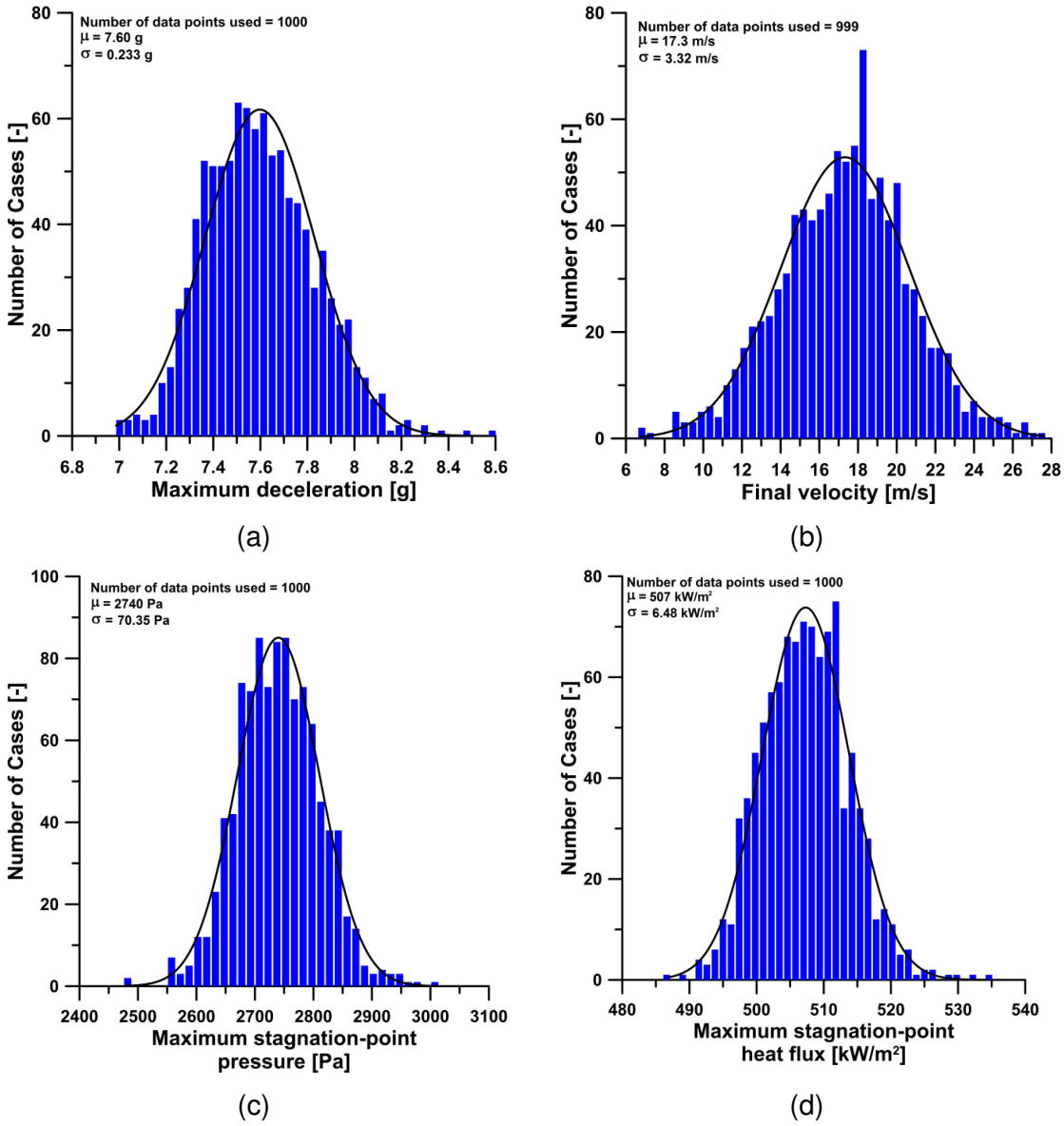

Figure 3.16: Statistical distribution of the maximum deceleration (a), the terminal velocity (b), the maximum stagnation-point pressure (c) and the maximum stagnation-point heat flux (d)

Finally, the landing dispersion has been evaluated in terms of downrange dispersion and landing point location and plotted in Figure 3.17. It is evident that in this case the classical landing ellipse is very tight because no disturbances in the crossrange direction have been considered for the capsule.

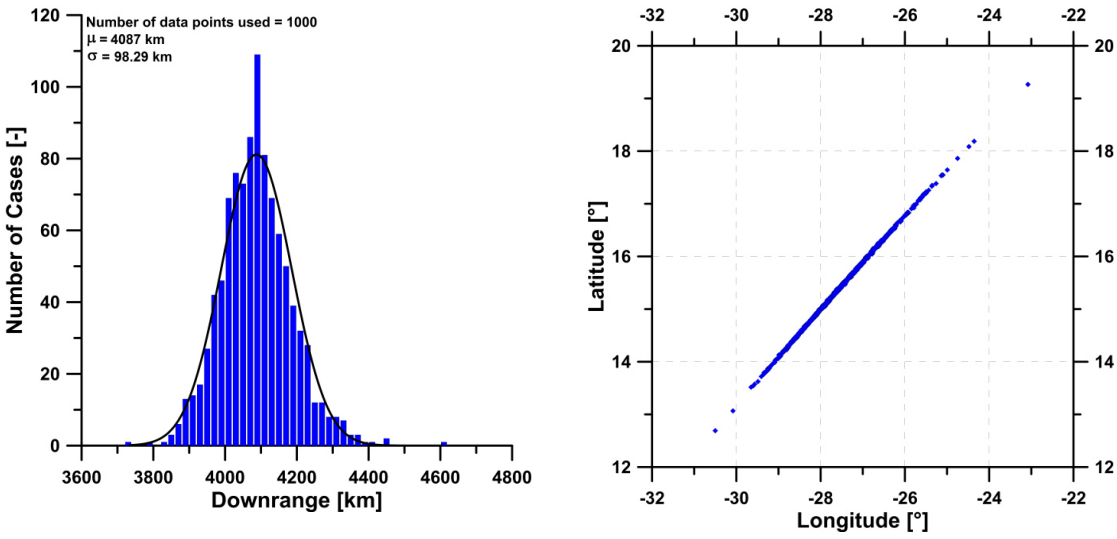

Figure 3.17: Landing dispersion in terms of downrange and landing point location

3.3 Aerothermodynamic analyses

3.3.1 CubeSats

CFD simulations have been carried out for the flow field around the CDRS configuration, on the basis of the numerical models reported in Section 2.22.2 for a reacting gas mixture.

Figure 3.18 shows the pressure (a) and temperature (b) profiles along the stagnation line. The free stream conditions, according to Figure 3.9(a), correspond to the maximum heat flux experienced along the re-entry trajectory and are reported in Table 3.8.

H [km]	p_∞ [Pa]	T_∞ [K]	M_∞	$V_\infty^2/2$ [MJ/kg]
73.7	2.93	211	20.6	18.0

Table 3.8: Free stream conditions for CFD simulations

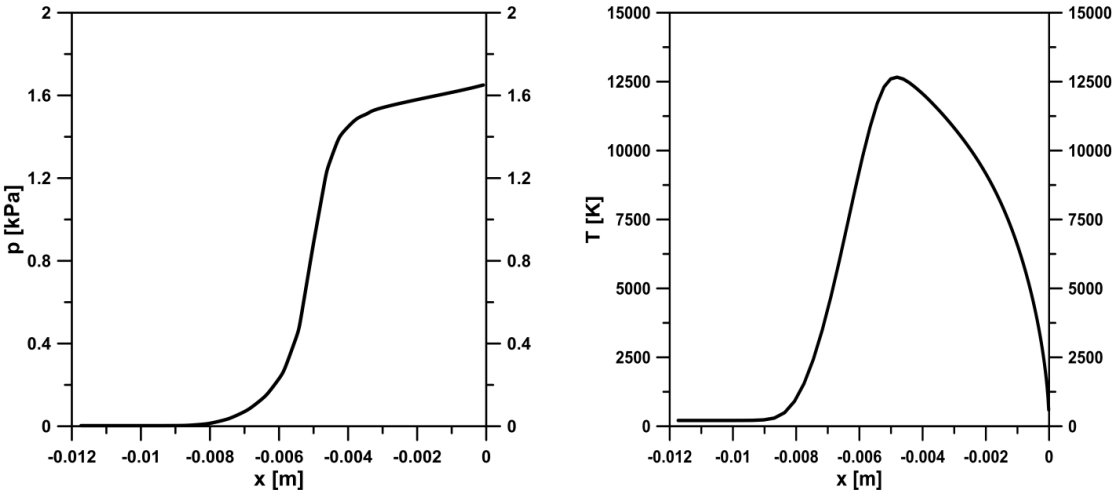

Figure 3.18: CDRS pressure (a) and temperature (b) variations along the stagnation line for the maximum heat flux condition along the re-entry trajectory

Figure 3.19 shows the corresponding pressure and heat flux distributions along the CDRS wall surface. The convective heat flux has been estimated in particular in NC and FC conditions.

Looking at Figure 3.9(a), it can be observed that the maximum value of the stagnation-point heat flux, slightly larger than 1100 kW/m^2, is very close to the NC solution obtained through the CFD analysis and reported in Figure 3.19(b). In addition, the maximum convective heat flux acting on the flexible part of the heat shield is roughly one half of the one acting on the stagnation-point. Finally, the stagnation pressure reported in Figure 3.19(a) is in great accordance with the one predicted along the re-entry trajectory at an altitude around 74 km and shown in Figure 3.9(c).

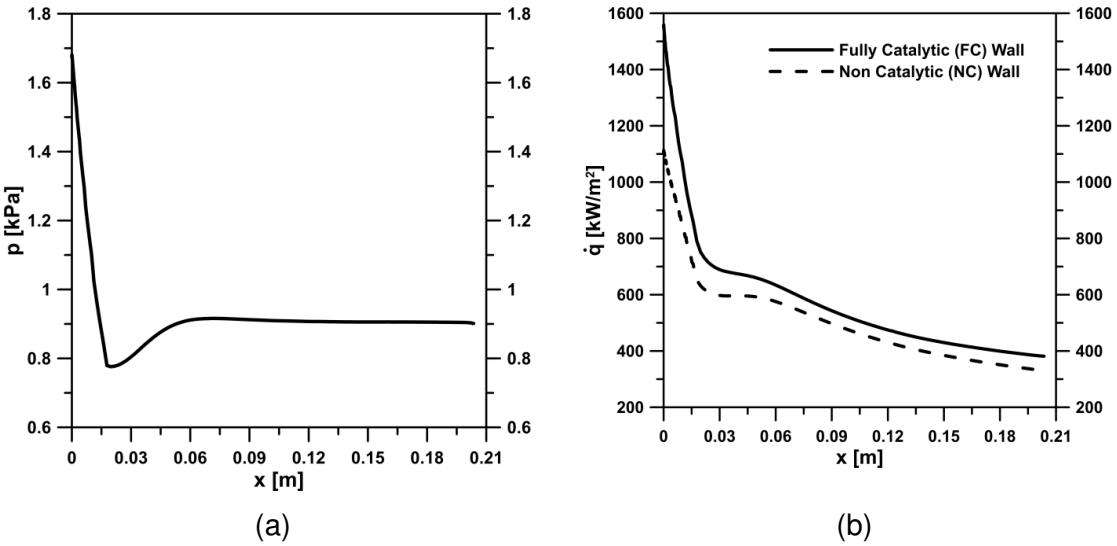

Figure 3.19: Pressure (a) and heat flux (b) profiles along the CDRS wall; evaluated at the condition of maximum heat flux experienced along the re-entry trajectory

3.3.2 Avio-launched system

3.3.2.1 Aerodynamic stability

In this Section several aerodynamic analyses have been performed to assess, in particular, the aerodynamic stability of the system for different positions of the Centre of Gravity (CoG), both in continuum and rarefied regimes. The latter class of calculations has been performed by means of the Direct Simulation Monte Carlo, whose results have been widely reported in (26).

In the latter reference more information on the computational method can be also found. In this work it is only worth reminding that the DSMC method (44), (45) is currently the only possible tool for the solution of rarefied flow fields from free molecular to continuum low density regimes. DSMC considers the gas as made up of discrete molecules. It is based on the kinetic theory of gases and computes the evolution of millions of simulated molecules, each one representing a large number (say 10^{15}) of real molecules in the physical space. Intermolecular and molecule-surface collisions are also taken into account. The computational domain is divided in cells, used for selecting the colliding molecules and for sampling the macroscopic fluid-dynamic quantities.

In order to evaluate the drag coefficient, the ballistic parameter and the stability characteristics of the deployable capsules at high altitudes (i.e. at 100 and 150 km), a number of computations has been carried out using a 3D numerical code based on the DSMC method. Three intermediate steps of the TPS deployment sequence have been also taken into account at 150 km, while at 100 km altitude the TPS has been considered completely deployed. At these altitudes the overall Knudsen number ($Kn_{D\infty}$) ranges from 0.11 to 42. According to Moss (46), a general definition of the transitional regime considers the overall Knudsen number between 10^{-3} and 50. The capsule is therefore in highly rarefied regimes, very close to the free molecular flow regime. Table 3.9 reports free stream inputs parameters for DSMC computations at the altitudes under investigation (being N_∞ the free stream number density).

H [km]	ρ_∞ [kg/m^3]	N_∞ [m^{-3}]	T_∞ [K]	p_∞ [Pa]	V_∞ [m/s]	M_∞ [-]	$Kn_{D\infty}$ [-]
150	2.08×10^{-9}	5.20×10^{16}	634	4.50×10^{-4}	7600	13.4	42.0
100	5.59×10^{-7}	1.19×10^{19}	196	3.20×10^{-2}	7500	26.3	0.11

Table 3.9: Input parameters for DSMC computations

The intermediate configurations of the deployment sequence have been analyzed according to Figure 3.20, being *φ* the half-cone angle at each deployment step.

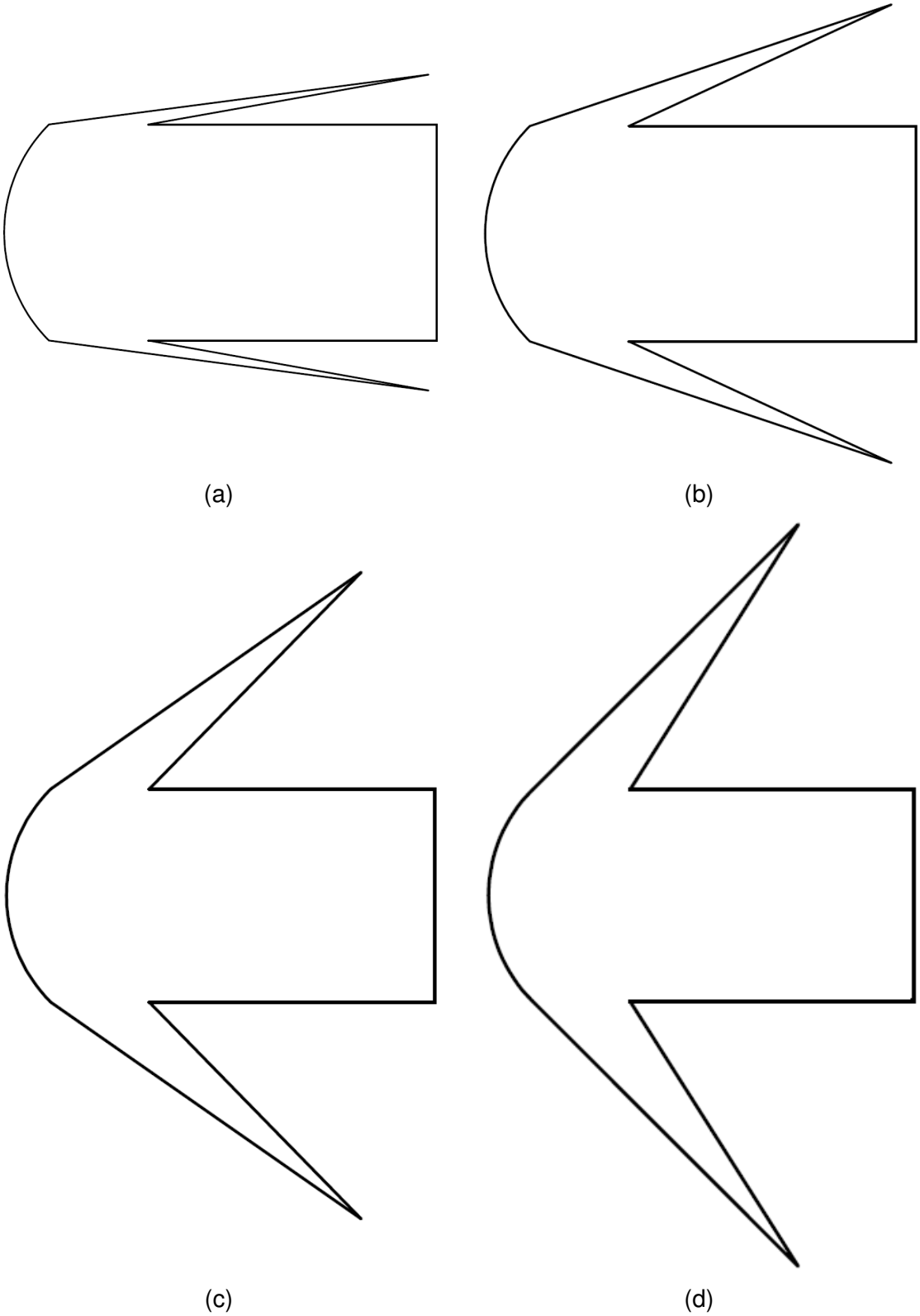

Figure 3.20: Sketch of the deployment process: (a) Step 1, φ=7.50° (b) Step 2, φ=18.5° (c) Step 3, φ=35.0°, Step 4, φ=45.0° (d)

Figure 3.21 and Table 3.10 report the ballistic parameter variation during the deployment phase, starting from the folded configuration (Step 0) up to the completely deployed TPS (Step 4). It is evident that the ballistic coefficient is reduced of about one order of magnitude passing from the folded to the completely deployed configurations. The variation of this parameter provides the measure of the capability to aerodynamically control the capsule during the de-orbit phase.

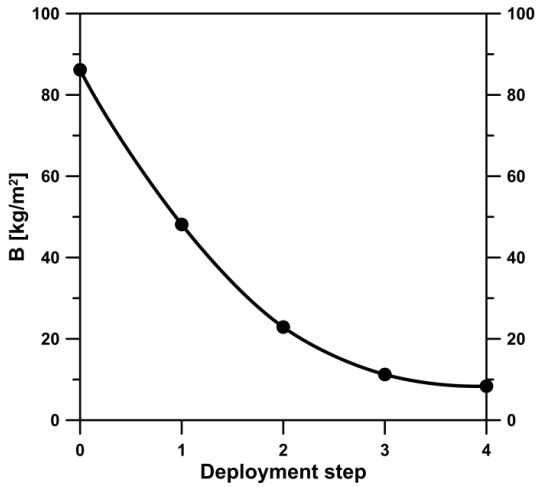

Figure 3.21: Ballistic parameter variation as a function of the deploying step (150 km altitude)

	Step 0	Step 1	Step 2	Step 3	Step 4
C_D [-]	2.46	2.06	2.05	2.04	1.96
S [m^2]	0.0707	0.151	0.320	0.655	0.915
B [kg/m^2]	86.2	48.1	22.9	11.3	8.38

Table 3.10: Drag coefficient, reference surface and ballistic parameter for the different deployment steps (150 km altitude)

As far as the longitudinal stability is concerned, the angle of attack has been ranged from 0° to 10° for the computation of the stability derivatives ($dCM_z/d\alpha$) relative to the Nominal Equilibrium Condition (NEC), around the zero angle of attack and from 170° to 180° for the stability evaluation in the Reverse Equilibrium Condition (REC), around the angle of attack of 180°. Due to the almost linear behaviour in these ranges, in both cases the stability derivative has been numerically approximated by the finite difference in the interval $\Delta\alpha=10°$.

The reference system has been assumed in accordance with Figure 3.22, being the z-axis such as to form a right-handed triad with the x and y.

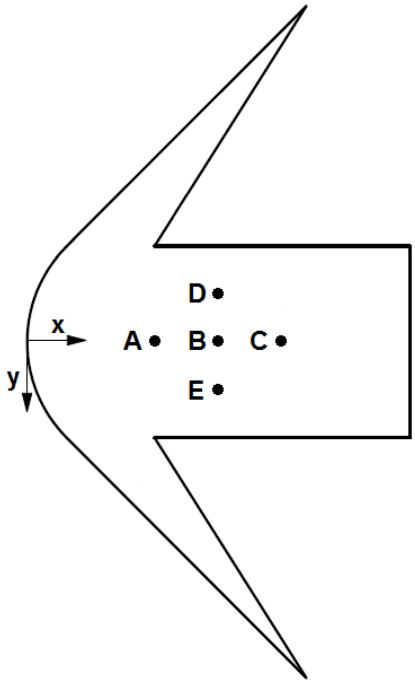

Figure 3.22: Capsule reference system and analyzed CoG locations

As well known, in this case, a negative value of the stability derivative identifies a stable condition (the more negative the derivative, the more stable the system), considering that a negative moment coefficient represents a pitching moment. The analysis has been carried out considering as poles the five different positions for the Centre of Gravity (CoG) shown in Figure 3.22 and as reference length the longitudinal dimension of the capsule (i.e. 60 cm). At each deployment step, the reference surfaces reported in Table 3.10 have been also considered.

Figure 3.23(a) shows the stability derivative ($dC_{Mz}/d\alpha$) profiles at 150 km altitude as a function of the deployment step with respect to the equilibrium condition around zero angle of attack and for the centre of gravity locations shown in Figure 3.22. Figure 3.23(b) refers to the REC. These figures clearly show that the analyzed configuration is longitudinally stable during the entire deployment process with respect to the NEC for almost all the CoG location analyzed. At the same time, an opposite behaviour can be verified with respect to the REC, as reported in Figure 3.23(b). This situation is very favourable because implies the aerodynamic self stabilization of the capsule. As expected, at each deployment step, as the centre of gravity moves forward, the stability derivative decreases.

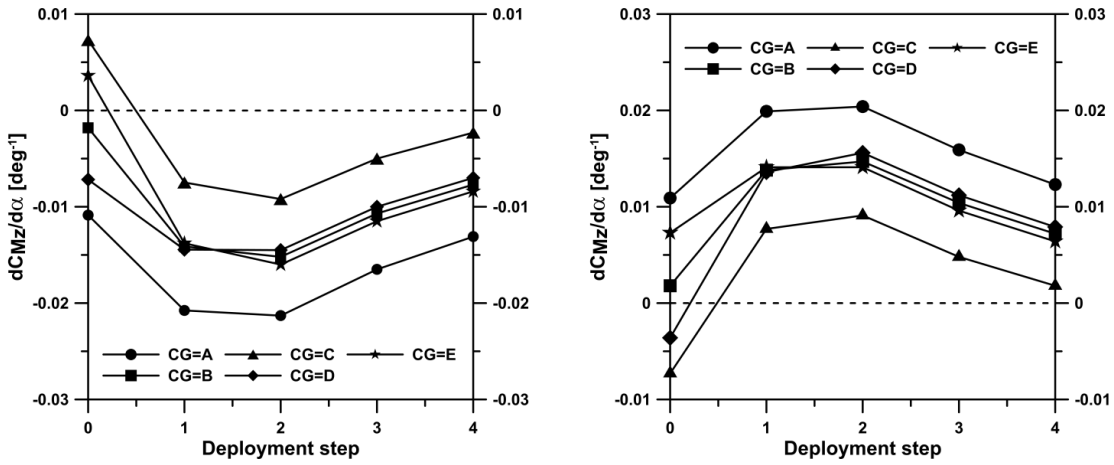

Figure 3.23: Stability derivative profiles as a function of the deployment step for different CoG positions at 150 km altitude, with respect to the nominal (a) and the reverse (b) equilibrium attitude

Table 3.11 reports the stability derivatives at 100 km altitude and for the above mentioned centre of gravity locations. Also in this case the analyzed configuration shows a good stability with respect to the NEC around zero angle of attack. In addition, in this case the capsule is also stable with respect the REC for almost all the analyzed CoG locations, but the module of the stability derivative is one order of magnitude lower than in the previous case. It is therefore clear that the effect of the Reynolds number increment (from 0.628 to 277) and of the Knudsen number reduction (from 42 to 0.11) is generally to increase the atmospheric stabilization. If no active stabilization techniques are foreseen, the aerobraking deployment has to be therefore carried out at an appropriate altitude, so to take advantage of the unique stable equilibrium condition at relatively high altitudes.

$dC_{Mz}/d\alpha$ [deg^{-1}]	CG≡A	CG≡B	CG≡C	CG≡D	CG≡E
NEC	$-1.1\cdot10^{-2}$	$-7.0\cdot10^{-3}$	$-3.0\cdot10^{-3}$	$-6.4\cdot10^{-3}$	$-7.6\cdot10^{-3}$
REC	$9.2\cdot10^{-4}$	$-5.0\cdot10^{-4}$	$-2.0\cdot10^{-3}$	$-1.8\cdot10^{-3}$	$-1.0\cdot10^{-3}$

Table 3.11: Stability derivatives [1/deg] with respect to the Nominal Equilibrium Condition (NEC) and Reverse Equilibrium Condition (REC) at 100 km altitude

Finally, Table 3.12 reports aerodynamic stability analyses performed by means of 3D CFD calculations at 50 km altitude. Results confirm the capsule behaviour verified at 100 km altitude also in continuum regime ($Kn_{D\infty}\approx8\cdot10^{-5}$).

$dC_{Mz}/d\alpha$ [deg^{-1}]	CG≡A	CG≡B	CG≡C	CG≡D	CG≡E
NEC	$-4.5\cdot10^{-3}$	$-3.3\cdot10^{-3}$	$-2.1\cdot10^{-3}$	$-1.0\cdot10^{-2}$	$3.7\cdot10^{-3}$
REC	$-1.9\cdot10^{-3}$	$-1.8\cdot10^{-3}$	$-1.7\cdot10^{-3}$	$-1.2\cdot10^{-2}$	$8.5\cdot10^{-3}$

Table 3.12: Stability derivatives [1/deg] with respect to the Nominal Equilibrium Condition (NEC) and Reverse Equilibrium Condition (REC) at 50 km altitude

3.3.2.2 Aerothermodynamic loads evaluation

In this Section a comparative aerothermodynamic study between CFD and DSMC methods has been performed. Also in this case CFD simulations have been carried out on the basis of the numerical models reported in Section 2.22.2 for a reacting gas mixture. Then, both CFD and DSMC analyses considered fully-catalytic wall conditions, assuming a constant wall temperature of 300 K.

Figure 3.24 reports the comparison between CFD and DSMC calculations regarding the most significant thermal and mechanical loads acting on the surfaces of the analyzed capsules.

In particular, Figure 3.24(a) shows that the convective heat flux distribution on the capsule surface in Fully Catalytic conditions and for the maximum stagnation-point heat flux corresponding to the engineering profile plotted in Figure 3.12(b). On the other hand in Figure 3.24(b) the pressure distribution on the thermal protection system is evaluated for the maximum stagnation-point pressure conditions identified in profile shown in Figure 3.12(d). A very good accordance can be found both between the CFD and DSMC methods.

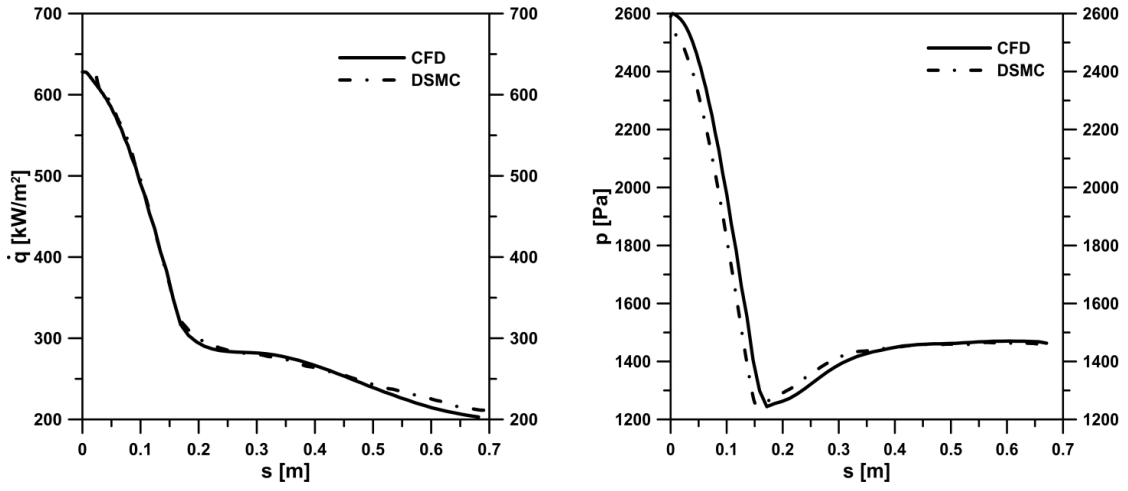

Figure 3.24: Convective heat flux profiles along the capsule surface for FC wall at the maximum $\dot{q}_0$ condition (a); pressure profiles along the capsule surface at the maximum p_0 condition (b)

It is clear that, as also discussed in Section 2.2.2, the convective heat flux evaluated in FC conditions is generally an overestimation, considering the intermediate wall catalycity of the material. If one consider, in particular, materials characterized by very low catalycity, like the RESCOR, the real heat flux is much closer to the NC solution, which is compared to the FC one in Figure 3.25. The NC provides therefore in our case both a more realistic and a more affordable load condition for the class of materials under consideration.

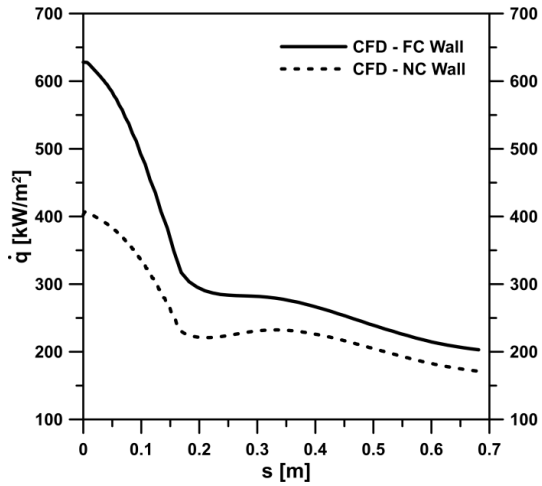

Figure 3.25: Comparison between FC and NC convective heat fluxes at the maximum $\dot{q}_0$ condition

In Figure 3.26 the contour distributions for some significant flowfield variable have been reported in the maximum stagnation-point heat flux condition. From Figure 3.26 it can be noticed that DSMC calculations overestimate the stand-off distance and the shock wave thickness with respect to CFD, resulting in a smoother variation of the flowfield variables along the stagnation line.

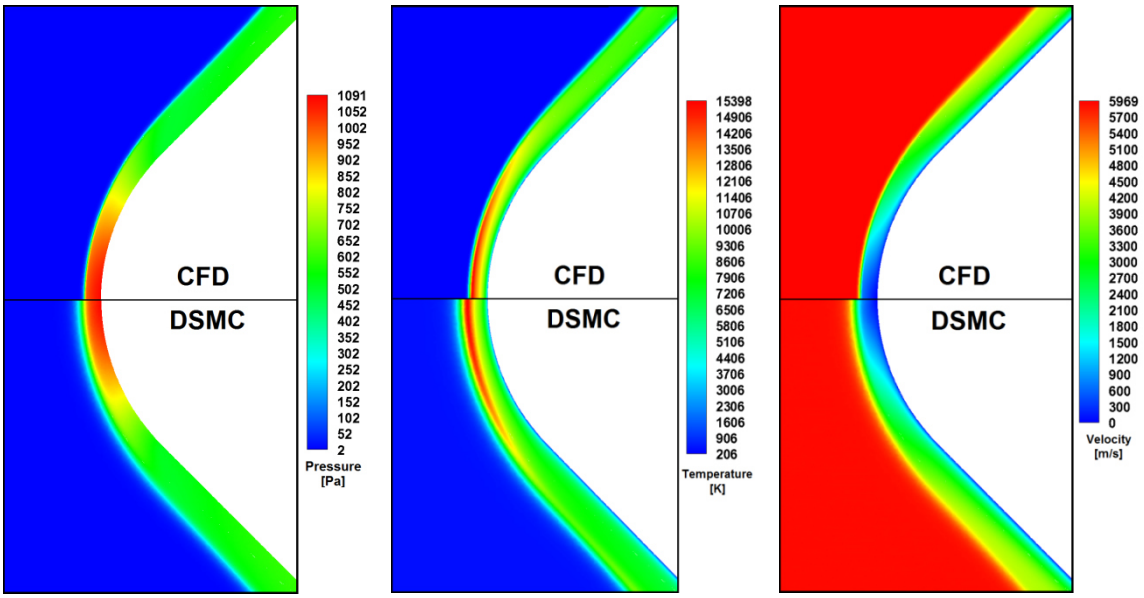

(a) (b) (c)

Figure 3.26: Pressure (a), Temperature (b) and Velocity (c) distributions in the flow field past the capsule configuration at the maximum stagnation-point heat flux condition

4 Suborbital entry trajectories onboard sounding rockets

4.1 System configurations and mission profiles

In the present Section technology demonstrators to be launched onboard the MAXUS and REXUS sounding rockets will be described in terms of system configuration and mission profile.

From an aerodynamic point of view, both the capsules present the same basic axisymmetric sphere-cone configuration, mainly consisting of a combination of a rigid hemispherical nose-cap and a conical flexible high temperature resistant fabric. A cylindrical compartment provides the accommodation for the payload and all the subsystems necessary for the mission (including batteries, actuators, sensors, data handling system and antenna beacon).

Different mass and dimensions have been considered for the two analyzed scenarios due to the different available volumetric envelopes offered by the two sounding rockets. The MAXUS mission profile, as it will be more clear in the following, also requires a more resistant (and therefore more massive) structure to withstand the larger dynamic and thermal loads experienced along the re-entry path. The main geometric parameters of the analyzed configurations are reported in Table 4.1.

	MAXUS	REXUS
Mass [kg]	15	5.0
Reference surface [m^2]	0.79	0.64
Ballistic parameter [kg/m^2]	19/14	7.8
Reference diameter [m]	1.0	0.90
Radius of curvature [cm]	17/27	12

Table 4.1: Characteristic parameters for the analyzed configuration

In addition, for the technology demonstrator to be launched onboard the MAXUS rocket, two aerodynamic configurations, characterized by two different half-cone angles (i.e. 45° and 60°), have been considered. The analyzed configurations are supposed to have the same mass and reference surface, but different ballistic parameters (due to the different drag coefficient, as it will be clarified in the following) and radius of curvature, as also reported in the second column of Table 4.1.

As far as the deployment mechanism is concerned, for all the analyzed configurations, a proper number of telescopic rods, hinged to the main body of the capsule and a sliding structure are employed to rotate and tighten the flexible fabric, so to realize the

desired half-cone angle. Other structural constraints are provided by metallic threads anchored to the sliding structure and the main body of the capsule. The entire deployment sequence is supposed to be electronically controlled.

4.1.1 Technology demonstrator for MAXUS sounding rocket

The first suborbital mission scenario analyzed foresees the ejection of the deployable re-entry demonstrator from the MAXUS interstage at about 150 km altitude, during the exoatmospheric ascent phase, a parabolic trajectory up to an apogee around 720 km and, finally, an atmospheric re-entry phase starting from an altitude of 100 km, as also schematically depicted in Figure 4.1.

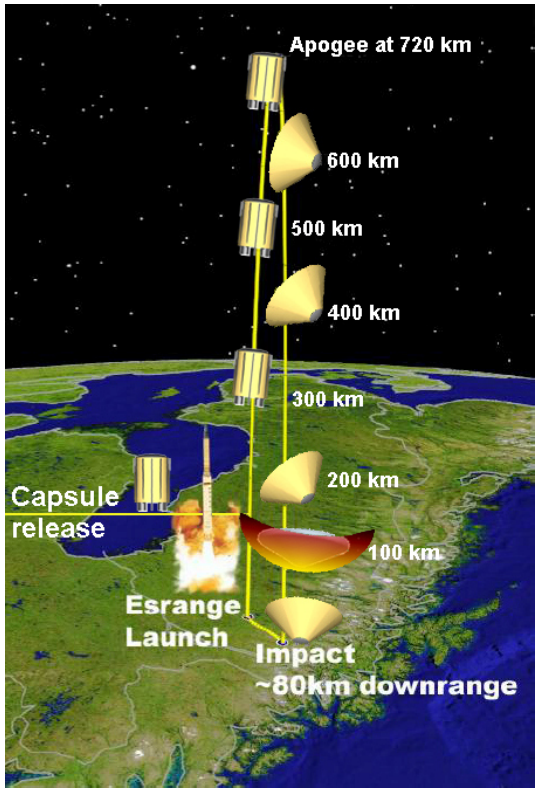

Figure 4.1: Suborbital mission scenario from MAXUS sounding rocket

For the flight events occurring below 100 km altitude, the main flight phases are in particular illustrated in Figure 4.2. After rocket burnout and coast, the MAXUS payload will be separated by the engine at 100 km altitude, 86 s after lift-off. Only during the exoatmospheric ascent phase the capsule will be ejected from the payload interstage at about 150 km altitude, continuing its ascent phase up to an apogee of about 720 km. The altitude and flight parameters (in particular velocity and flight path angle) at the time of the capsule ejection from the MAXUS payload shall be clearly identified in

agreement with the mission managers and eventual dispersion shall be also provided for a correct mission analysis. In this work preliminary values reported in Table 4.2 have been assumed in agreement with the SHARK mission (28).

Altitude [km]	Velocity [km/s]	Flight path angle [°]
150	3.20	87.0

Table 4.2: Preliminary flight parameter at the time of the capsule ejection from MAXUS

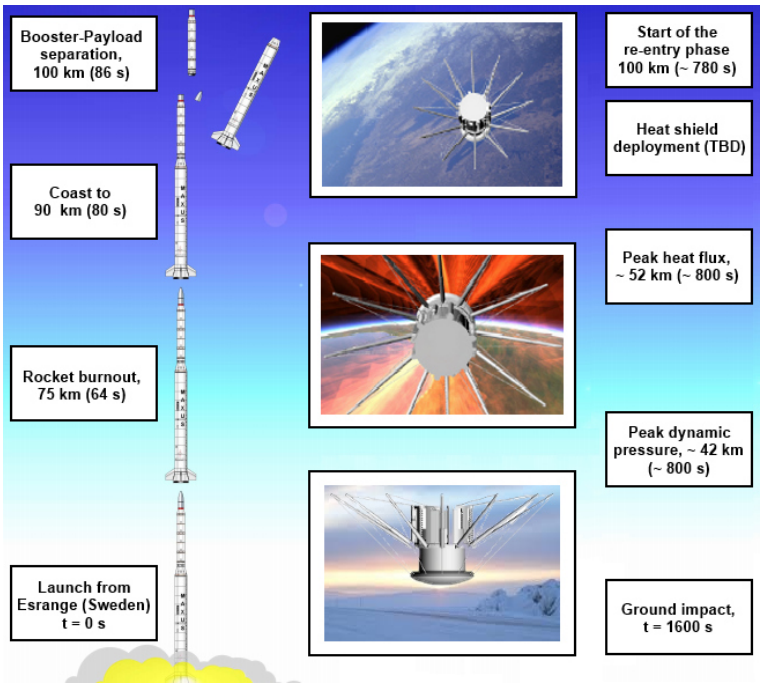

Figure 4.2: Mission scenario below 100 km altitude

The experimental procedure shall be automatically controlled using a time controller of the onboard computer. Two different scenarios may be foreseen for the heat shield deployment:

- the deployment sequence begins and is completed in the exoatmospheric flight, i.e. before atmospheric re-entry;
- the aerobrake is only partially deployed in the exoatmospheric phase, assuming a partial half-cone angle in the order of 20°, but complete deployment and tensioning is carried out during the descent trajectory between 90 km and 70 km.

The latter solution can be useful to exploit the unique aerodynamically stable attitude of the folded configuration, as it will be pointed out in the following. A back-up activation system for the aerobrake deployment, based on pressure and/or acceleration

measurements along the nominal re-entry trajectory, shall be also considered in case of temporal mismatch between nominal and real trajectory.

The flight test should demonstrate the correct deployment procedure of the capsule heat shield, the aerodynamic deceleration and re-entry and the payload survivability. In addition, the most important flight data should be recorded and recovered for post-flight analyses to assess the thermal and aerodynamic performances of the deployable re-entry capsule. The collected flight data can be also useful for trajectory reconstruction and comparison with the analysis and design techniques used in the development of the re-entry system.

Considering the cylindrical volume available in the MAXUS interstage, having a diameter of 29 cm and a height of 25 cm and shown in Figure 4.3, different aerodynamic and structural configurations have been investigated for the demonstrator.

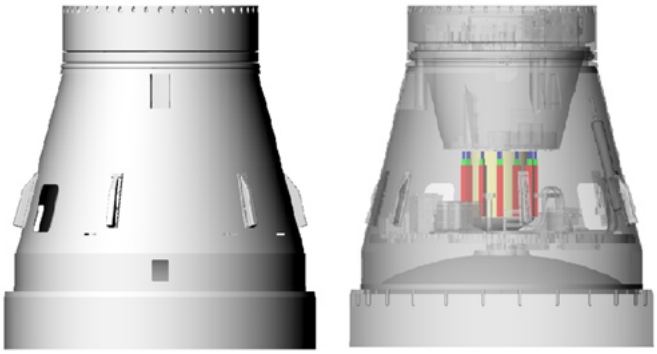

Figure 4.3: A possible capsule integration in the sounding rocket interstage

As already discussed in Section 4.1, a trade-off study will be performed between two possible solutions, the former characterized by a half-cone angle of 45° and the latter by a half-con angle of 60°, in order to select the most suitable configuration. The analyzed configurations are shown in Figure 4.4 and Figure 4.5 in folded, intermediate and completely deployed configurations, respectively. They have been designed in order to provide the same reference diameter and almost the same re-entry mass, in accordance with the values reported in Table 4.1.

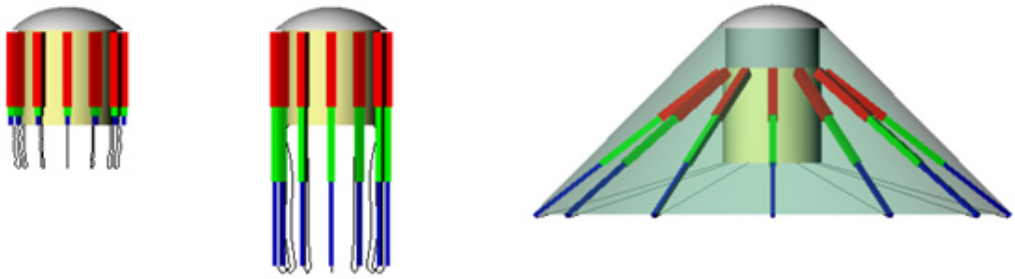

Figure 4.4: Aerodynamic configuration characterized by a half-cone angle of 45°

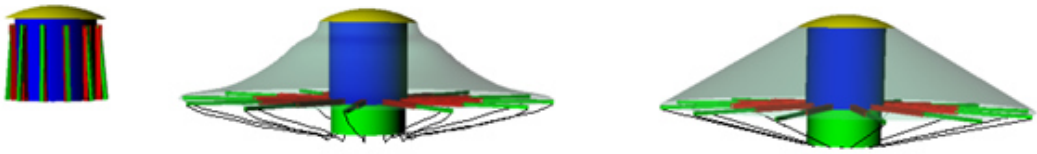

Figure 4.5: Aerodynamic configuration characterized by a half-cone angle of 60°

In the first design solution, depicted in Figure 4.4, the telescopic rods are initially closed and parallel to the cylindrical body of the capsule. The heat shield deployment is performed in two phases. In the first phase, represented in second picture of Figure 4.4, the rods elongate remaining almost parallel to the cylindrical surface of the payload container and the TPS fabric almost completely tensioned. In the second phase, represented in the third picture of Figure 4.4, the heat shield is deployed thanks to the sliding of a cylindrical supporting structure coaxial with the payload bay, able to guarantee the hinged rods rotation so to reach a half-cone angle of 45°.

In the second design solution, shown in Figure 4.5, the mechanical rods are split in two sections, able to rotate and deploy as depicted in the second picture of Figure 4.5. In this case the final tensioning is applied through the metallic threads attached at the bottom sliding structure and a half-cone angle of 60° is reached.

From an aerodynamic point of view there are therefore two main differences, which will be supported by some of the results reported in the following Sections:

- the first configuration is more stable than the second one and, for the first configuration, aerothermal and mechanical loads more steeply reduce moving from the nose towards the flexible aerobrake;
- the second configuration is characterized by a larger drag coefficient with respect to the first one. The second capsule (having the same mass and reference surface of the first one) has therefore the advantage to be characterized by a lower ballistic parameter, leading to lower aerothermal and mechanical loads during re-entry.

4.1.2 Technology demonstrator for REXUS sounding rocket

The second suborbital mission scenario analyzed is characterized by a relatively low energy re-entry environment. It could be exploited to test the system, mainly from the aerodynamic and the mechanical points of view and to collect data in less severe entry conditions. This kind of scenario can therefore represent a reliable flight test basis for all the more complex, high-energy entry paths presented in this work, as also discussed in Section 1.5.2.

This mission foresees that the capsule safely lands a dummy payload, mainly consisting of onboard electronics and of the recorded flight data, preserving its structural integrity and availability. All the data acquired during the re-entry phase will be collected on SD cards and, possibly, continuously downlinked to the ground to increase the mission reliability.

Thus, through post-processing operations, data could be exploited to:

- show the effectiveness of the innovative re-entry strategy;
- validate theoretical models and pre-flight simulations;
- refine the design for future missions.

Considering the available volumetric envelope in the REXUS nosecone, and the relatively low energy re-entry scenario provided by this sounding rocket, a down-scaled version of the configuration presented in Section 4.1.1 has been considered.

The characteristics geometric parameters for the configuration are reported in Table 4.1 and in Figure 4.6. The cylindrical payload bay has a diameter of 20 cm and the aerobrake forms a half-cone angle of 45° with respect to the capsule symmetry axis. The rigid nosecone is characterized by a smaller radius of curvature than the one foreseen for the demonstrator launched by the MAXUS rocket. This aspect is not critical for this mission, considering that, as will be shown in the following, the thermal loads encountered during the re-entry path are largely sustainable by Commercial Off The Shelf (COTS) materials. In Figure 4.6 it is also specified that also in this case a sliding structure, able to increase the capsule height of about 10 centimetres, is foreseen for the deployment sequence.

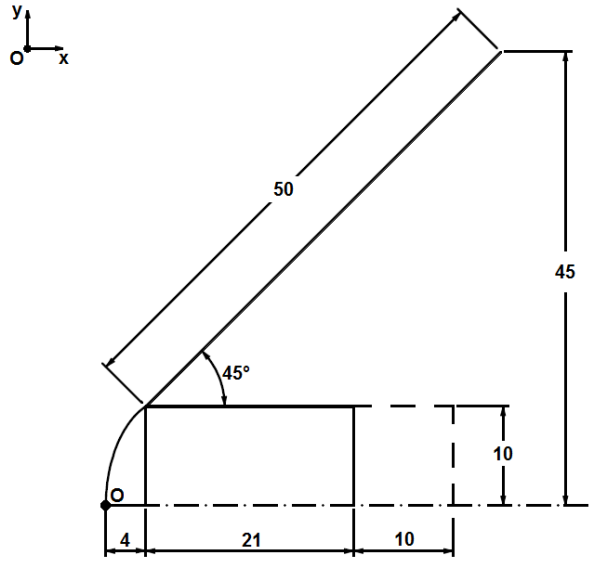

Figure 4.6: Re-entry demonstrator for a mission onboard REXUS sounding rocket

Figure 4.7 shows some CAD renderings of the folded and deployed configuration under investigation.

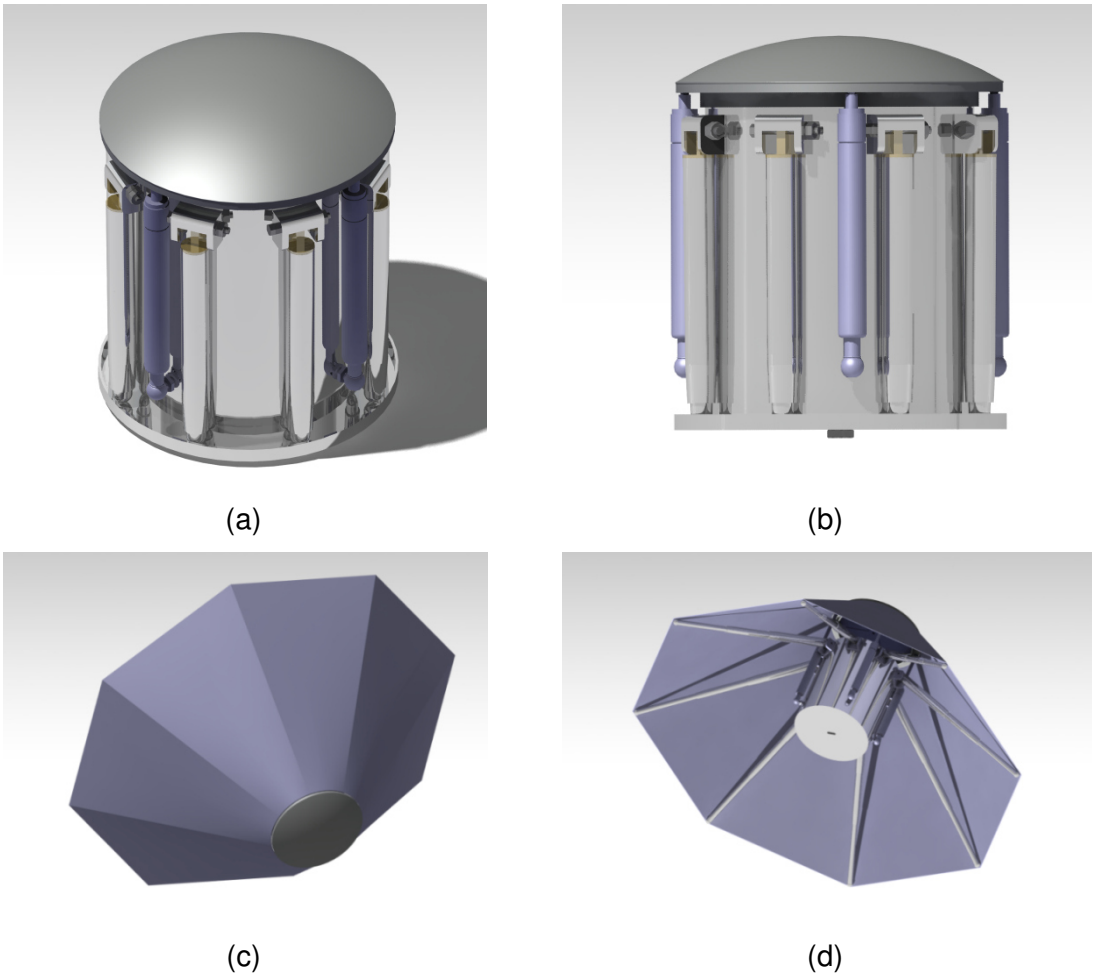

Figure 4.7: CAD renderings of the analyzed configuration

In this Section the deployment mechanism preliminarily designed for the analyzed configuration is also presented in Figure 4.8 through Figure 4.11. Basically, the design is oriented towards the low complexity and the use of COTS components.
In folded configuration the telescopic rods (label 4 in Figure 4.8) are kept closed thanks to light blue aluminium disk (label 7) constrained under the grey cylindrical box (label 1) by means of an electronic lock, while the nose cap (label 3) is constrained to the top of the cylindrical payload bay (label 6) thanks to an electronic lock similar to the previous one.

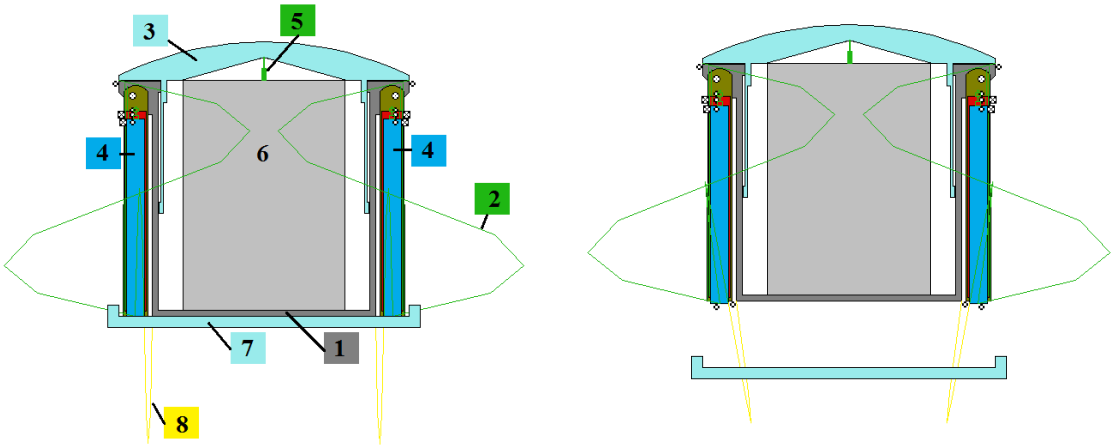

(a) (b)

Figure 4.8: Capsule in folded configuration (a) and aluminium disk ejection (b)

When foreseen by the mission profile, an electric impulse unlocks the first electronic lock. The aluminium disk, no more constrained, is therefore ejected, as also depicted in Figure 4.8(b). At this stage, the telescopic rods are free to extend taking advantage from inside preloaded springs and the green fabric (label 2) is partially tightened (see Figure 4.9).

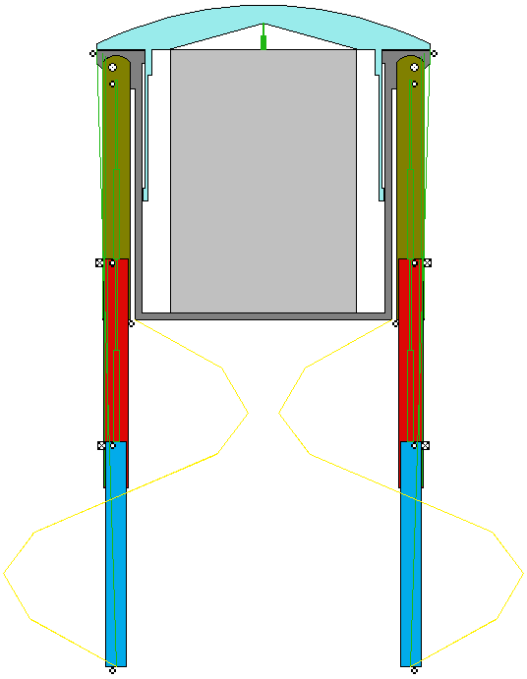

Figure 4.9: Telescopic rods extension

A number of torsional springs can guarantee a small rotation of the telescopic rods, providing the necessary arm in order to complete in an easy way the rotation during the following step. A second electric impulse will unlock the second electronic lock. Some actuators or gas springs (label 5) can lift up the sliding structure and the nose cap. In this way the aerobrake is deployed, completing the full rotation of telescopic rods (see Figure 4.10 and Figure 4.11).

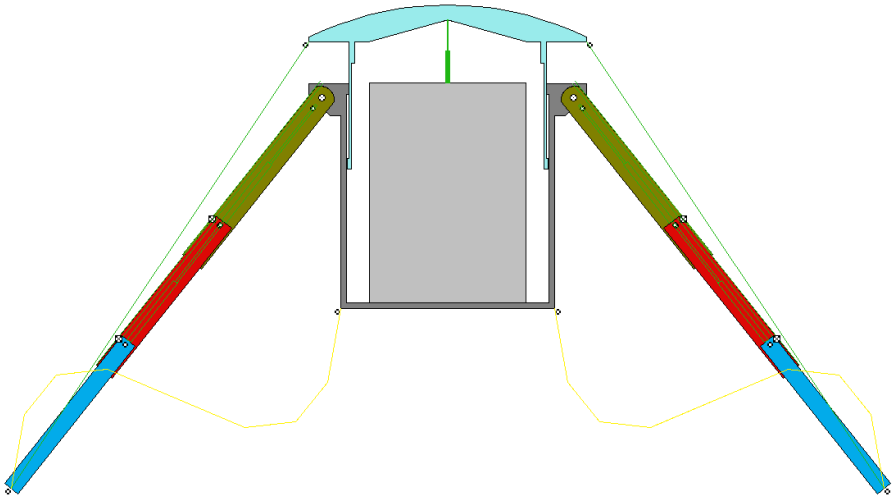

Figure 4.10: Preliminary rods rotation and nose lift up

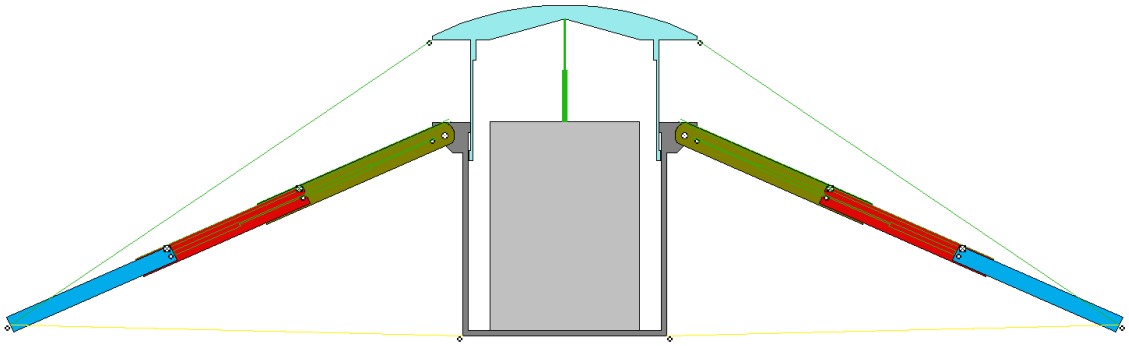

Figure 4.11: Final aerobrake deployment

Finally, lower threads (label 8) hinged to the main body of the capsule and to the third part of the telescopic rods serve to avoid that the pressure load acting on the fabric during re-entry can refold again the aerobrake.

4.2 Mission analysis

4.2.1 Technology demonstrator for MAXUS sounding rocket

The trajectory computation for the technology demonstrator launched onboard the MAXUS rocket has been performed assuming the capsule parameters listed in Table 4.1 and the initial conditions reported in Table 4.3.

H [km]	V [km/s]	γ [°]	λ [°]	Λ [°]
150	3.20	87.0	67.9	21.1

Table 4.3: Initial parameters for trajectory computations

The parabolic trajectory of the capsule above 100 km altitude is shown in Figure 4.12.
Re-entry trajectory computations below 100 km altitude have been performed for both the half-cone angle configurations. As already discussed in Section 4.1, they differ for the ballistic parameter (due to the different drag coefficient) and for the radius of curvature at the stagnation point (so that the nose cone is tangent to the conical part of the aerobrake). The most meaningful results are plotted in Figure 4.13.
It is evident that, due to the slightly lower ballistic parameter, the 60° half-cone angle capsule exhibits a larger deceleration at higher altitudes, when compared with the 45° half-cone capsule.

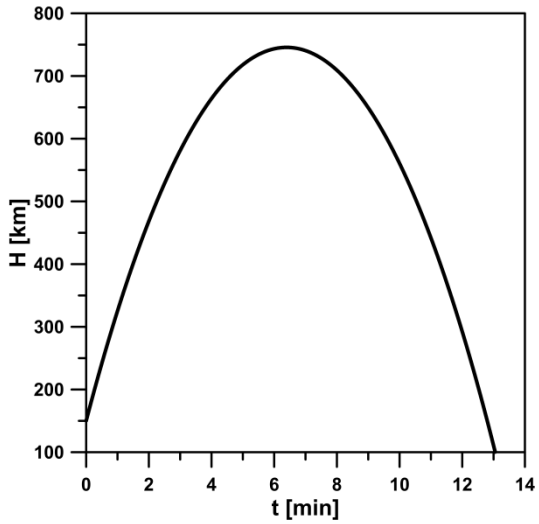

Figure 4.12: Capsule parabolic trajectory above 100 km altitude

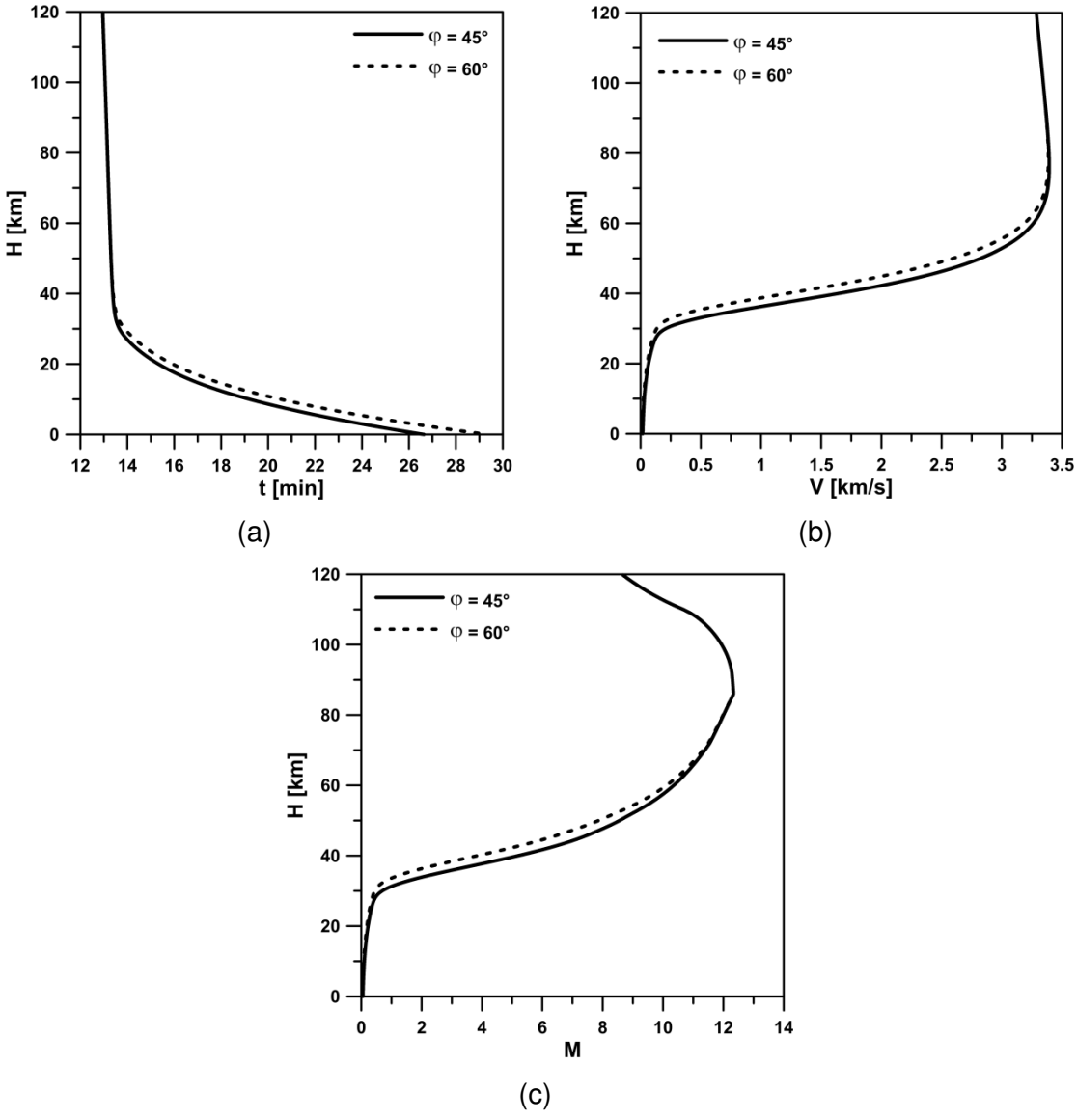

Figure 4.13: Re-entry trajectories for the analyzed configurations: Time (a), Velocity (b) and Mach number (c) as functions of the Altitude

The aerothermal and mechanical loads have been calculated along the trajectories according to the engineering models discussed in Section 2.1.1 and plotted in Figure 4.14.

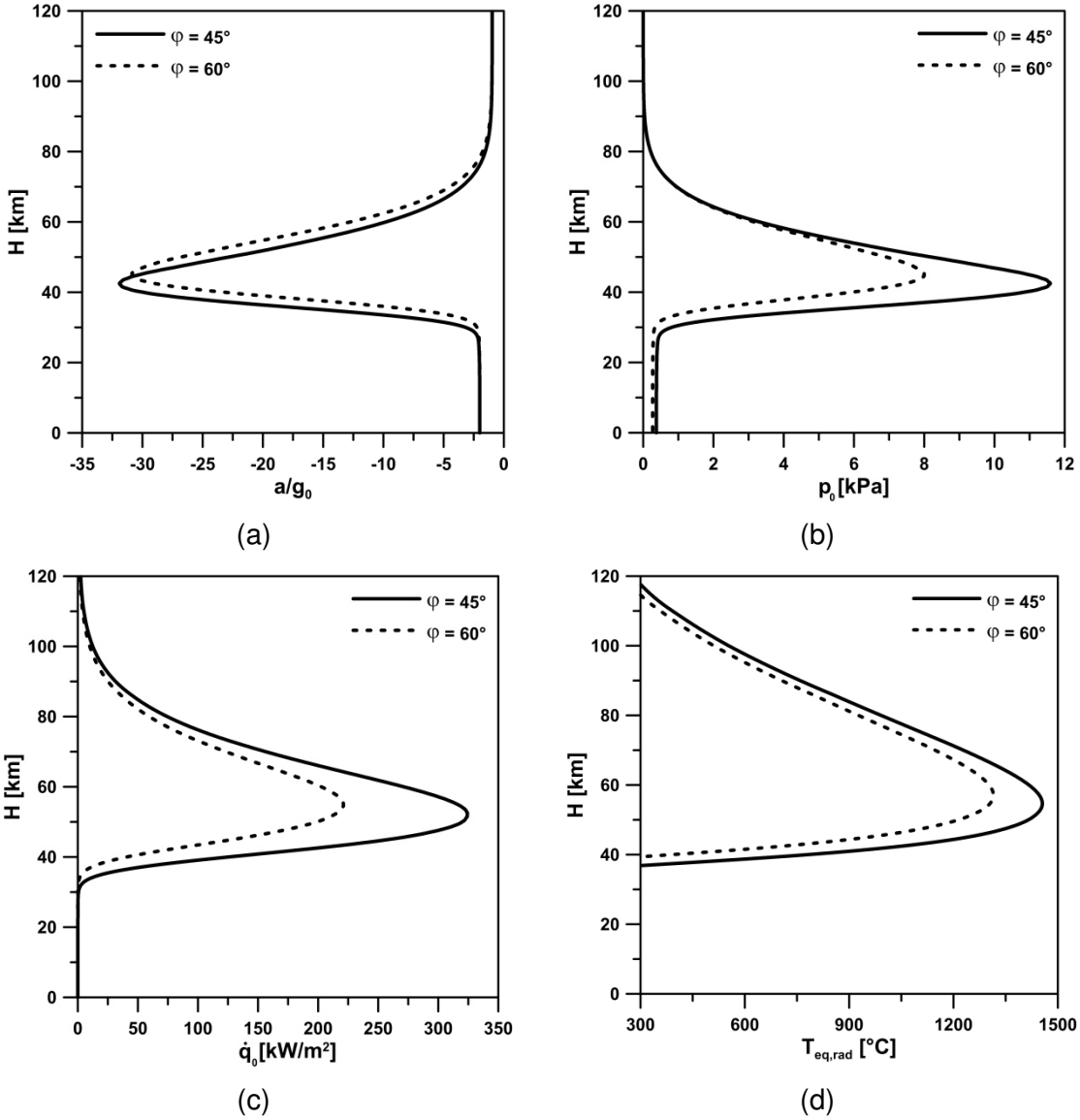

Figure 4.14: Thermal and mechanical loads variation for the analyzed configurations: Acceleration (a), Stagnation-point pressure (b), Stagnation-point heat flux (c) and Radiation equilibrium Temperature (d) as functions of the Altitude

It is evident that the ballistic parameter reduction for a 60° half-cone angle configuration would be obviously beneficial for a stagnation-point heat flux and pressure reduction (while the maximum deceleration, as well known, is not significantly affected by the ballistic parameter variation). Nonetheless, maximum aerothermal and mechanical loads are not the only parameters driving the choice of the final configuration, as it will be pointed out in the following.

The re-entry trajectories reported in Figure 4.13 and in Figure 4.14 have been evaluated considering the heat shield completely deployed in the exoatmospheric phase of the trajectory and assuming that the capsule reaches the conventional re-entry interface altitude (i.e. 100 km) with a proper attitude.

The effect on thermal and mechanical loads due to a heat shield deployment below 100 km altitude is now considered. This can be useful to investigate the effects of an undesired malfunctioning of the deployment mechanism or to study the possibility that the deployment procedure be completed only below the entry interface, in order to take advantage from the aerodynamic stability of the folded configuration that should be able to guarantee the proper re-entry attitude. The 45° half-cone angle configuration has been considered, but similar conclusion can be obtained for a 60° half-cone angle.

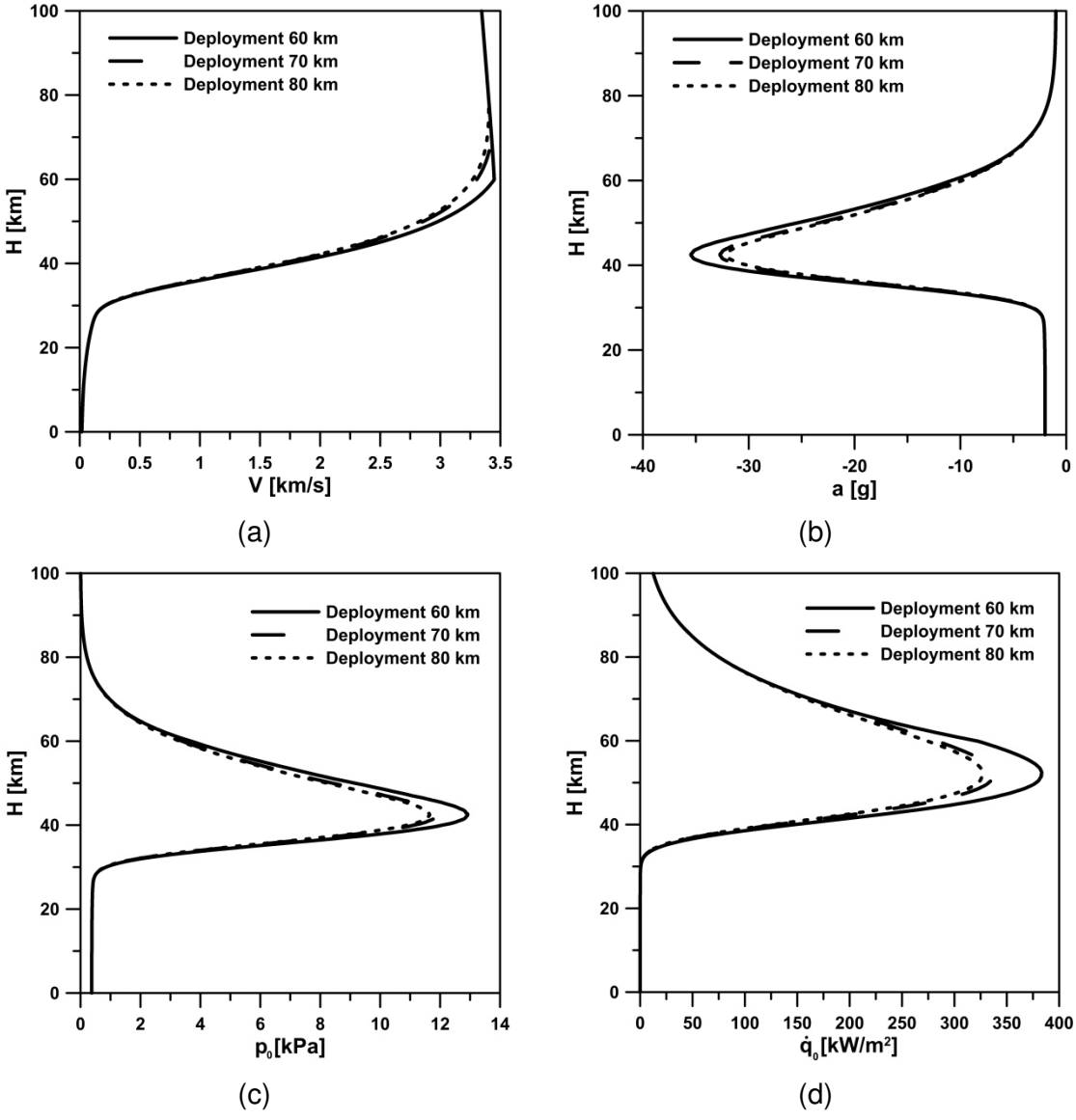

Figure 4.15: The effect of a delayed heat shield activation on the re-entry trajectory and on aerothermal and mechanical loads: Velocity (a) Acceleration (b), Stagnation-point pressure (c), Stagnation-point heat flux (d) as functions of the Altitude

Figure 4.15 reports the outcomes of the above mentioned analysis, both in terms of re-entry trajectory and in terms of aerothermal loads. It is evident that the aerobrake deployment up to an altitude of 70 km does not significantly affect any significant flow variable. On the contrary, deploying the aerobrake around 60 km, a sensible parameters variation may be noticed. It is therefore advisable not to foresee a heat shield deployment activation below 70 km altitude in this case.
When considering the option to take advantaged from aerodynamic forces for attitude stabilization before aerobrake deployment, however, one should be also consider that the duration of the re-entry phase in the range of altitudes between 120 km and 30 km is only 25 seconds; while the capsule altitude changes from 80 km to 60 km in only 6 seconds. For this reason, stabilization by aerodynamic forces before heat shield deployment can be highly risky, particularly in case of uncertainties in the flight trajectory.

4.2.2 Technology demonstrator for REXUS sounding rocket

The trajectory computation for the technology demonstrator launched onboard the REXUS rocket has been performed assuming the capsule parameters listed in Table 4.1 and the initial conditions reported in Table 4.4. In particular, initial altitude, velocity and flight path angle refer to potential conditions at the trajectory apogee, based on flight data relative to past missions (29). In addition, in this case the heat shield has been supposed to be completely deployed at the apogee.

H [km]	V [m/s]	γ [°]	λ [°]	Λ [°]
90	250	0	67.9	21.1

Table 4.4: Initial parameters for trajectory computations

Nominal re-entry trajectories are reported in Figure 4.16, while in Figure 4.17 the main thermo-mechanical variables are plotted along the trajectory. It is clear that the present demonstrative mission is not properly useful for the aerothermal testing of the capsule, considering that the experienced heat flux is two orders of magnitude lower than the one characterizing an orbital re-entry or a parabolic flight at higher energy.
Nonetheless, as already discussed, technology demonstrative missions onboard a low-energy class of sounding rockets can lead to meaningful results for the flight testing of the deployment mechanism and for the capsule aerodynamic stabilization.

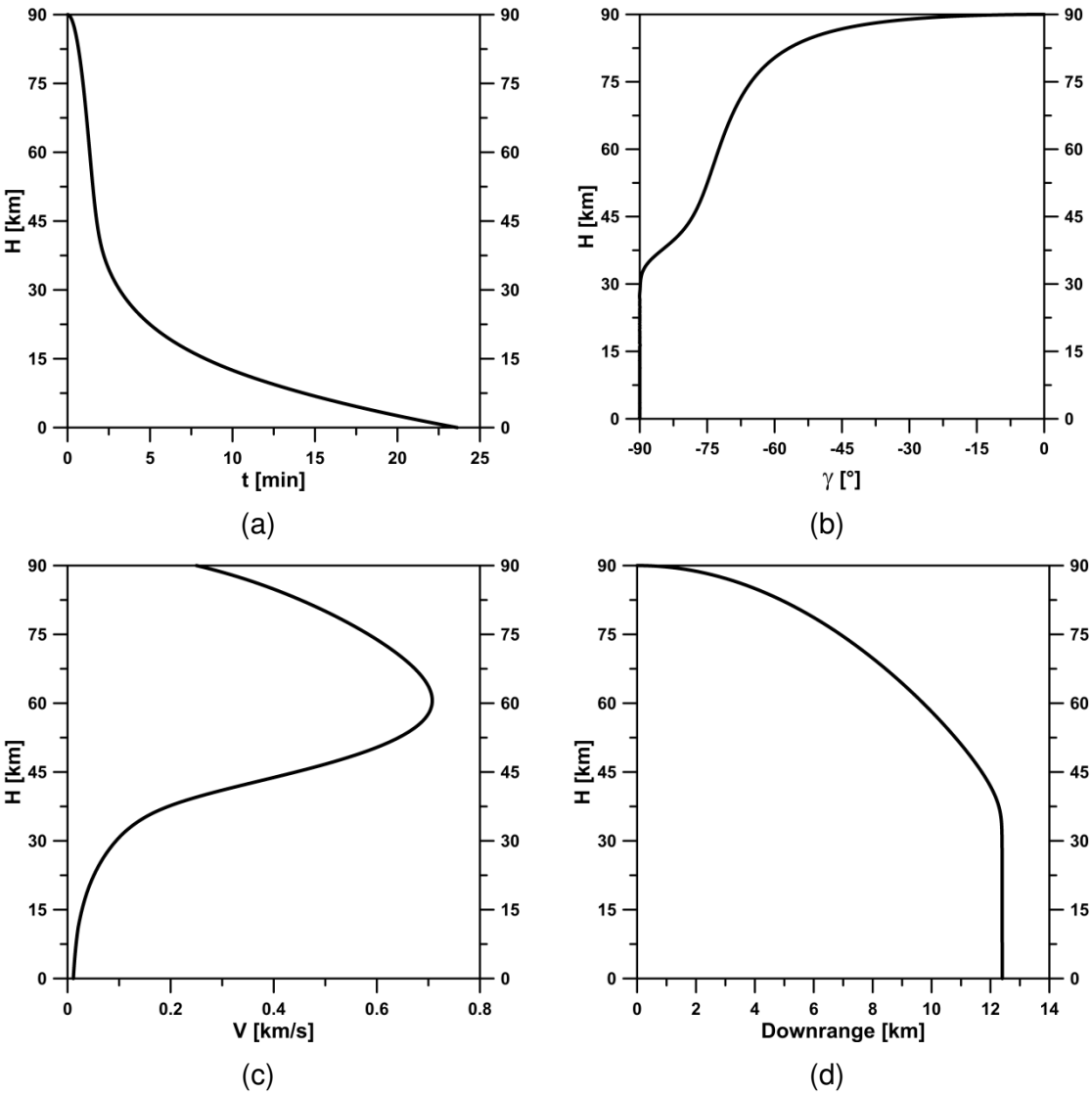

Figure 4.16: Re-entry trajectories for the analyzed configurations: Time (a), Flight Path Angle (b), Velocity (c) and Downrange (d) as functions of the Altitude

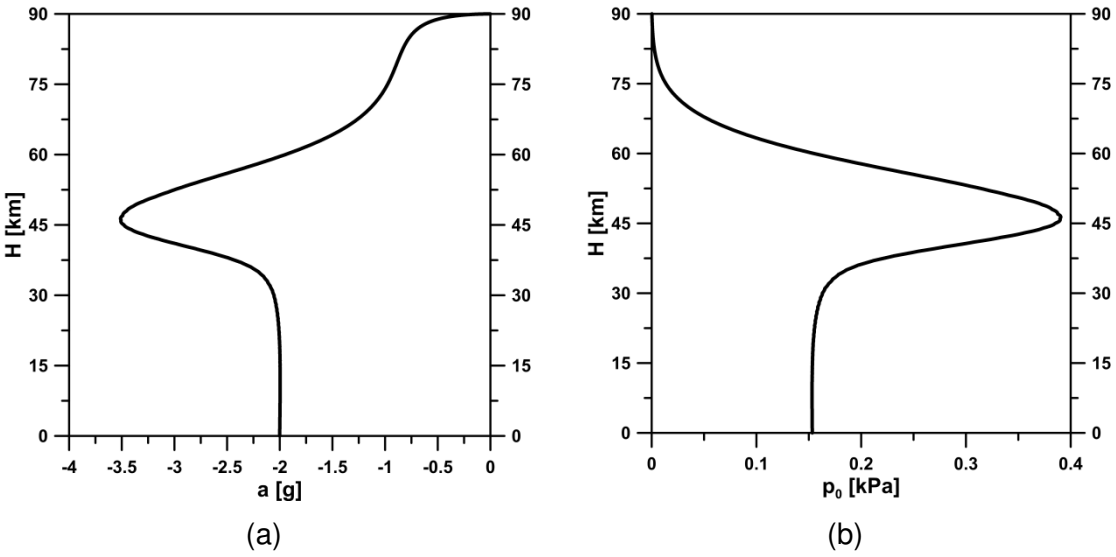

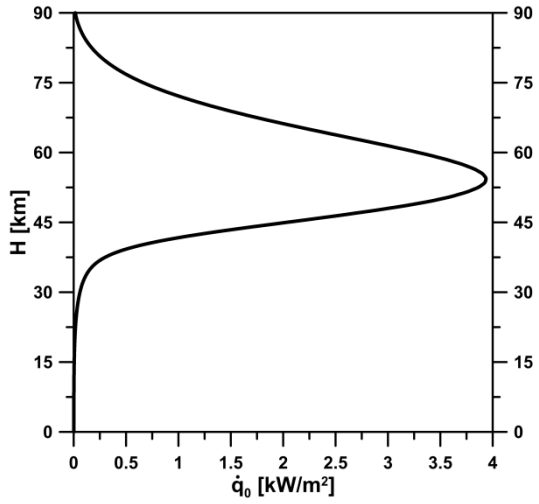

(c)

Figure 4.17: Thermal and mechanical loads variation for the analyzed configurations: Acceleration (a), Stagnation-point pressure (b), Stagnation-point heat flux (c) as functions of the Altitude

In this case a landing dispersion analysis similar to the one already discussed in Section 3.2.2.2, has been also performed. The input random parameters are reported in Table 4.5 through Table 4.7.

Variable	Average Value	3-σ Variance
Initial altitude [km]	90	0.500
Initial velocity [m/s]	250	1.000
Initial flight path angle [°]	0	0.01

Table 4.5: Mission uncertainties connected with the entry interface

Variable	Average Value	3-σ Variance
Capsule mass [kg]	5.0	0.010
Drag coefficient [-]	Equation 3.1	0.10
Lift coefficient [-]	0	0.010
Reference Surface [m^2]	0.64	0.010

Table 4.6: Mission uncertainties connected with the capsule configuration

Variable	Average Value	3-σ Variance
Air density [kg/m^3]	Standard atmosphere	10%
Wind velocity [m/s]	0	10

Table 4.7: Mission uncertainties connected with the atmospheric conditions

The statistical distributions of the aerothermal and mechanical loads is plotted in Figure 4.18, while the landing dispersion in terms of downrange and landing point location is depicted in Figure 4.19.

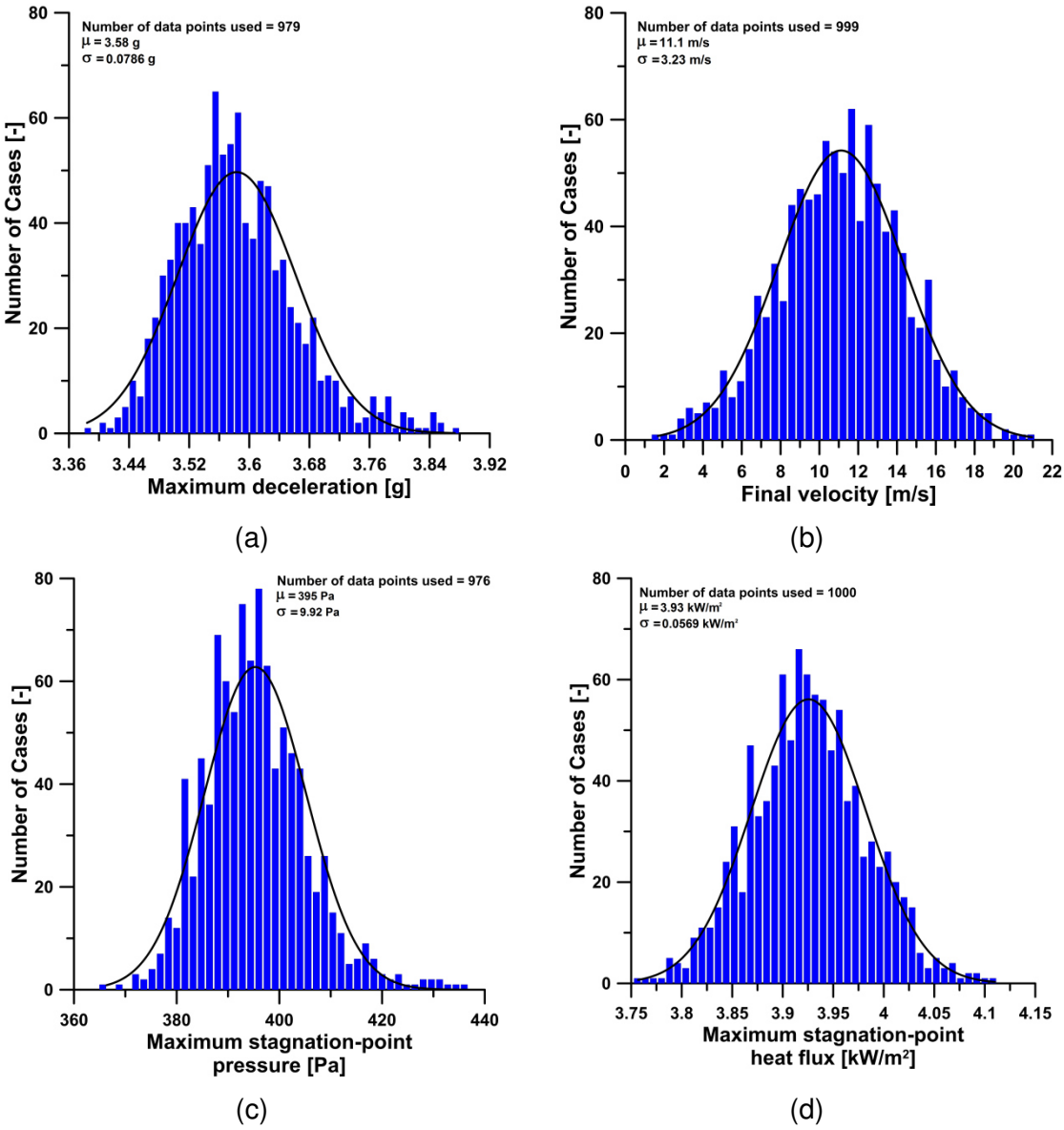

Figure 4.18: Statistical distribution of the maximum deceleration (a), the terminal velocity (b), the maximum stagnation-point pressure (c) and the maximum stagnation-point heat flux (d)

It is clear from Figure 4.19 that in this case the landing profile is quite far from the classical elliptical footprint. Investigating which uncertainty factor affected this behaviour, it was found that neglecting the uncertainty regarding the lift coefficient, a more classical result was found, as reported in Figure 4.20. It is therefore clear that for a lower energy entry the aerodynamic coefficients produce a larger impact on downrange standard deviation and on the impact point location.

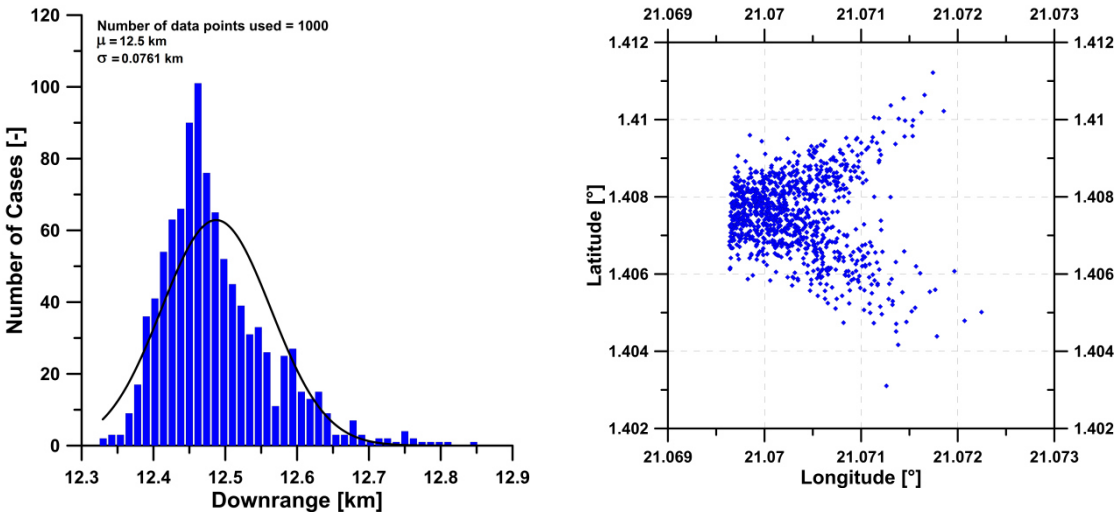

Figure 4.19: Landing dispersion in terms of downrange and landing point location

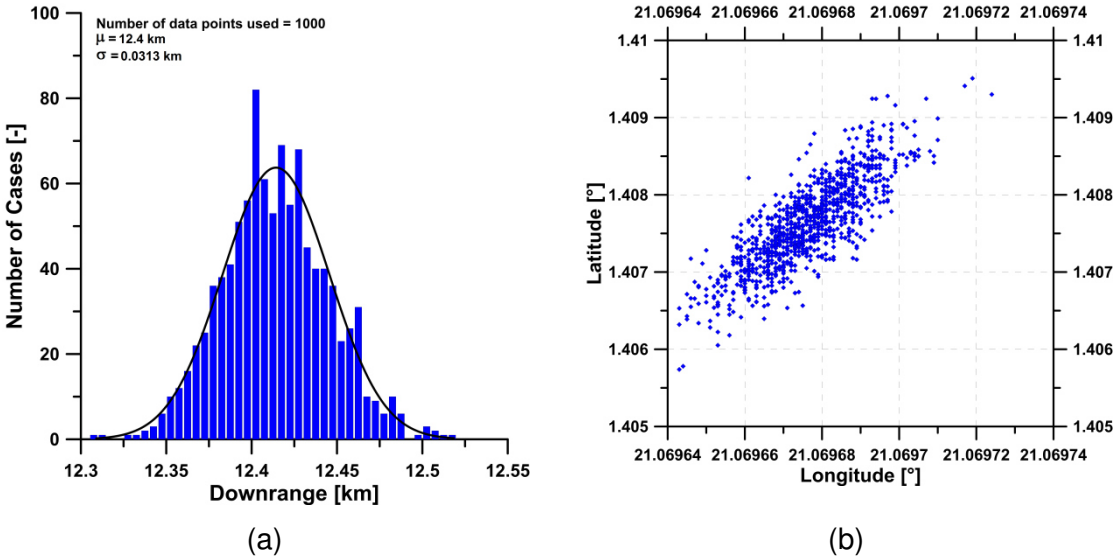

Figure 4.20: Landing dispersion in terms of downrange and landing point location, neglecting the uncertainty on the lift coefficient

4.3 Aerodynamic analyses

4.3.1 Technology demonstrator for MAXUS sounding rocket

4.3.1.1 Aerodynamic stability

As far as the aerodynamic static stability is concerned, in this Section the capsule aerodynamic behaviour in folded and deployed configuration has been analyzed in the entire range of variability for the angle of attack (0°-180°). Then, the influence of the

half-cone angle on the pitching moment of the fully-deployed configuration has been considered with respect to the nominal re-entry attitude.

The capsule aerodynamic stability in folded configuration has been evaluated performing CFD simulations of the flowfield around the hemispherical nose and the cylindrical body, without considering the presence of the deployed conical fabric. Simulations have been carried out for angles of attack varying from 0° to 180°, with a step of 30°. The asymptotic conditions correspond to the one encountered at 100 km altitude.

As it is possible to see from Figure 4.21, reporting the pitching moment coefficient as a function of the angle of attack, assuming a centre of gravity located on the longitudinal axis 10 cm distance from the nose tip, the capsule exhibits two trim angles of attack (0° and 180°). Nonetheless, it can be noticed a static stability behaviour with respect to the nominal re-entry attitude, while the reverse equilibrium attitude is statically unstable. This behaviour guarantees that the capsule will be aerodynamically self-stabilized when the aerobrake is folded.

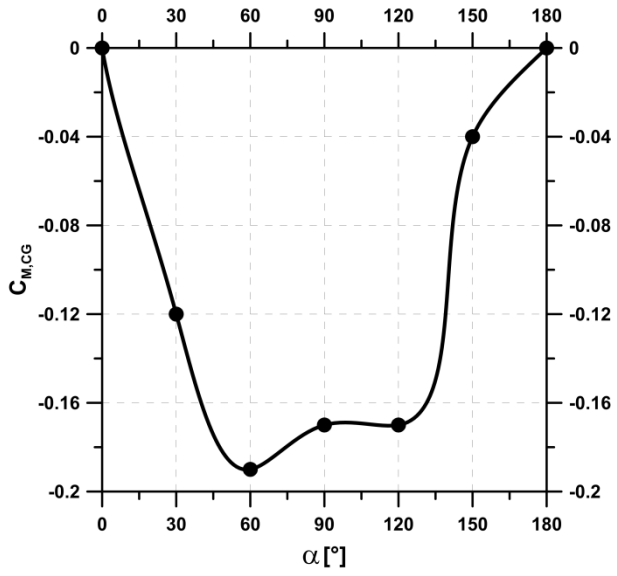

Figure 4.21: Pitching moment coefficient variation as a function of the angle of attack for the capsule in folded configuration (centre of gravity located 10 cm distance from the nose tip)

A similar analysis has been performed for the capsule in deployed configuration, in particular for 60° half-cone angle. Similar results apply to the 45° half-cone angle configuration, in particular for what concern the stability behaviour around the reverse equilibrium attitude. As far as the stability derivative around the nominal re-entry attitude is concerned, much more influenced by the half-cone angle, a dedicated analysis is reported in the following, with a comparison between the two analyzed configurations.

Figure 4.22 shows the pitching moment coefficient variation as a function of the angle of attack assuming again the centre of gravity located on the longitudinal axis 10 cm distance from the nose tip. In this case the reverse equilibrium condition is statically stable (being the pitching moment derivative in the order of -0.0035 deg^{-1}). However, the stability derivative is much less (in absolute value) in comparison to the corresponding value at the nominal attitude.

Considering that an aerodynamic self-stabilization cannot be guaranteed with the deployed heat shield and the problems connected with the possible aerobrake activation below the re-entry interface (see Section 4.2.1), additional stabilization methods can be considered (e.g. spin stabilization, reaction wheels etc.). In this case, it is important to take into account that the average aerodynamic torque to be compensated by the attitude control system in the exoatmospheric flight (i.e. above 150 km) has been estimated in the order of 10^{-5}-10^{-4} N·m; in particular the average disturbance moments range from O(10^{-6}) N·m at 300 km to O(10^{-4}) N·m at 150 km.

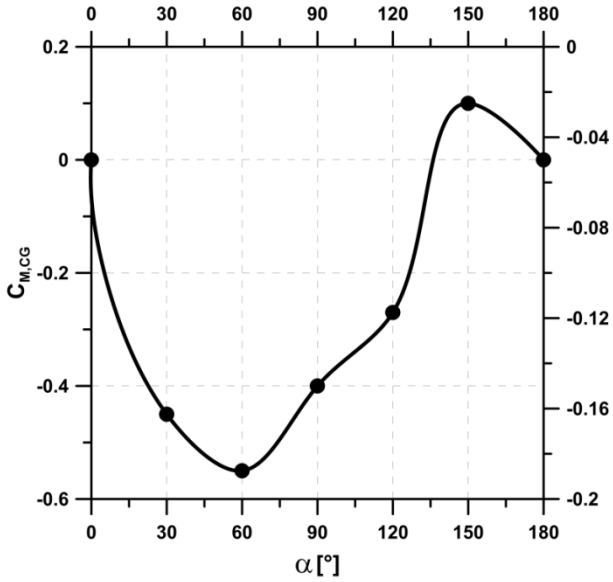

Figure 4.22: Pitching moment coefficient variation as a function of the angle of attack for the capsule in deployed configuration (centre of gravity located 10 cm distance from the nose tip)

Finally, the aerodynamic stability has been investigated around the nominal re-entry attitude to compare the 45° and 60° half-cone configurations, considering again the centre of gravity located on the longitudinal axis 10 cm distance from the nose tip.

From Table 4.8 it can be seen that both the capsule are stable with respect to the nominal re-entry attitude but, as also well known from the literature, the 45° half-con angle configuration exhibits a higher static stability than the 60° configuration. This behaviour would suggest to select, from this point of view, the 45° half-cone

configuration, which will be also exhibit, according to literature data, also a higher dynamic stability (47), (48), (49).

	φ = 45°	φ = 60°
$C_{M\alpha}$ [deg^{-1}]	-0.0281	-0.0150

Table 4.8: Pitching moment derivative for the analyzed capsules in deployed configuration (centre of gravity located 10 cm distance from the nose tip)

4.3.1.2 Aerothermodynamic loads evaluation

The aerothermodynamic loads have been estimated by means of 2D CFD calculations, considering both the half-cone angle configurations, for the maximum stagnation-point heat flux conditions.

In addition, the analysis includes the effect of the flexible heat shield bending under the pressure load. In particular, a fabric curvature characterized by a maximum displacement of 1 centimetre in the direction perpendicular to the one of the rigid aerobrake has been considered, according to the results of a non-linear structural analysis (50).

In Figure 4.23 the non dimensional convective heat flux distributions along the capsule surface have been compared for two significant points of the suborbital re-entry trajectory (maximum stagnation-point convective heat flux and pressure conditions) and for a reference profile relative to an orbital re-entry scenario. It is evident that, for both the half-cone angles, similar trends can be observed. For each half-con angle it is therefore possible to assume the corresponding non dimensional profile applicable along the entire re-entry trajectory. Scaling these profiles with the stagnation-point heat flux evaluated in a certain condition of the trajectory by means of the Tauber's engineering formula reported in Equation 2.4, it is possible to have a first order approximation of the heat flux distribution along the capsule surface in any re-entry condition.

In addition, Figure 4.23 shows another advantage of the 45° half-cone angle configuration. Despite the larger heat fluxes at the stagnation-point (due to the slightly larger ballistic parameter), for this configuration a steeper reduction of the convective heat flux can be observed with respect to the configuration characterized by a half-cone angle of 60°. In the first configuration the flexible high temperature resistant fabric therefore experiences less severe aerothermal conditions.

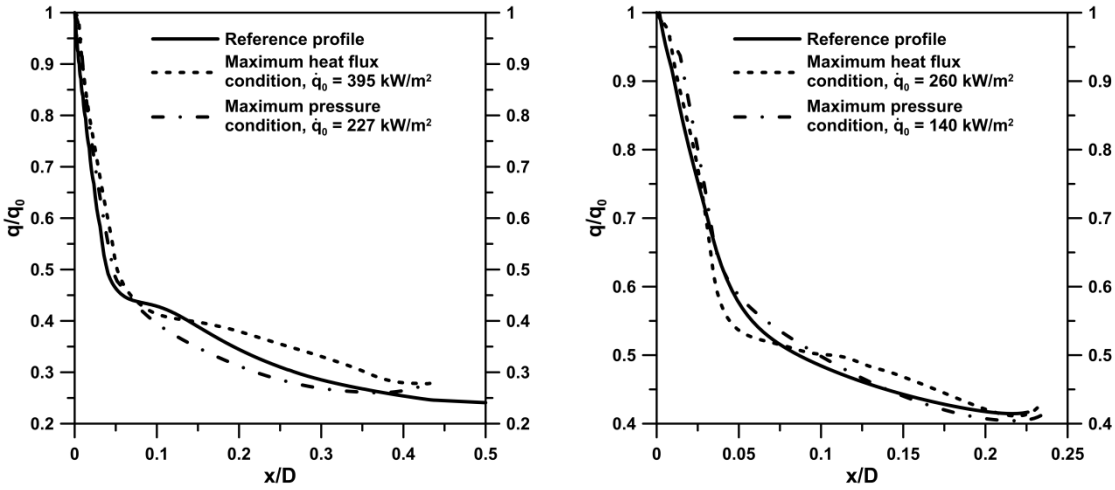

Figure 4.23: Non dimensional convective heat flux distributions along the capsule surface for the 45° (a) and 60° half-cone angle configuration

In Figure 4.24 the pressure profiles on the capsule surface as functions of the coordinate along the longitudinal axis are reported. It is evident that in both cases the fabric bending produces an additional compression shock wave, but the effect is much more important for the 60° half cone angle. This is an additional driving factor for the choice of the 45° half-cone angle configuration.

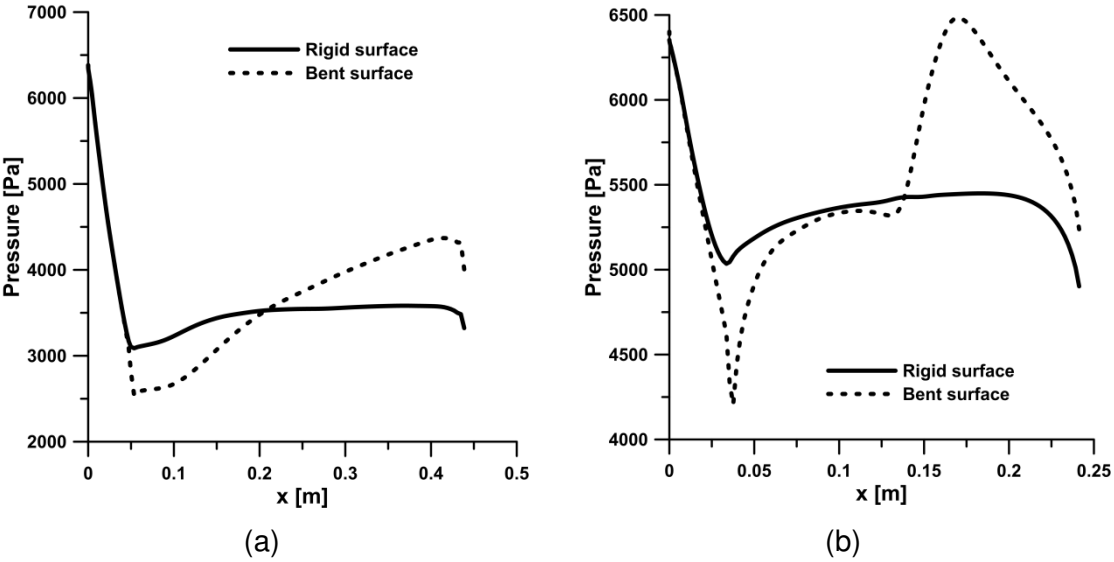

Figure 4.24: Pressure profiles on the capsule surface for the 45° (a) and 60° (b) half-cone angles

4.3.2 Technology demonstrator for REXUS sounding rocket

4.3.2.1 Aerodynamic load evaluation

Also for the mission scenario onboard REXUS sounding rocket, 2D CFD analyses have been performed to evaluate the main loads distribution on the capsule surface. However, differently from other mission profiles, in this case only the pressure profile has been reported, considering the very low incidence of the aerodynamic thermal loads for the analyzed scenario. The pressure profile, in the point of the trajectory where a peak value at the stagnation-point is expected, is reported in Figure 4.25, while the corresponding pressure contour is shown in Figure 4.26.

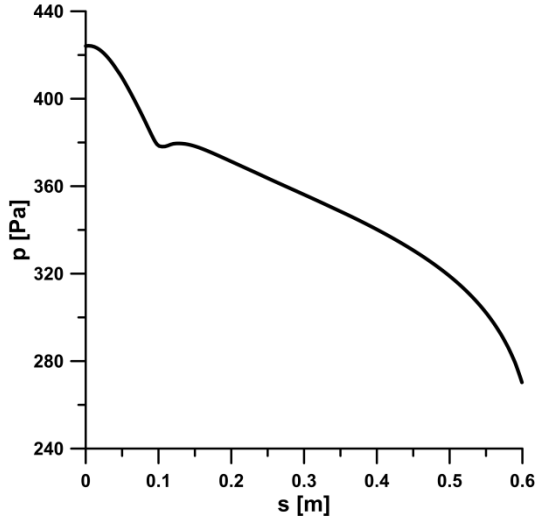

Figure 4.25: Pressure profile along the capsule surface for the maximum stagnation-point pressure condition of the entry trajectory

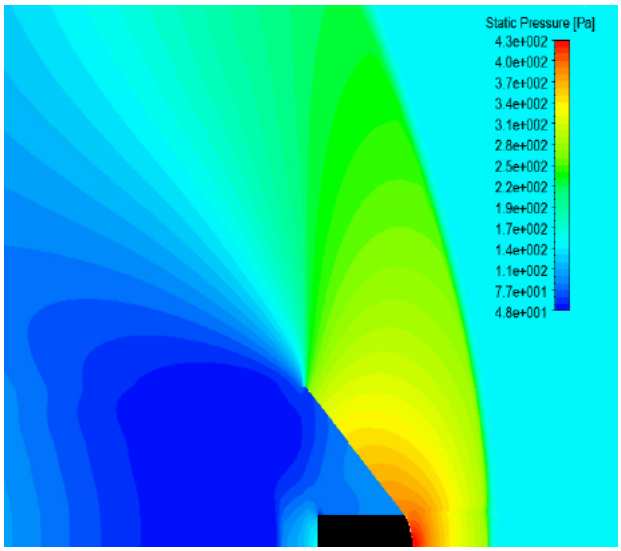

Figure 4.26: Pressure contour for the maximum stagnation-point pressure condition of the entry trajectory

It has been already pointed that, for the mission profile under consideration, dynamic and thermal loads are not so relevant, when compared to a high-energy re-entry profile. Nonetheless, their numerical estimation could serve to validate the numerical method also against potential flight data. In addition, this mission can serve as a preliminary opportunity to test in-flight the system at supersonic conditions that reproduce very well the final leg of a higher energy re-entry.

4.3.2.2 Aerodynamic stability

For the mission scenario onboard the REXUS sounding rocket, stability analyses have been carried out at different altitudes along the entry trajectory and at different locations of the Centre of Gravity. The altitudes considered for the present analysis are in the range 70-50 km. The corresponding input data to CFD analyses are reported in Table 4.9 in terms of free stream velocity, Mach number, pressure, temperature and Reynolds number.

H [km]	V [m/s]	M [-]	p [Pa]	T [K]	Re_D [-]
70	647.4	2.18	5.20	219.5	2710
60	706.5	2.25	20.3	245.4	10716
50	593.5	1.80	77.7	270.6	30008

Table 4.9: Input data to CFD analyses for longitudinal stability analyses

In Figure 4.27, at the altitude of 70 km, the variation of the moment coefficient around the z-axis with the angle of attack is reported. The range of angle of attack between 0° and 180° and different positions of the centre of gravity have been considered (both on and off the longitudinal axis).

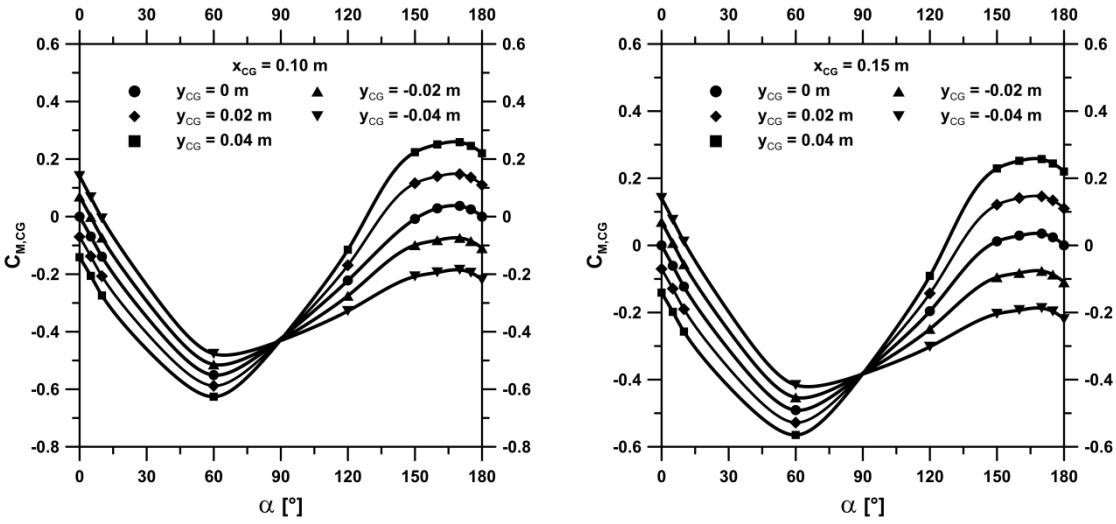

(a) (b)

Figure 4.27: Longitudinal moment coefficient as a function of the angle of attack at five different centre of gravity positions at fixed longitudinal coordinates, 0.1 m (a) and 0.15 m (b) distance from the nose tip

For the CoG located on the longitudinal axis of the capsule ($y_{CG} = 0$), results show two stability conditions around 0° and 180°, and an unstable equilibrium condition around 150°. It is also evident that the reverse equilibrium condition is much less stable than the nominal equilibrium condition. In addition it is clear that properly choosing a CoG location off the longitudinal axis (in particular below it), a unique stable equilibrium condition characterized by an angle of attack around 5°-10° can be obtained. Generally a relatively large trim angle of attack could result in over loading of the conical part of the capsule, but for this scenario dynamic and, in particular, thermal loads are not so critical, as also discussed in Section 4.3.2.1.

In addition, a backward movement of the CoG decreases the absolute value of the stability derivative around both the nominal and reverse re-entry attitude.

Then, the computation of the stability derivatives around the nominal and the reverse equilibrium condition for three different points of the re-entry trajectory (see Table 4.9), are reported in Table 4.10 and Table 4.11 for the CoG located on the longitudinal axis 10 and 15 centimetres distance from the nose tip, respectively.

	$dC_{M,CG}/d\alpha$ [1/deg]	
H [km]	NEC	REC
70	-0.014	-0.0037
60	-0.013	-0.0026
50	-0.012	-0.0033

Table 4.10: Stability derivatives evaluated at three re-entry conditions for the CoG located on the longitudinal axis at 10 centimetres distance from the nose tip

	$dC_{M,CG}/d\alpha$ [1/deg]	
H [km]	NEC	REC
70	-0.012	-0.0035
60	-0.012	-0.0024
50	-0.011	-0.0030

Table 4.11: Stability derivatives evaluated at three re-entry conditions for the CoG located on the longitudinal axis at 15 centimetres distance from the nose tip

4.3.2.3 Unsteady analysis for dynamic behaviour characterization

In the present Section results obtained by an unsteady CFD model are presented. The unsteady model is based, in particular, on a first order temporal discretization and on a fully implicit scheme (having the advantage to be unconditionally stable with respect to the time step size). The objective of the analyse is to give preliminary information about the time oscillations of some aerodynamic characteristic parameters, such as the force and moment coefficients or the pressure acting on the fabric surface. Such oscillations are caused by the unsteady flow characteristics present in the capsule wake, essentially unsteady due to the vortex shedding from the capsule.

The analyzed case study considers the trajectory condition characterized by the maximum dynamic pressure and an angle of attack of 20° (see Table 4.12).

H [km]	α [°]	V [m/s]	M [-]	p [Pa]	T [K]	Re_D [-]
40	0	381	1.2	278	251	77068

Table 4.12: Input data for the unsteady CFD analysis

Four velocity contours collected during the unsteady analysis are then represented in Figure 4.28. Considering that the dynamic phenomena is periodic, an reference time t_0 can be set. It can be seen that the period of the entire wake oscillation is of about 0.07 s, due to the almost identity between Figure 4.28(a) and Figure 4.28(d).

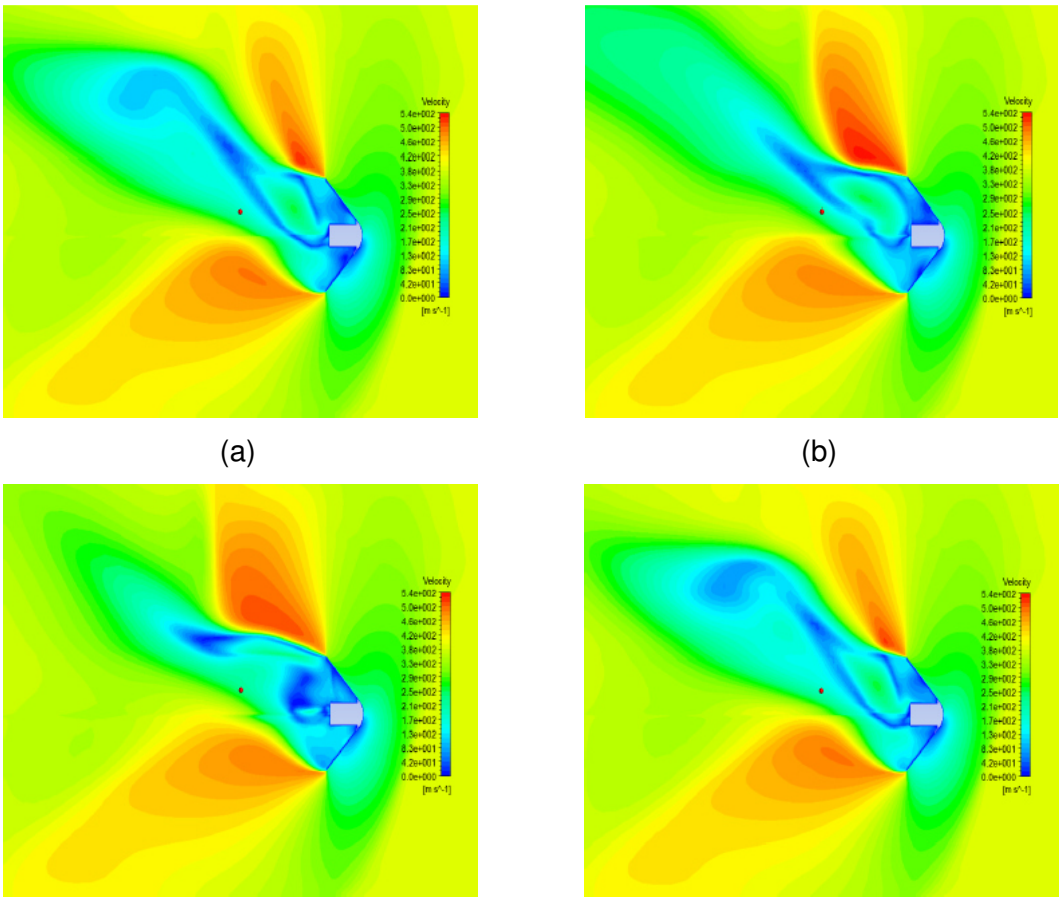

Figure 4.28: Velocity contour during the unsteady analysis at $t=t_0$ (a), $t=t_0+0.02$ s (b), $t=t_0+0.04$ s (c) and $t=t_0+0.07$ s (b)

The oscillation of the pressure and of the aerodynamic coefficients has been also monitored over time. They all oscillate with the same frequency (≈ 14 Hz), but with different amplitudes, reported in Table 4.13. In this case the pressure amplitude reported refers to the maximum value registered along the flexible part of the aerobrake.

	p [Pa]	C_L [-]	C_D [-]	C_M [-]
Amplitude	≈ 80	≈ 0.020	≈ 0.015	≈ 0.040

Table 4.13: Pressure and aerodynamic coefficients oscillation amplitudes

In conclusion, the present unsteady analysis can serve as a preliminary evaluation of dynamic phenomena registered during the re-entry phase of the capsule. In particular, it gives some information on the frequency of dynamic pressure loads that could affect the flexible part of the aerobrake from the aeroelastic point of view. They can also

serve as a reliable basis for future dynamic stability studies, where dynamic mesh should be also considered.

5 Conclusions and future developments

Aerothermodynamic and missions analyses of new concepts of deployable aerobraking systems have been performed along different mission profiles.

The concept allows flexible launch and re-entry operations, due to the opportunity to deploy the aerobrake and also to modulate its reference surface during the flight. Exploiting this peculiarity, the possibility to aerodynamically control the capsule de-orbit phase has been investigated and a preliminary control technique able to cope with the off-nominal entry conditions has been implemented.

A number of possible re-entry scenarios has been presented in order to show the wide range of potential applications in the near future, including the possibility to deorbit micro and nano-satellites to contrast the phenomenon of Space debris.

In addition, two different technology demonstrators to be launched onboard suborbital rockets have been presented. Suborbital demonstrative re-entry flights could be very useful to verify the effectiveness and the functionality of the innovative concept at growing energy levels, in particular before a more risky and expensive orbital re-entry flight test.

All the presented results can be considered as starting points for future specific mission and system analyses and for the design of wind tunnel and flight drop tests.

References

1. *Inflatable re-entry and descen ttechnology (IRDT) - further developments.* **Wilde, D. and Walther, S.** Arcachon, France : s.n., 2001. 2nd International Symposium of Atmospheric Re-entry Vehicles and Systems.

2. *Structural analysis and testing of the Inflatable Re-entry Vehicle Experiment (IRVE).* **Lindell, M. C., et al.** Newport,RI : s.n., 2006. ASME/ASCE/AHS/ASC Structures, Structural Dynamics, and Materials Conference.

3. *Nanosat de-orbit and recovery system to enable new missions.* **Andrews, J., Watry, K. and Brown, K.** Logan, UT : s.n., 2011. 25th Annual AIAA/USU Conference on Small Satellites.

4. **Andrews, D., et al.** *Deployable decelerator based microsatellite recovery. US 8292232 B1* United States, 2012.

5. *The parashield entry vehicle concept: basic theory and flight test developments.* **Alkin, D. L.** Logan, UT : s.n., 1990. 4th Annual AIAA/Utah State University Conference on Small Satellites.

6. *A Small Re-entry Capsule - BREMSAT 2.* **Wiegand, M. and Königsmann, H. J.** Logan, UT : s.n., 1996. 10th AIAA/USU Small Satellite Conference.

7. **Cotronics.** *Mechanicable and castable low expansion fused silica foam.*

8. **3M.** *Ceramic Textiles Tecnical Notebook.*

9. **Guariglia, D.** Analisi termografica di prove in galleria ipersonica "SCIROCCO" su una capsula di rientro dispiegabile. *Master Thesis.* Naples : University of Naples "Federico II", Academic Year 2011-2012.

10. **Aerospace Laboratory for Innovative components S.C.ar.l.** *Mission Scenarios and Baseline Definition.* 2010.

11. *Re-entry and launch proposals for an advances ISS crew transportation system.* **Carandente, V., et al.** Naples, Italy : s.n., 2012. 63th International Astronautical Congress.

12. *Responsive Air Launch.* **Frick, W., Guerci, J. and Horais, B.** Los Angeles, CA : s.n., 2004. 2nd Responsive Space Conference.

13. *MISTRAL (Air-Launchable Micro-Satellite with Reentry Capability) A small spacecraft to carry out several missions in LEO.* **Fortezza, R., Savino, R. and Russo, G.** Beijing, China : s.n., 2013. 64th International Astronautical Congress.

14. *Coverage, Responsiveness, and Accessibility for Various "Responsive Orbits".* **Wertz, J. R.** Los Angeles, CA : s.n., 2005. 3rd Responsive Space Conference.

15. **California Polytechnic State University.** *CubeSat design specifications.* 2010. Rev. 12.

16. **PocketQube Shop.** [Online] http://www.pocketqubeshop.com/.

17. *Conceptual design of de-orbit and re-entry modules for standard CubeSats.* **Carandente, V., Elia, G. and Savino, R.** Rome, Italy : s.n., 2013. 2nd IAA Conference on University Satellite Missions and CubeSat Workshop.

18. **Kallender-Umezu, P.** *A market for cleaning up Space junk?* 2011. Global Security Research Working Paper, n. 30.

19. **Kofford, A. S.** *System and method for creating an artifical atmosphere for the removal of Space debris. US 2013/0082143 A1* 2013.

20. **Gregory, D. A. and Mergen, J. F.** *Space debris removal using upper amosphere. 2012/094128 A1* 2012.

21. **Dunn, M. J.** *Space debris removal. WO 2012/128851 A1* 2012.

22. *Recovery of In-Space CubeSat Experiments (RICE) Project.* **Chan, B., et al.** Barcelona, Spain : s.n., 2010. 7th International Planetary Probe.

23. *IRENE—Italian Re-Entry NacellE forMicrogravityExperiments.* **Bassano, E., et al.** Cape Town, South Africa : s.n., 2011. 62nd International Astronautical Congress.

24. *Aerothermodynamic and Feasibility Study of a Deployable Aerobraking Re-Entry Capsule.* **Savino, R. and Carandente, V.** 4, s.l. : Tech Science Press, 2012, Fluid Dynamics and Materials Processing, Vol. 8, pp. 453-476.

25. *Study and development of a sub-orbital reentry demonstrator.* **Savino, R., et al.** Naples, Italy : s.n., 2013. 22nd Conference of the Italian Association of Aeronautics and Astronautics.

26. *Aerothermodynamic and stability analyses of a deployable re-entry capsule.* **Carandente, V., Zuppardi, G. and Savino, R.** s.l. : Elsevier, 2014, Acta Astronautica, Vol. 93, pp. 291–303.

27. **European Space Agency.** *European Users Guide to low Gravity Platforms.* UIC-ESA-UM-0001.

28. *Shark-Maxus 8 Experiment: A technology demonstrator of the re entry.* **Gardi, R., et al.** Hyre, France : s.n., 2011. 20th ESA Symposium on Europan Rocket and Baloon Programmes and Related Research.

29. **EuroLaunch.** *Rexus User Manual v7.11.* 2014.

30. **Anderson, J. D.** *Hypersonic and high temperature gas dynamics.* s.l. : McGrow-Hill Book Company, 1989.

31. **Tauber, M. E.** *A review of High Speed Convective, Heat Transfer Computation Methods.* 1989. NASA Technical Paper. 2914.

32. *Predicted solar cycle twenty-two 10.7 cm flux and satellite orbit decay.* **Tobiska, W. K., Culp, R. D. and Barth, C. A.** 1987, The journal of Astronautical sciences, Vol. 35, pp. 419-433.

33. *Entry Dispersion Analysis for the Genesis Sample Return Capsule.* **Desai, P. N. and McNeil Cheatwood, F.** 3, 2001, Journal of Spacecraft and Rockets, Vol. 38, pp. 345-350.

34. *Entry, Descent, and Landing Operations Analysis for the Stardust Re-Entry Capsule.* **Desai, P. N., et al.** Keystone, CO : s.n., 2006. AIAA/AAS Astrodynamics Specialist Conference and Exibit.

35. *Six-Degree-of-Freedom Entry Dispersion Analysis for the METEOR Recovery Module.* **Desai, P. N., et al.** 3, 1997, Journal of Spacecraft and Rockets, Vol. 34, pp. 334-340.

36. **Bertin, J. J.** *Hypersonic Aerothermodynamics.* s.l. : American Institute of Aeronautics and Astronautics Education Series, 1994.

37. **FLUENT Inc.** *FLUENT 6.3 Tutorial Guide.* 2006.

38. *A Review of Reaction Rates in High Temperature Air.* **Park, C.** 1740, 1989, AIAA Paper, Vol. 89.

39. *Analysis of thermochemical modeling and surface catalyticity in space vehicle reentry.* **Viviani, A., Pezzella, G. and Golia, C.** Anchorage, AK : s.n., 2008. 26th International congress of the aeronautical sciences.

40. *Numerical analysis of supersonic combustion ramjet with upstream fuel injection.* **Savino, R. and Pezzella, G.** 2003, International Journal for Numerical Methods in Fluids, Vol. 43, pp. 165–181.

41. **Porter, J. W. and White, N. C.** *Multi-layer stitched blanket insulation. US 5080306* 1992.

42. *Overview of Initial Development of Flexible Ablators for Hypersonic Inflatable Aerodynamic Decelerators.* **Beck, R. A., et al.** Dublin, Ireland : s.n., 2011. 21st AIAA Aerodynamic Decelerator Systems Technology Conference and Seminars.

43. *Aerodynamic and aerothermodynamic database of the Expert capsule.* **Schettino, A, et al.** Moscow, Russia : s.n., 2007. West-east high speed flow field cnference .

44. **Bird, G. A.** *Molecular Gas Dynamics and Direct Simulation Monte Carlo.* Oxford : Clarendon Press, 1998.

45. **Shen, C.** *Rarefied Gas Dynamics: Fundamentals, Simulations and Micro Flows.* Berlin : Springer, 2005.

46. **Moss, J. N.** *Rarefied Flows of Planetary Entry Capsules.* Rhode-Saint-Genèse, Belgium : s.n., 1995. pp. 95-129. AGARD-R-808.

47. *Oscillation of supersonic inflatable aerodynamic decelerators at Mars.* **Smith, B. P., Clark, I. G. and Braun, R. D.** Dublin, Ireland : s.n., 2011. 21st AIAA Aerodynamic Decelerator System Technology Conference and Seminar.

48. *Dynamic Stability Analysis of Blunt Body Entry Vehicles Through the Use of a Time-Logged Afterbody Pitching Moment.* **Kazemba, C., et al.** Grapevine, TX : s.n., 2013. 51st AIAA Aerospace Sciences Meeting.

49. *Flight Performance of the Inflatable Reentry Vehicle Experiment II.* **Dillman, R.** Barcelona, Spain : s.n., 2010. 7th International Planetary Probe Workshop.

50. **De Benedictis, D.** Studio meccanico ed aerotermodinamico di una capsula a geometria variabile. *Master Thesis.* Naples : University of Naples "Federico II", Academic Year 2011-2012.